ISSN 1590-8844
Vol. 08 No 01
2007

International Journal of Mechanics and Control

Honorary Editor: Guido Belforte

Editor: Andrea Manuello Bertetto

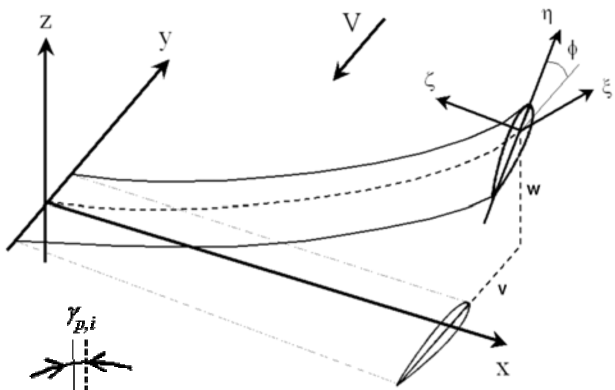

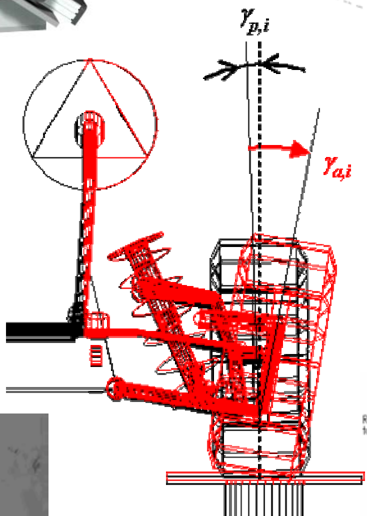

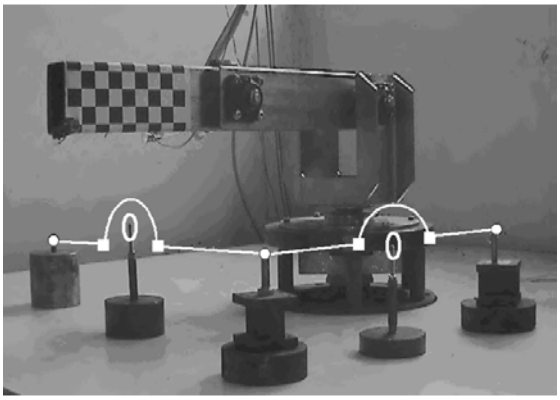

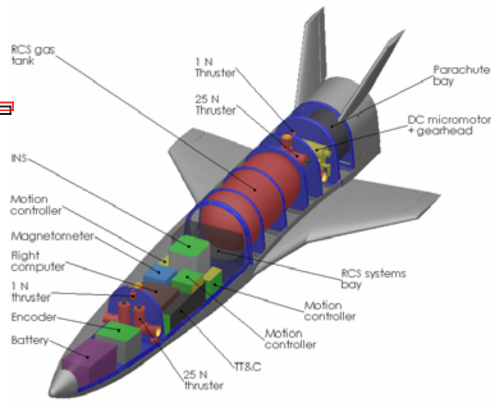

LIBRERIA EDITRICE UNIVERSITARIA
LEVROTTO & BELLA
TORINO

Official Torino Italy Court Registration
n.5390, 5th May 2000

Deposito presso il Tribunale di Torino
numero 5390 del 5 maggio 2000
Direttore responsabile:
Andrea Manuello Bertetto

International Journal of Mechanics and Control

The Journal is addressed to scientists and engineers who work in the fields of mechanics (mechanics, machines, systems, control, structures). It is edited in Turin (Northern Italy) by Levrotto&Bella Co., with an international board of editors. It will have not advertising.

Turin has a great and long tradition in mechanics and automation of mechanical systems. The journal would will to satisfy the needs of young research workers of having their work published on a qualified paper in a short time, and of the public need to read the results of researches as fast as possible.

Interested parties will be University Departments, Private or Public Research Centres, Innovative Industries.

Aims and scope

The *International Journal of Mechanics and Control* publishes as rapidly as possible manuscripts of high standards. It aims at providing a fast means of exchange of ideas among workers in Mechanics, at offering an effective method of bringing new results quickly to the public and at establishing an informal vehicle for the discussion of ideas that may still in the formative stages.

Language: English

International Journal of Mechanics and Control will publish both scientific and applied contributions. The scope of the journal includes theoretical and computational methods, their applications and experimental procedures used to validate the theoretical foundations. The research reported in the journal will address the issues of new formulations, solution, algorithms, computational efficiency, analytical and computational kinematics synthesis, system dynamics, structures, flexibility effects, control, optimisation, real-time simulation, reliability and durability. Fields such as vehicle dynamics, aerospace technology, robotics and mechatronics, machine dynamics, crashworthiness, biomechanics, computer graphics, or system identification are also covered by the journal.

Please address contributions to

Prof. Guido Belforte
Prof. Andrea Manuello Bertetto
PhD Eng. Elvio Bonisoli

Dept. of Mechanics
Technical University - Politecnico di Torino
C.so Duca degli Abruzzi, 24.
10129 - Torino - Italy - E.C.

e_mail: jomac@polito.it

Subscription information

Subscription order must be sent to the publisher:

Libreria Editrice Universitaria
Levrotto&Bella
2/E via Pigafetta – 10129 Torino – Italy

www.levrotto-bella.net
e_mail: info@levrotto-bella.net
tel. +39.011.5097367
+39.011.5083690
fax +39.011.504025

ISSN 1590-8844
International Journal of Mechanics and Control, Vol. 08, No. 01, 2007

DESIGN OF ADVANCED ROBOTIC SYSTEMS FOR ASSEMBLY AUTOMATION

Massimo Callegari, Andrea Gabrielli, Matteo Claudio Palpacelli, Marco Principi

Dipartimento di Meccanica, Università Politecnica delle Marche, Ancona, Italy

ABSTRACT

The paper describes the architecture of the virtual prototyping environments that can be presently set up to try to make the best from the concurrent mechatronic design of mechanical devices and control systems: though a single comprehensive tool is not available on the market at the moment, a proper integration of different software modules can do the job. As an example, a hybrid kinematic architecture for mechanical assembly is presented, based on the functional splitting of complex tasks between two cooperating parallel kinematics machines with limited mobility and equipped by proper interaction control.

Keywords: Design Automation, Virtual Prototyping, Mechatronics, Automated Assembly, Robotics

1 CAD ENVIRONMENTS FOR MECHATRONIC DESIGN

The automation of assembly tasks has been studied extensively for a long time, but the accomplishment of effective processes still deserves further research efforts [1]: the opportunities offered by current state-of-the-art technology cannot sometimes be exploited due to the complexity of the resulting plants, that makes difficult their design or even their management; this is the case, for instance, of assembly cells based on parallel kinematics machines.

Up-to-date design criteria deserve a tight integration between mechanics and control [2], according to the mechatronics paradigms shown in Fig. 1. The benefits of this approach are quite clear indeed: both shorter development times and a potential enhancement of system's performances can be easily achieved, since the design is not aimed at a "local" optimization of single modules (mechanics, electronics, informatics, etc.) but rather looks for suitable solutions for the entire system.

Contact author: Massimo Callegari

Università Politecnica delle Marche
Dipartimento di Meccanica
Via Brecce Bianche, s/n - 60131 Ancona - Italy
ph: +39 071 2204444 fax: +39 071 2204801
m.callegari@univpm.it, www.dipmec.univpm.it/meccanica

The use of this approach is much simplified by the availability of development environments able to support the designer during all the design steps [3], possibly up to the prototyping phase to be carried on with the aid of "hardware-in-the-loop" simulation tools.

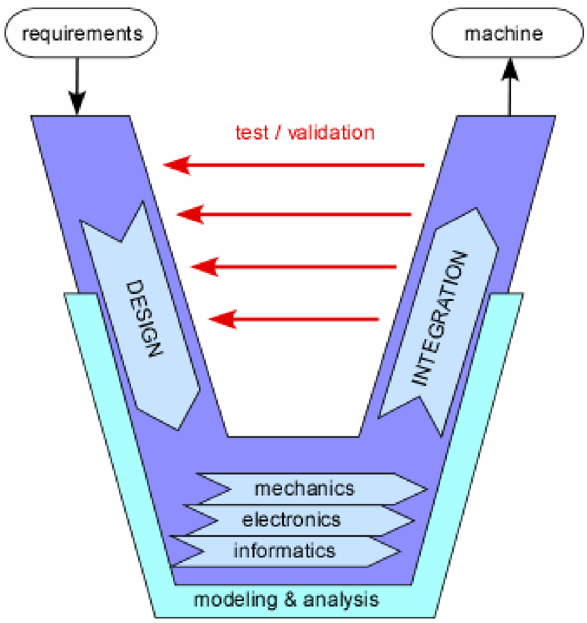

Figure 1 V-model for the development of mechatronic systems [4]

As a matter of fact, the need to reconsider previous design steps, that is pretty common in usual engineering practice by the way, is not dramatic in case an integrated development environment is available. Sometimes the same platform can also be used during the start-up and/or management of the plant itself, provided that the software tools support production planning activities, possibly up to off-line machines programming. Unfortunately a comprehensive design environment able to fulfil all the functions that have been outlined is not presently available in the market, in spite of providers' efforts to extend more and more the capabilities of their software packages. Therefore, it is now needed the use of different tools for the various aspects of the design and it is necessary to make resort to their capability to interface one to the other at various levels of integration, from the mere sharing of models that have been coded in proper file formats, to the synchronization of different processes, up to the full associativity of packages that can even share the same user interface.

2 ASSEMBLY MODELING

Figure 2 shows the virtual prototyping environment that is used at the Department of Mechanics of the Polytechnic University of Marche for the design of automated assembly systems based on parallel kinematic manipulators. The mechanical design is developed through conventional CAD tools, that allow to easily define even the most complex geometries and also to perform, e.g. by means of FEM modules, the needed structural analyses; the interface with a multibody code allows to perform a closed-loop dynamic analysis, with different levels of difficulty according to the associativity of the used programs.

To this aim, the *MSC VisualNastran* code is often used but in most complex cases the *LMS Virtual.Lab Motion* package has been used too, which is able to handle in a more convenient way complex situations like, for instance, the occurrence of an impact. In any case, the scheme of the simulation is always the same: the multibody code receives in input from the controller the actuation torques and integrates the equation of direct dynamics, providing in output the state variables that are assumed to be measured. The control system, that is implemented in the *Matlab/Simulink* environment, computes the control actions by taking into account the assembly task to be executed and sometimes also by exploiting the complete or partial knowledge of robot's dynamics (inverse dynamics model). If the task is constrained by the contact with the environment, like is usually the case for assembly, the contact forces can be measured too, to set up more efficient force control schemes [5].

As for task planning and robot programming, it is possible to use both commercial programs or specific packages, purposely developed for the application presently treated: a sample code developed for the planning of assembly tasks

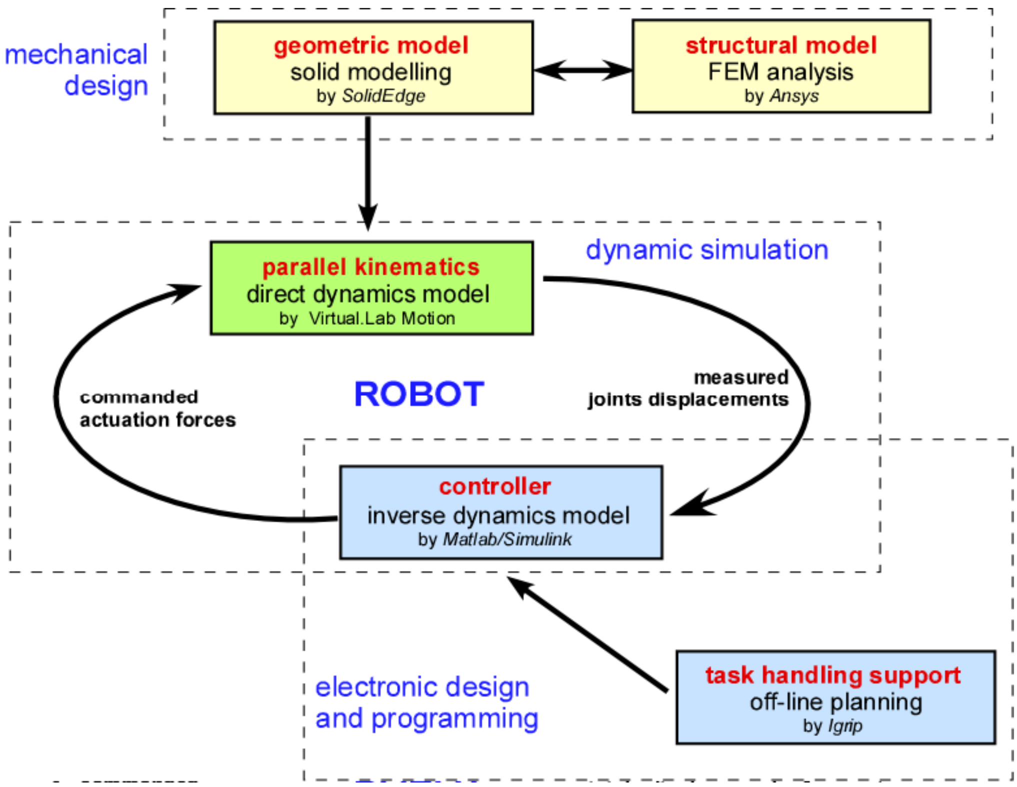

Figure 2 Integrated virtual prototyping environment for mechatronic design

is shown in the next section; as for commercial packages, the Authors have experience of the *Delmia IGRIP* software that, once the task has been defined off-line, is able to generate the part program for the controllers of the most common robot manufacturers.

In the end, once the most appropriate control logics have been set up off-line, an advanced development environment should allow the direct generation of the code for the controller and its download to the actual control hardware.

3 ANALYSIS AND PLANNING OF ASSEMBLY TASKS

The usefulness of a computer aided support tool for the planning of assembly tasks can be effectively shown with reference to the well known case of peg-in-hole assembly: even in the simplest case of rigid bodies, cylindrical surfaces and smoothed chamfers, many variables affect the process, as for instance diametral play, misalignment angle, friction coefficient, contact forces and moments, etc.

In any case, an effective accomplishment of the task must be based on the availability of suitable compliant wrists or, in case a high accuracy is needed, on manipulator's capability of controlling both mutual positions and static and/or dynamic actions between the parts in contact. It is therefore easily understood that an impedance or even a hybrid position/force control is better designed only after a careful study of the parameters involved in the task.

By making reference to the classic studies developed by D.E. Whitney and J.L. Nevins at MIT in the first '80s [6-7], the so-called "fine motion" assembly has been divided into the following five phases, shown in Fig. 3: *approach, chamfer crossing, one-point contact, two-points contact, linear contact* and a specific Matlab code has been developed for the simulation and planning of the resulting scenarios.

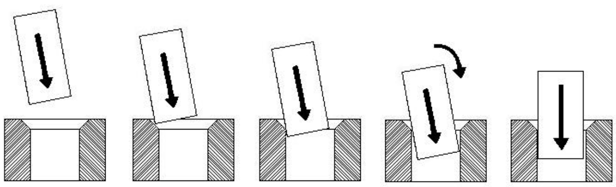

Figure 3 The five different phases of fine-motion assembly

Two typical problems can arise during the assembly task, both preventing the fulfilment of the operation because the peg appears stuck in the hole: the *jamming* consists in a wrong proportion among the exerted forces and moments and can occur both during one-point and two-point contact phases; the *wedging*, on the other hand, can arise only during the two-point contact phase and, deriving from a wrong geometric setting, cannot be avoided by varying the applied forces or moments.

The mathematical model of both situations has been derived and useful diagrams have been drawn [8]; many geometrical and static parameters play a significant role in the assembly, e.g. peg's diameter d, hole's diameter D, static friction coefficient μ and parts' misalignment θ: in the diagrams that are shown in the following figures, some of these parameters are assigned while others are varied in order to study the sensitivity of the assembly to such variations.

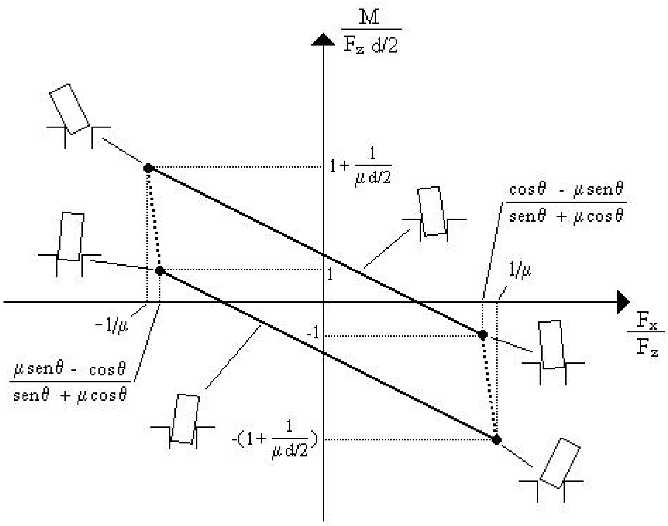

Figure 4 Jamming diagram (absence of chamfer)

For instance, the *jamming diagram* shown in Fig. 4 plots with solid lines the combinations of external actions (lateral force F_x, axial thrust F_z and bending moment M_z) that correspond to situations of equilibrium: the inside area represents a slipping region where the dynamic unbalance among the external and the reaction forces leads to successful mating of the parts, while the region outside such equilibrium lines eventually jam the peg, either in one- or two-point contact.

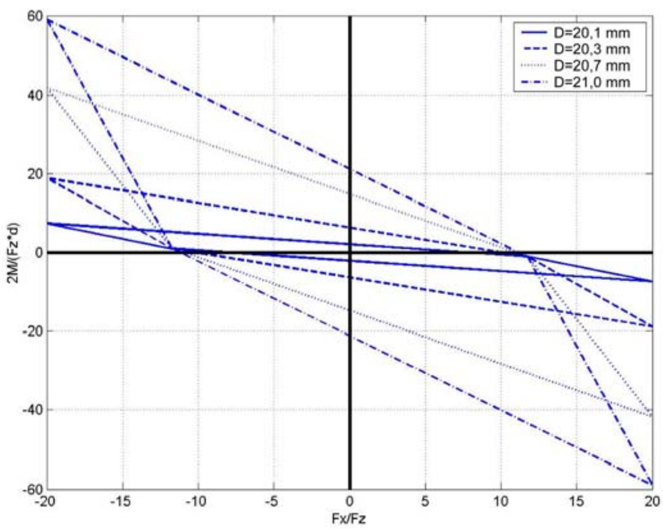

Figure 5 Jamming diagram for different values of hole's diameter D (μ=0.05, d=20.0 mm, θ=2°)

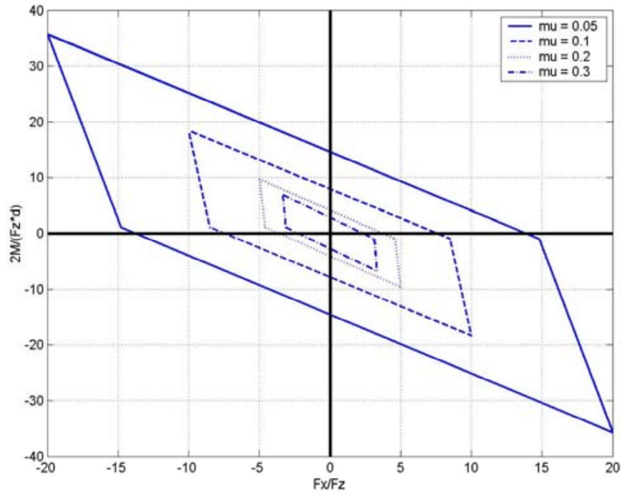

Figure 6 Jamming diagram for different values of friction coefficient μ (D=20.3 mm, d=20.0 mm, θ=1°)

Figures 5 and 6 both refer to the same sample case but the occurrence of jamming is studied against variations of the diametral play in Fig. 5 while the influence of friction coefficient is investigated in Fig. 6.

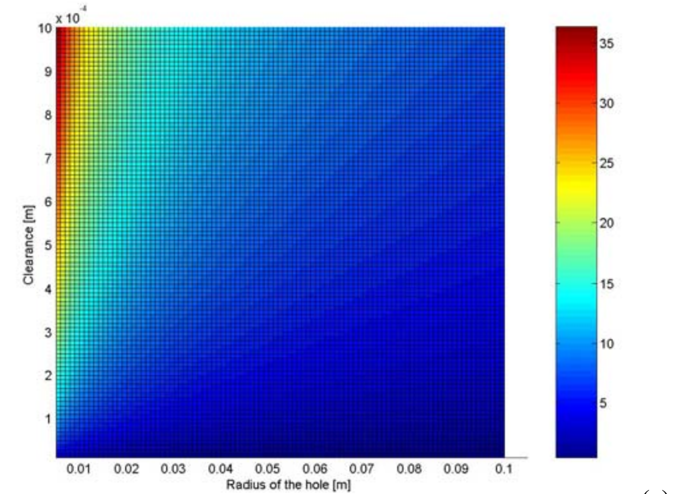

(a)

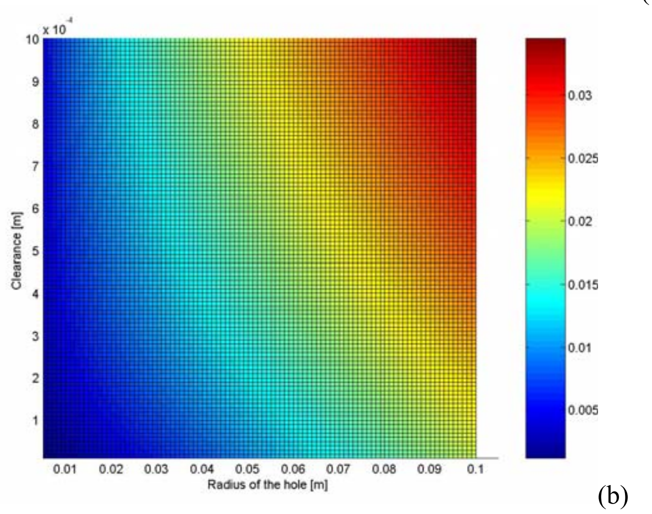

(b)

Figure 7 Limit values for tilt angle (a) and insertion depth (b) to avoid wedging

In Fig. 7, instead, the limit values of the tilt angle θ (Fig. 7a) and of the insertion depth h (Fig. 7b) able to avoid wedging are assessed against variations of hole's radius and clearance.

4 SAMPLE CASE

Parallel kinematics machines are often characterised by potentially high performances but their actual behaviour is limited by difficulties in design and control, especially in the case of 6 axes robots, mainly due to their complex kinematics. A possible solution lies in the use of (several) simpler machines, characterised by limited mobility: hybrid machines may be designed (e.g. a conventional "serial" wrist on top of a "parallel" shoulder, see the Tricept concept) or mini-maxi architectures can be experimented; alternatively, a full-mobility task may be decomposed into elemental sub-tasks, to be performed by separate minor mobility machines, like done already in conventional machining operations and recently proposed also for PKM's [9]. In this case a proper mechatronic design allows to exploit, at least partially, the advantages of both architectures, while the disadvantages can be minimised. In this way it is possible to realise hybrid cooperative systems with many degrees of freedom, leading to a modular and reconfigurable system architecture.

The example here described is taken from the results of a research developed at the Department of Mechanics of the Polytechnic University of Marche, aimed at assessing the feasibility of complex assembly tasks (e.g. 6 axes operations) by means of the use of two cooperating parallel robots, both characterized by a simple mechanical and control architecture. The two machines are based on the same 3-CPU architecture, meaning that the mobile platform is connected to the ground frame by means of 3 identical limbs, each one composed by the following joint sequence: Cylindrical, Prismatic, Universal.

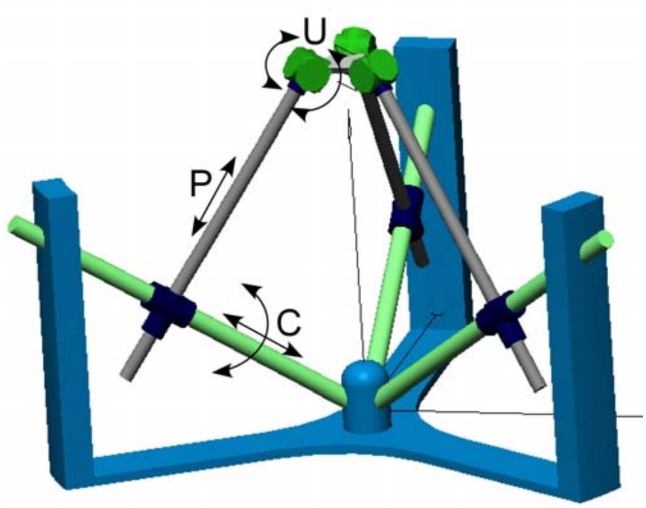

Figure 8 Concept of a pure translations robot derived from the 3-CPU mechanism

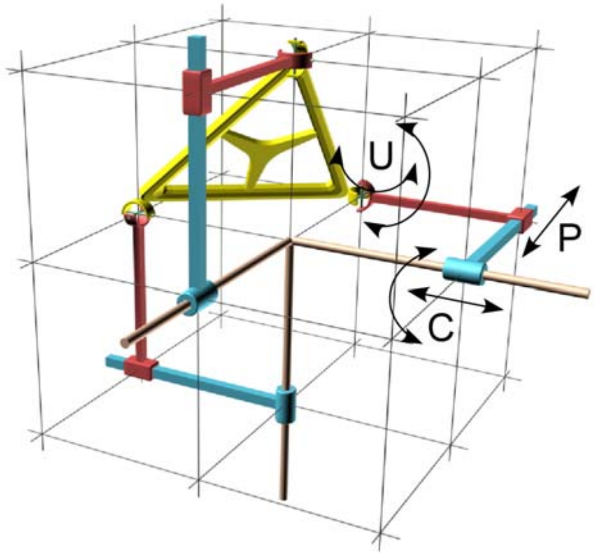

Figure 9 Concept of a spherical wrist derived from the 3-CPU mechanism

In one case, shown in Fig. 8, joints axes are set in space so that the mobile platform can freely translate (without rotating) inside its 3D workspace: this is easily obtained by arranging the universal joint so that the axis of the outer revolute joint is parallel to the cylindrical joint in each limb; such three directions are mutually orthogonal to maximise the workspace and grant optimal manipulability.

With a different setting of the joints, shown in Fig. 9, three degrees of freedom of pure rotation are obtained at the terminal of the spherical wrist: in this case the axes of the cylindrical joints and those of the outer revolute pairs in the universal joints all intersect at a common point, which is the centre of the spherical motion.

Figure 10 shows the functional architecture of the whole system: it has been first studied and designed by means of the simulation environment previously explained and now the physical prototypes are under construction. The control systems of the two machines are equipped with an impedance controller, so that the relative stiffness of the system can be varied during parts' mating to allow an effective accomplishment of the task but, on the other hand, the complexity of the hybrid position/force algorithms (needing proper force sensors and the availability of real time robots' inverse dynamics models) is avoided.

The simulations have shown the benefits of the prospected mechatronic architecture and allowed to tune the design of the mechanical and control systems. The prototype of the translational robot has been built already, see Fig. 11, and it is actuated by brushless motors and linear modules based on ball-screw drives; the controller is based on the *DSpace DS1103* card and the code has been written in *Matlab*, tested in the mentioned virtual prototyping environment and then downloaded to the controller by means of the *Matlab Realtime Workshop* toolbox.

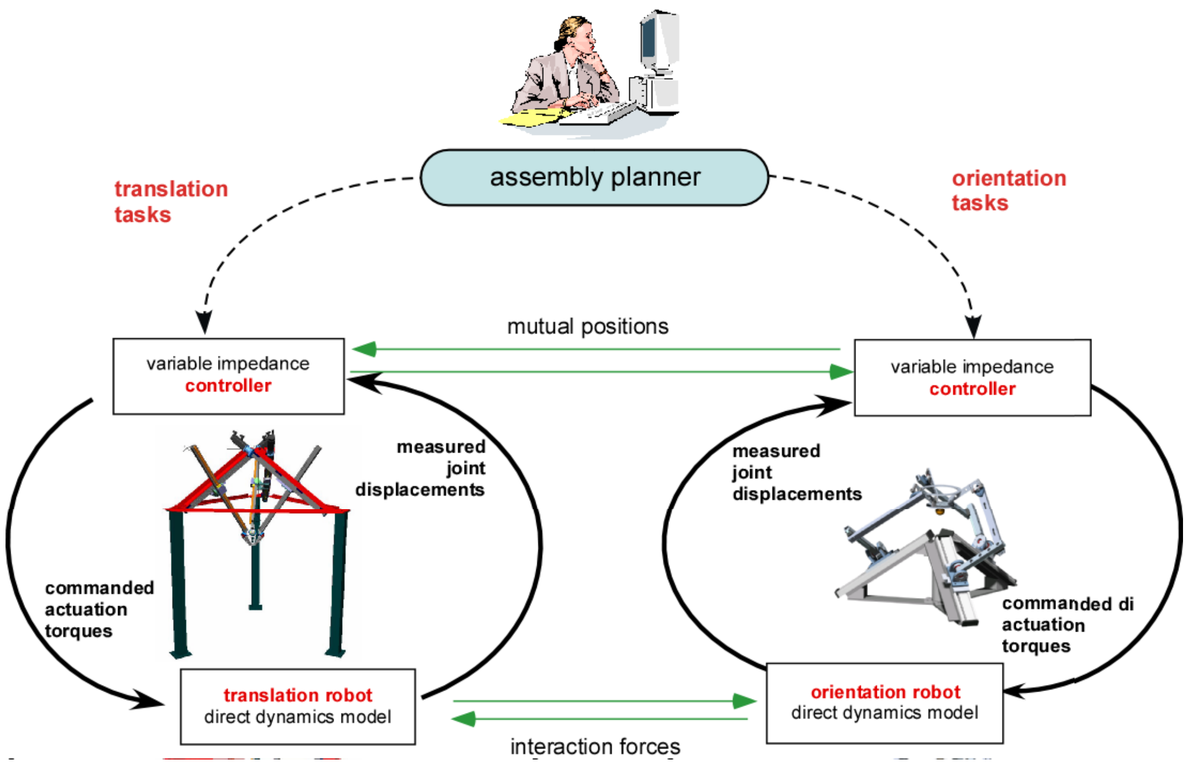

Figure 10 Architecture of the assembly system based on cooperating parallel robots

The spherical wrist, instead, is presently under construction and Fig. 12 shows the final design: it will be directly driven by 3 linear motors by *Phase* and controlled by a *Nation Instrument* system based on the *PXI/FlexMotion* hardware.

Figure 11 Prototype of translation robot

Figure 12 Final design of spherical wrist

5 CONCLUSIONS

The paper has presented the layout of a virtual prototyping environment developed at the Polytechnic University of Marche for the mechatronic design of advanced robotic systems. As an example, the architecture of a cell for mechanical assembly is presented: it is based on the functional splitting of complex tasks between two cooperating parallel kinematics machines with limited mobility and equipped by proper interaction control. The design phase has been completed already and the first experimentations are presently under execution.

REFERENCES

[1] Michelini R.C., Acaccia G.M., Callegari M. Molfino, R.M. and Razzoli, R.P., Computer Integrated Assembly for Cost Effective Developments, in: *Computer Aided Design, Engineering and Manufacturing: Systems Techniques and Applications, Vol. II: Computer Integrated Manufacturing*, Cornelius T. Leondes Ed., CRC Press LLC, Boca Raton (FL), pp. 2.1-2.68, 2001.

[2] Callegari M., La meccatronica per progettare con le PKM, *Soluzioni di Assemblaggio* (supplement to *Rivista di Meccanica*), VNU, Anno II, N° 3, pp. 96-98, 2006.

[3] Michelini R.C., Acaccia G.M., Callegari M., Molfino R.M. and Razzoli R.P., Instrumental Robots Design with Applications to Manufacturing, in: *Computer Aided Design, Engineering and Manufacturing: Systems Techniques and Applications, Vol. VII: Artificial Intelligence and Robotics in Manufacturing*, Cornelius T. Leondes Ed., CRC Press LLC, Boca Raton (FL), pp. 7.1-7.62, 2001.

[4] Verein Deutscher Ingenieure, VDI 2206: *Design methodology for mechatronical systems*, Beuth Verlag, Berlin, 2004.

[5] Siciliano B and Villani L., *Robot Force Control,* Kluwer, Dordrecht, 2000.

[6] Whitney D.E. Quasi-Static Assembly of the Compliantly Supported Rigid Parts, *ASME J. Dynamic Systems, Measurement and Control*, Vol. 104, No. 1, pp. 65-77, 1982.

[7] Nevins J.L. and Whitney D.E., *Concurrent Design of Products and Processes*, McGraw-Hill, New York, 1989.

[8] Callegari M. and Suardi A., On the force-controlled assembly operations of a new parallel kinematics manipulator, *Proc. Mediterranean Conf. on Control and Automation*, Rhodes, June 18-20, IV06-02, 2003.

[9] Tsai L.-W. and Joshi S., Kinematics Analysis of 3-DOF Position Mechanisms for Use in Hybrid Kinematic Machines, *ASME J. Mech. Design*, Vol. 124, pp. 245-253, 2002.

ISSN 1590-8844
International Journal of Mechanics and Control, Vol. 08, No. 01, 2007

ECCENTRICITY EFFECT ON THE CRITICAL AEROELASTIC CONDITION OF SLENDER WINGS

Giacomo Frulla, Enrico Cestino

Politecnico di Torino, Dept. of Aerospace Engineering, Turin, 10129, Italy

ABSTRACT

In the design of High-Altitude Long-Endurance (HALE) UAVs wings, the goal is usually to minimize the weight of the aircraft structure for a given payload weight. In the optimal design process, the structural weight is reduced until design constraints become active. Reduction of the structural weight of the structure tends to produce wings that are more flexible, forcing the designer to deal with specific phenomena not usually considered in classical aircraft definition proposing different design indications.
Among various aeroelastic problems correlated with high aspect ratio wings, the flutter condition and the influence of selected design aeroelastic parameters, such as tip deflection and center of gravity offset from elastic axis will be discussed in the paper. The flutter condition will be analysed in the paper considering that HALE wings can experience moderate to large static deflections during normal flight operations with the consequence of not conventional couplings that reduce flutter speed. A geometrically consistent non-linear structural model is adopted based on Hodges and Dowell, including Da Silva second order geometrical non-linear terms. The structural model has been coupled with an unsteady aerodynamic model for an incompressible flow field, based on the Wagner aerodynamic indicial function, in order to obtain a non-linear aeroelastic model.

Keywords: HALE Flutter Behaviour, Non-Linear Aeroelasticity

NOMENCLATURE

a = Elastic axis location
b = Semi-chord
e = Section mass center from elastic axis
E = Modulus of elasticity
G = Shear modulus
U = Free-stream velocity
m = Mass per unit length
I_η, I_ζ = Vertical and chord-wise area moments of inertia, respectively
ρ = Air density
G = Torsional stiffness constant
ω_r = Reference frequency
L = Wing semi-span
$\varepsilon_1, \varepsilon_2$ = Wagner function constants
v, w, ϕ = lag, flap and torsional displacements, respectively
$w_{3/4c}$ = Downwash velocity at ¾ chord
EI_ζ, EI_η, GJ = Bending and torsion rigidity
G'_v, G'_w, G'_ϕ = Added non-linear 2nd order terms
L_v, L_w, M_ϕ = Generic in-plane, out-of-plane and aerodynamic moment resultant expressions.
κ = parameter vector
q = generalized coordinate vector
Ψ = generic autonomous governing system

Contact author: Enrico Cestino

Department of Aerospace Engineering

Corso Duca degli Abruzzi 24, 10129 Torino - Italy

E-mail: enrico.cestino@polito.it

1 INTRODUCTION

The development of advanced uninhabited air vehicles (UAVs) will require improved understanding of the different aero-structural interactions than the conventional flight vehicles. New types of UAVs with wingspans greater than 60 meters and aspect ratios greater than 30 are envisioned [1,2,3,4], and existing analysis and design tools are not suited for analysis of such configurations as nonlinear aeroelastic effects may dominate such configurations. In the case of slender wing aircrafts, static structural deflections occurring during standard flight conditions could dangerously modify their behaviour and can introduce some unexpected changes in aeroelastic properties.

As we try to reduce weight increasing performance levels using directional material, thus leading to an increasingly flexible aircraft, there is a need for reliable analysis tools, which model all the important characteristics of the fluid-structure interaction problem. Aeroelastic instabilities always constrain the flight envelope and thus they have to be considered fundamental during the design process.

The flutter speed and flutter frequency are defined as the lowest airspeed and corresponding frequency at which a given structure flying in a specific atmosphere will exhibit sustained simple harmonic oscillations. Flutter condition is a borderline situation or neutral stability due to the fact that small motions must be stable at a speed below flutter speed , whereas divergent oscillations occur in a range of speed above flutter speed. Based on small motion hypothesis, a specific aerodynamic linear operator can be applied such as the Theodorsen scheme. The final problem led to a complex eigenvalue problem where two characteristic numbers have to be determined: speed and frequency. In the flutter condition, where the approximation is strictly valid, the real part of at least one of the characteristic exponents from negative value becomes zero and after positive: zero damping parameter identifies flutter speed. From these items as in [8], the classical flutter calculation was derived such as the well known V-g approach. This classical approach is strictly referred to the undeformed configuration as an initial point with small motion superimposed. If the aero-elasto-dynamic governing equations of a generic autonomous system can be represented by the following vector relation in R^n:

$$\dot{q} = \Psi(q, \kappa) \tag{1}$$

a stationary point of the system can be indicated by q^e such that $\Psi(q^e, \kappa) = 0$. Following the definition above, the small motion hypothesis admits a representation of the governing system in the following form assuming constant parameters:

$$\begin{aligned} \dot{z} &= \Psi(q^e + z, \kappa) = \\ &= \Psi(q^e, \kappa) + J(\Psi)_{q^e} z + \cdots \\ &\cong J(\Psi)_{q^e} z \end{aligned} \tag{2}$$

with z as the small perturbation and J as the Jacobian of Ψ evaluated in the equilibrium condition. If the Ψ application is linear : $\Psi = [H(\kappa)]q$, then:

$$J(\Psi)_{q^e} = [H]_{q^e} = [H]_{\overline{q}} = [H] \tag{3}$$

with $\overline{q}$ generic reference point such as the undeformed state $\overline{q} = 0$. The dynamic characteristics of the perturbed motions are the same whatever reference point is assumed. In this situation it is possible to investigate the flutter behaviour of the system and a flutter condition can be determined and identified as classical flutter speed or linear flutter speed. In the following it will be named LFS that is: “flutter velocity in linear equilibrium condition”. On the contrary as the Ψ operator is non-linear, due to high structural flexibility, the perturbed motion dynamic is influenced by the chosen equilibrium point. The reduced linear perturbation system originates a linear approximation of the behaviour of the system in the neighbourhood of the static equilibrium point with the possibility of calculating a flutter speed for each condition. In this case the flutter speed is identified in the following by NLFS that is: “ flutter velocity in non-linear equilibrium condition”. In the case of slender HALE structures the classical approach is no longer suitable to obtain correct flutter identification.

Flutter speed in High Aspect Ratio wings is influenced by many parameters and in particular static tip deflection and stiffness ratio between in-plane stiffness and out-of-plane stiffness has been demonstrated that could play an important role in determine the flutter boundaries [5,6,7,12]. The flutter condition is also affected by other structural parameters like section mass eccentricity from elastic axis. To achieve an efficient design of flexible airplanes, a better understanding of all the factors contributing to the occurrence and increase of the flutter boundary are required. An investigation of this parameter such as the effect of tip deflection have been carried out in this paper considering a typical low aspect ratio configuration (AR=7) and a typical high aspect ratio configuration (AR=20).

2 AEROELASTIC GOVERNING EQUATIONS

2.1 STRUCTURAL MODEL

In this paper a geometrically non-linear moderate to large deflection structural model, based on [9] and modified according to the second order geometrically non-linear terms proposed in [10], has been coupled with an unsteady aerodynamic model for an incompressible flow field based on the Wagner indicial function [8,11]. Although an unsteady aerodynamic model accounting for stall can be included similarly to [12,13,14] or via the use of non-linear indicial function [15], in this paper, to emphasize the effect of the nonlinear structural coupling, only a linear aerodynamic model has been considered. The strain displacement relations are developed from a consistent transformation between the deformed and undeformed coordinate systems. The wing is assumed to be clamped in the plane of symmetry and the equations of motion are obtained from Hamilton’s principle. These equations are also valid for beams with a mass centroid axis offset from the elastic axis, non-uniform mass and stiffness section properties, and variable pre-twist. Terms up to second order have been retained in the final expression. Higher non-linear terms have been neglected assuming they would have a negligible effect on the system dynamics. Rotary inertia has been neglected according to the slender beam hypothesis. The effect of shear deformation has also been neglected. The resulting equations, Eqs. (4a-c), are valid to second-order for long, slender, homogeneous, isotropic beams undergoing moderate to large displacements. Such assumptions are consistent with [9], and the reader is referred to [9,10] and the references cited therein for further details.

$$\begin{cases} EI_\zeta v'''' + \left[\left(EI_\zeta - EI_\eta\right)\phi w''\right]'' + G'_v + m\ddot{v} = L_v \\ EI_\eta w'''' + \left[\left(EI_\zeta - EI_\eta\right)\phi v''\right]'' + G'_w + m\ddot{w} + me\ddot{\phi} = L_w \\ -GJ\phi'' + \left(EI_\zeta - EI_\eta\right) v'' w'' + G'_\phi + mk_m^2\ddot{\phi} + me\ddot{w} = M_\phi \end{cases} \tag{4a-c}$$

In Eqs. (4a-c), G'_v, G'_w, G'_ϕ are the second order non-linear terms derived from Da Silva [10] and expressed as:

$$\begin{aligned} G'_v &= GJ\left(\phi' w''\right)' - I_\zeta \ddot{v}'' \\ G'_w &= -GJ\left(\phi' v''\right)' - I_\eta \ddot{w}'' \\ G'_\phi &= -GJ\left(v' w''\right)' \end{aligned} \tag{5a-c}$$

where the terms with double derivative in time are rotary inertia terms. According to the Euler-Bernoulli beam model, applicable to slender beam and low frequency vibrations, the effect of shear deformations and rotatory inertia could be neglected. This is the case being studied, so these effects will be neglected in the results presented below. In order to solve the system of governing equations and to study the subcritical and supercritical aeroelastic response as well as the flutter boundaries, the introduction of a small dynamic perturbation about a non-linear static equilibrium is applied. In-plane, out-of-plane and torsional displacements (v, w, ϕ) are considered to be a summation of the static and dynamic components in the undeformed reference system. Hence, the displacements can be written as:

$$\begin{aligned} v &= v_s + \bar{v} \\ w &= w_s + \bar{w} \\ \phi &= \phi_s + \bar{\phi} \end{aligned} \tag{6a-c}$$

where v_s, w_s, and ϕ_s are the static in-plane lagging, out-of-plane bending and torsion displacements due to the aeroelastic trim, corresponding to a specific flight condition, respectively. The deformed beam scheme used in the present model is shown in Figure 1.

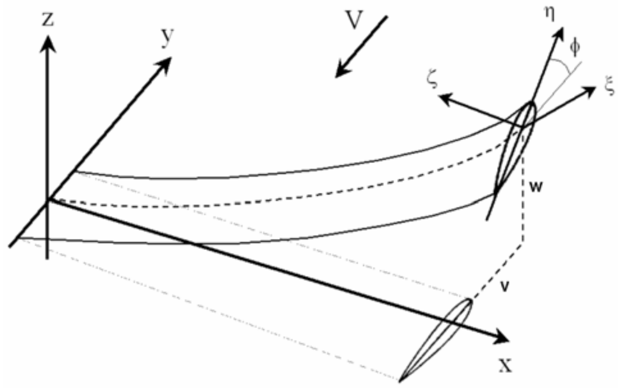

Figure 1 Reference system

A moderate/large deflections small perturbations approximation has been introduced and the static variables are considered only x dependent. The dynamic parts of the displacements are both time and space dependent. Using modal analysis techniques, the solution of the problem can be approximated as:

$$\begin{aligned} v(x,t) &= v_s + \sum_{i=1}^{N_v} \zeta_i(t) v_i(x) \\ w(x,t) &= w_s + \sum_{i=1}^{N_w} \eta_i(t) w_i(x) \\ \phi(x,t) &= \phi_s + \sum_{i=1}^{N_\phi} \beta_i(t) \phi_i(x) \end{aligned} \tag{7a-c}$$

The form of the solution is independent of the trial functions employed to discretize the system, but the proximity of the discrete system to the original one is dependent on the choice and the number of trial functions used. A well-chosen set of trial functions can accurately represent the original continuous system in terms of a few discrete coordinates. Previous investigations [16] on cantilever beams, using uncoupled mode shapes for flap-lag-torsion stability analysis, indicated that results would be satisfactorily accurate with as few as one or two trial functions. The example presented in this paper uses six trial functions (two for each degree of freedom) which are the mode shape functions of a vibrating uniform cantilever beam. The partial differential equations governing the dynamics of the flexible beam were reduced to a system of ordinary differential equations using a series discretization technique [17], along with Galerkin's method, to obtain the aeroelastic governing equations. Substituting Eqs. (3a-c) into Eqs. (1-a-c) it is possible to identify two sets of governing equations: a static aeroelastic equilibrium system and a perturbed dynamic system. The static equilibrium non-linear system can be expressed as:

$$
\begin{cases}
S_\varsigma v_s'''' + \left[\left(S_\varsigma - S_\eta\right)\phi_s w_s''\right]'' + S_\phi\left(\phi_s' w_s''\right)' = F_y \\
S_\eta w_s'''' + \left[\left(S_\varsigma - S_\eta\right)\phi_s v_s''\right]'' - S_\phi\left(\phi_s' v_s''\right)' + mg = F_w \\
-S_\phi \phi_s'' + \left(S_\varsigma - S_\eta\right) v_s'' w_s'' - S_\phi\left(v_s' w_s''\right)' + mge = F_\phi
\end{cases}
\quad \text{(8a-c)}
$$

Where S_i are bending and torsional stiffness. Given a free-stream velocity and an angle of attack α, static displacements for the correspondent trim condition can be computed by means of eq. (8). The static values enter then the dynamic perturbed system coupling with dynamic displacements. A dimensionless form of the system can be derived and perturbed equations of motion may be rewritten in terms of the mode shapes as reported in [6,7,19]. Introducing the dimensionless variables and their space and time derivatives in the form:

$$
\hat{\chi}_v = \sum_{i=1}^{N_v} \hat{\zeta}_i \hat{v}_i \;,\; \hat{\chi}_v' = \sum_{i=1}^{N_v} \hat{\zeta}_i \hat{v}_i' \;,\; \dot{\hat{\chi}}_v = \sum_{i=1}^{N_v} \dot{\hat{\zeta}}_i \hat{v}_i \quad (9)
$$

where prime denotes space derivatives and point time derivatives. Dimensionless perturbed non-linear system becomes:

$$
\Gamma\Omega_h \hat{\chi}_v'''' + \Omega_h\left(\Gamma-1\right)\left[\phi_s \hat{\chi}_w'' + \hat{w}_s'' \hat{\chi}_\phi\right]'' +
$$
$$
+ \ddot{\hat{\chi}}_v + \Omega_\alpha \Lambda^2 \left[\phi_s' \hat{\chi}_w'' + \hat{w}_s'' \hat{\chi}_\phi'\right]' = \hat{L}_v
$$

$$
\Omega_h \hat{\chi}_w'''' + \Omega_h\left(\Gamma-1\right)\left[\phi_s \hat{\chi}_v'' + \hat{v}_s'' \hat{\chi}_\phi\right]'' +
$$
$$
+ \ddot{\hat{\chi}}_w + x_\alpha \ddot{\hat{\chi}}_\phi - \Omega_\alpha \Lambda^2 \left[\phi_s' \hat{\chi}_v'' + \hat{v}_s'' \hat{\chi}_\phi'\right]' = \hat{L}_w
$$

$$
-\Omega_\alpha \hat{\chi}_\phi'' + \Omega_h\left(\Gamma-1\right)\left[\hat{v}_s'' \hat{\chi}_w'' + \hat{w}_s'' \hat{\chi}_v''\right] +
$$
$$
+ r_\alpha^2 \ddot{\hat{\chi}}_\phi + x_\alpha \ddot{\hat{\chi}}_w + \Omega_\alpha \Lambda^2 \left[\hat{v}_s'' \hat{\chi}_w'' + \hat{w}_s'' \hat{\chi}_v''\right] = \hat{M}_\phi
$$

(10a-c)

where $\hat{\phi}_s$ is the dimensionless static torsional displacement (function of dimensionless coordinate $\hat{x}$), while $\hat{v}_s$ and $\hat{w}_s$ that are respectively the static in-plane and out of plane displacements nondimensionalized by the semi-chord. The nondimensional parameters used in the above equations are defined as:

$$
\begin{aligned}
&\Omega_h \equiv \frac{EI_\eta}{m\omega_r^2 L^4},\; \Gamma = \frac{EI_\zeta}{EI_\eta},\; x_\alpha \equiv \frac{e}{b},\; \Omega_\alpha \equiv \frac{GJ}{m\omega_r^2 b^2 L^2}, \\
&r_\alpha^2 \equiv \frac{mk_m^2}{mb^2},\; k \equiv \frac{\omega_r b}{U},\; \mu \equiv \frac{m}{\pi\rho b^2},\; a,\; \Lambda = \frac{b}{L}
\end{aligned}
\quad (11)
$$

2.2 UNSTEADY AERODYNAMIC MODEL

The unsteady aerodynamic forces can be obtained using Wagner's indicial function in Duhamel integral form [8,11]. Considering that instantaneous aerodynamic components should act on the deformed reference system, while the generic in-plane, out-of-plane and aerodynamic moment resultant expressions indicated in Eqs. (10a-c) are referred to the undeformed reference system, a transformation matrix should be applied to the aerodynamic loads. As a consequence, the introduction of static/dynamic coupling terms also in the aerodynamic part of the model should be considered, see [4] for more details. Due to the presence of the integral terms in the aerodynamic integro-differential equations [8,20], it is cumbersome to integrate them numerically. However, applying properties of the integration by parts, and introducing the variables [12]:

$$
W_1 = \int_0^t w e^{-\varepsilon_1(t-\sigma)} d\sigma \;,\; W_2 = \int_0^t w e^{-\varepsilon_2(t-\sigma)} d\sigma
$$
$$
W_3 = \int_0^t \phi e^{-\varepsilon_1(t-\sigma)} d\sigma \;,\; W_4 = \int_0^t \phi e^{-\varepsilon_2(t-\sigma)} d\sigma
$$

(13a-d)

the airloads can be rewritten in general form containing just differential operators leading to a state-space form.

$$
\begin{aligned}
\hat{L} = {} & \hat{C}_1 \ddot{\hat{w}} + \hat{C}_2 \dot{\hat{w}} + \hat{C}_3 \hat{w} + \hat{C}_4 \ddot{\hat{\phi}} + \hat{C}_5 \dot{\hat{\phi}} + \hat{C}_6 \hat{\phi} + \\
& + \hat{C}_7 \hat{W}_1 + \hat{C}_8 \hat{W}_2 + \hat{C}_9 \hat{W}_3 + \hat{C}_{10} \hat{W}_4 + \hat{F}_0
\end{aligned}
\quad (14)
$$

$$
\begin{aligned}
\hat{M}_\phi = {} & \hat{D}_1 \ddot{\hat{w}} + \hat{D}_2 \dot{\hat{w}} + \hat{D}_3 \hat{w} + \hat{D}_4 \ddot{\hat{\phi}} + \hat{D}_5 \dot{\hat{\phi}} + \\
& + \hat{D}_6 \hat{\phi} + \hat{D}_7 \hat{W}_1 + \hat{D}_8 \hat{W}_2 + \hat{D}_9 \hat{W}_3 + \hat{D}_{10} \hat{W}_4 + \hat{P}_0
\end{aligned}
\quad (15)
$$

where the coefficients $\hat{C}_i$ and $\hat{D}_i$ are functions of the elastic axis location a, the reduced frequency k, the mass parameter μ and the unsteady indicial function coefficients. F_0 and P_0 are the aerodynamic loads due to initial conditions. Their expressions can be found in [9].

2.3 STATE SPACE FORMULATION

The dimensionless state vector $\left\{X\right\} = \left\{x_1, \ldots, x_{20}\right\}^T$ become function of the displacement variables and the additional aerodynamic lag states as:

$$\begin{aligned}&\hat{x}_1=\hat{\dot{\varsigma}}_1,\ \hat{x}_2=\hat{\dot{\varsigma}}_2,\ \hat{x}_3=\hat{\dot{\eta}}_1,\ \hat{x}_4=\hat{\dot{\eta}}_2,\\&\hat{x}_5=\hat{\dot{\beta}}_1,\ \hat{x}_6=\hat{\dot{\beta}}_2,\ \hat{x}_7=\hat{\varsigma}_1,\ \hat{x}_8=\hat{\varsigma}_2,\\&\hat{x}_9=\hat{\eta}_1,\ \hat{x}_{10}=\hat{\eta}_2,\ \hat{x}_{11}=\hat{\beta}_1,\hat{x}_{12}=\hat{\beta}_2,\\&\hat{x}_{13}=\hat{W}_{11},\ \hat{x}_{14}=\hat{W}_{21},\ \hat{x}_{15}=\hat{W}_{31},\hat{x}_{16}=\hat{W}_{41},\\&\hat{x}_{17}=\hat{W}_{12},\ \hat{x}_{18}=\hat{W}_{22},\ \hat{x}_{19}=\hat{W}_{32},\ \hat{x}_{20}=\hat{W}_{42}\end{aligned}\tag{16}$$

Applying the convolution integral property [11], the remaining constraint equations can be derived in order to complete the system. Constraint equations obtained from Wagner's indicial theory are expressed as:

$$\begin{aligned}&\dot{\hat{x}}_{13}=\hat{x}_9-\frac{\hat{\varepsilon}_1}{k}\hat{x}_{13},\ \dot{\hat{x}}_{14}=\hat{x}_9-\frac{\hat{\varepsilon}_2}{k}\hat{x}_{14},\\&\dot{\hat{x}}_{15}=\hat{x}_{11}-\frac{\hat{\varepsilon}_1}{k}\hat{x}_{15},\ \dot{\hat{x}}_{16}=\hat{x}_{11}-\frac{\hat{\varepsilon}_2}{k}\hat{x}_{15},\\&\dot{\hat{x}}_{17}=\hat{x}_{10}-\frac{\hat{\varepsilon}_1}{k}\hat{x}_{17},\ \dot{\hat{x}}_{18}=\hat{x}_{10}-\frac{\hat{\varepsilon}_2}{k}\hat{x}_{18},\\&\dot{\hat{x}}_{19}=\hat{x}_{12}-\frac{\varepsilon_1}{k}\hat{x}_{19},\ \dot{\hat{x}}_{20}=\hat{x}_{12}-\frac{\varepsilon_2}{k}\hat{x}_{20},\end{aligned}\tag{17}$$

The aeroelastic system can finally be written in a state-space form as:

$$\left\{\dot{X}\right\}=\left[U\left(q_e,k\right)\right]\left\{X\right\}+\left[V\right]_{NLIN}\left\{X\right\}\tag{18}$$

where $\left[U\right]$ is a matrix containing linear terms that are functions of the equilibrium solution and $\left[V\right]_{NLIN}$ is a matrix containing only non-linear terms. Linear flutter speed calculations can be performed setting the matrix $\left[V\right]_{NLIN}$ equal to zero. The stability of motion about the equilibrium operating condition is determined by the eigenvalues of the $\left[U\right]$ matrix. The reduced linear perturbation system originates a linear approximation of the behaviour of the system in the neighborhood of the static equilibrium point with the possibility of calculating a flutter speed for each trim condition. Linear flutter speed can be computed assuming the equilibrium static configuration as zero with no coupling effect computing eigenvalues of $\left[U\left(......,v_s=0,w_s=0,\phi_s=0\right)\right]$. Including equilibrium terms, non-linear flutter speed calculations can be performed computing eigenvalues of $\left[U\left(......,v_s\neq 0,w_s\neq 0,\phi_s\neq 0\right)\right]$. The system response is then analyzed via time marching integration by the non-linear Mathematica® solver. Linear integration, maintaining $\left[V\right]_{NLIN}=0$, or non-linear integration, $\left[V\right]_{NLIN}\neq 0$, can be carried out to investigate the post-flutter behaviour.

3 PRELIMINARY RESULTS

The procedure presented in the previous sections has been validated with the Goland bending-torsion flutter for a uniform cantilever wing, Ref [21]. The advanced aeroelastic model is reduced to the classical one by means of elimination of flapping displacement under static load (v_s, w_s, ϕ_s). Main wing characteristic has been introduced in the code according to cited references and a stiffness ratio Γ=44 has been used in the present calculation. Linear results for the flutter speed shown a critical speed of 489.42 Km/h and a flutter frequency of 71 rad/s that are in very good agreement with some of the results reported in Refs. [21-24]. To validate the non-linear aeroelastic model proposed in this paper, the models of Patil and Hodges [12] and Tang and Dowell [26] have been considered and comparisons have been carried out. The results presented are in very close agreement with the results of [12,26].

In addition to analytical and computational results, preliminary wind tunnel test has been conducted on an high-aspect-ratio balsa wood wing [4,6,7]

Firstly, the linear flutter speed (LFS) can be determined corresponding to the stability characteristics of the unloaded, undeformed wing. Secondly, one could trim the aircraft, or apply representative static loads on the wing and calculate the non-linear equilibrium position. The aeroelastic model can then be linearly reduced about the non-linear steady state to obtain a linear eigenvalue problem determining non-linear flutter speed (NLFS) condition. This analysis gives a more realistic prediction of the stability of the wing. For a given flow speed, typical velocity vs. damping plots can be determined in function of the static tip displacement assumed.

Table I - Base Configuration

k	variable
μ	11
Ω_h	198
Ω_α	892
Γ	44
x_α	0
r_α^2	0.25
a	-0.333
1/Λ	7

Preliminary linear and non-linear flutter calculations are reported in the following referring a base low aspect ratio configuration with aeroelastic parameters reported in Table I. The case of zero deflection static condition $w_{s\text{-}tip}/b=0$, shows a dimensionless LFS of 175 m/s. A typical reduction in the critical flutter speed has been obtained for a deformed static wing. Considering, for example, the case of $w_{s\text{-}tip}/b=0.415$, the flutter velocity decrease to a value of about 155m/s, showing a reduction of about 12% and higher reduction up to 30-35% can be otained considering higher aspect ratios wing as in Ref [4,6,7] and for the high aspect ratio configuration studied below.

For fixed values of others aeroelastic parameters, flutter is governed also by chord-wise dimensionless center of gravity location X_α .When X_α is negative, (referring to reference system of Figure 1, it means that center of gravity is behind the elastic center and the wing would be statically unstable in flight. In Figure 2 is reported Basic configuration LFS and NLFS as function of X_α , for the case of zero deflection static condition, and for an imposed deflected equilibrium with $w_{s\text{-}tip}/b$=0.415 respectively. It is possible to observe that for the configuration under investigation when nonlinear aeroelastic analysis is activated there is a much more sensitivity of flutter speed to variation of X_α respect to the case of LFS. Possible flutter speed reductions up to 50-60% are possible for special configurations with $X_\alpha < 0$ as shown in Figure 2.

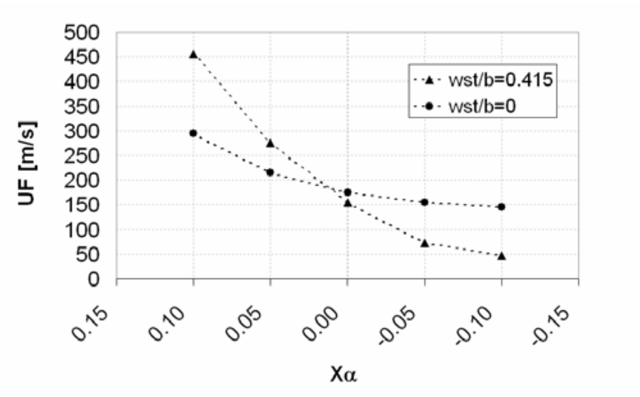

Figure 2 LFS & NLFS as function of X_α
(Low Aspect Ratio)

In order to study the typical aeroelastic behaviour of a high aspect ratio wing, the basic configuration has been modified and a classical high aspect ratio wing has been obtained and studied. High Aspect Ratio (HAR) wing aeroelastic parameters are reported in Table II.

Table II - High Aspect Ratio Configuration

	HAR wing
k	variable
μ	11
Ω_h	2.44
Ω_α	100
Γ	44
x_α	0
r_α^2	0.25
a	0
$1/\Lambda$	20

HARs wings undergo large deformations for relatively low aerodynamic loadings as compared to low-aspect-ratio wings, and the natural frequencies of the high-aspect-ratio wings are quite low. From simple formulae for natural frequencies of a beam-rod it is clear that torsional frequencies are inversely proportional to the length, while the bending frequencies are inversely proportional to the square of the length. Thus, the bending frequencies decrease at a higher rate than the torsional frequencies do as the wing span increases. High-aspect-ratio wings have a very low flapping frequency, while the lagging bending frequency seems to decrease on the same order as the torsional frequency. Under aerodynamic loading the wing exhibits static deflections, (a curved wing configuration), for which a non-linear coupling between torsion and lagging bending occurs.

The modal content of the statically undeflected HAR wing structure at zero speed consists of six modes, two flapping modes, two lagging modes and two torsional modes with frequency shown in table III.

Table III - Modal content HAR undeformed wing

Type	Theory [Hz]	Code (LIN) [Hz]
Mode 1 (2nd lag)	36.16	36.38
Mode 2 (2nd tors)	14.93	14.93
Mode 3 (1st lag)	5.81	5.81
Mode 4 (2nd flap)	5.45	5.48
Mode 5 (1st tors)	4.98	4.98
Mode 6 (1st flap)	0.88	0.88

In Table III are shown the natural frequencies for deformed HAR wing considering w_{tip}/b=1.

In Figure 3a-b a typical graphical representation of the eigenanalysis in the form of real eigenvalues (damping) vs. the flow velocity is presented for the HAR configuration. It is possible to identify a critical flutter speed of 45 m/s in correspondence to the lowest airspeed for which there is an intersection of damping with the velocity axis.

Considering an imposed wing static deflection with w_{tip}/b=1 (Figure 4a-b) initial modal content become different and it is not possible to recognize pure lagging and torsion modes.

Table IV - Modal content HAR deformed wing

Type	Code (NLIN) [Hz]
Mode 1 (2nd lag)	36.51
Mode 2 (2nd tors)	15.11
Mode 3 (1st lag-tors)	6.21
Mode 4 (2nd flap)	5.48
Mode 5 (1st tors-lag)	2.16
Mode 6 (1st flap)	0.88

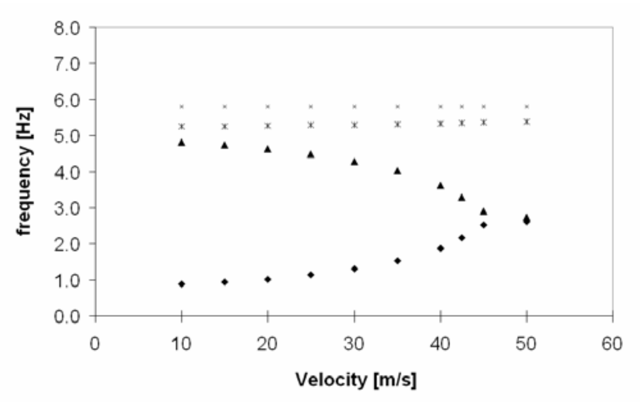

Figure 3a Frequencies (HAR wing $w_{st}/b=0$ $X_\alpha=0$)

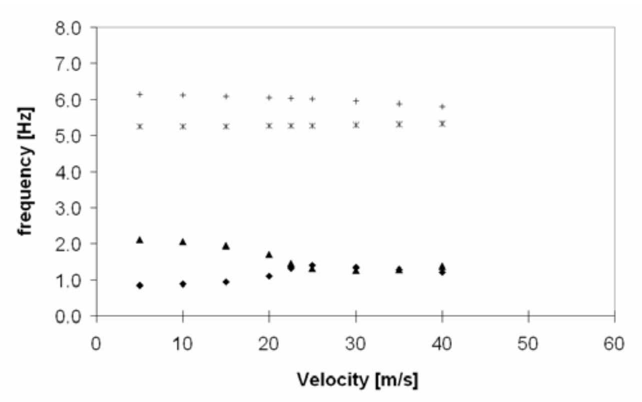

Figure 4a Frequencies (HAR wing $w_{st}/b=1$ $X_\alpha=0$)

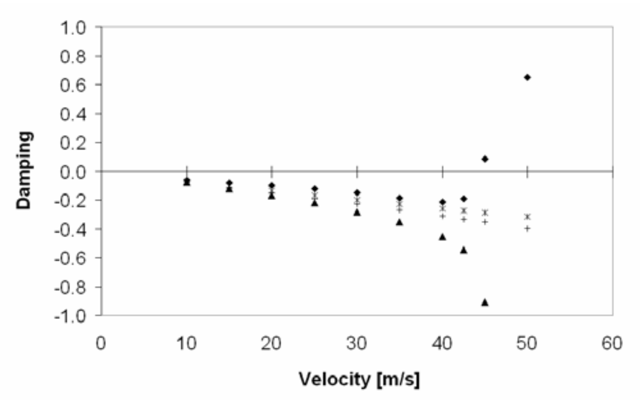

Figure 3b LFS (HAR wing $w_{st}/b=0$ $X_\alpha=0$)

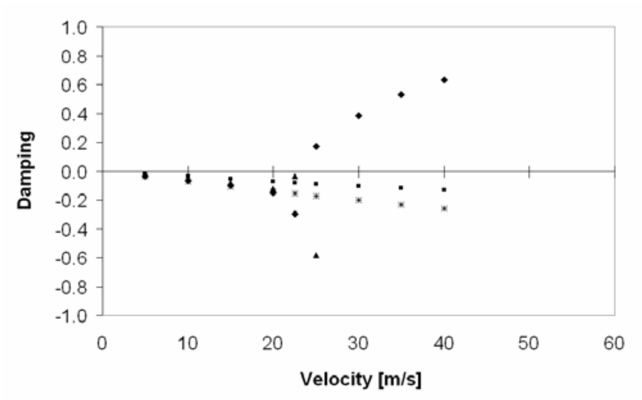

Figure 4b NLFS (HAR wing $w_{st}/b=1$ $X_\alpha=0$)

Comparing the previous aeroelastic analysis ($w_{tip}/b=0$) and the case with $w_{tip}/b=1$ a strong reduction of the flutter speed has been detected. It is possible to recognize a first critical condition at a very low speed (22.5m/s) due to the interaction between coupled lagging/torsion modes and flapping modes as reported in Figure 4a-b showing a strong reduction up to 50% that of the linear case.

The effect of eccentricity has been analyzed also for the HAR configuration (Figure 5).

In the case of undeformed HAR wing the behaviour is similar to the base configuration, showing an increased LFS when a positive value of X_α is considered even if the sensitivity is less important than the lower aspect ratio case. Both for undeformed $w_{st}/b=0$ and deformed wing $w_{st}/b=1$ have flutter speed variation of about 10-12% consistent with the case with $X_\alpha=0$. It is possible to conclude that the elastic eccentricity could have an important role in designing an advanced UAV but the positive role of an increased X_α is present with less influence in the case of a high aspect ratio wing as shown in figure 5.

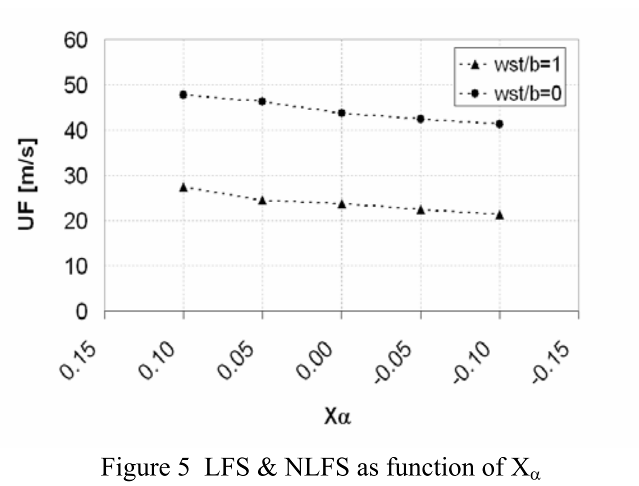

Figure 5 LFS & NLFS as function of X_α (High Aspect Ratio)

4 CONCLUSIONS

Highly flexible High Altitude Long Endurance (HALE) aircraft exhibit aeroelastic behaviors that are very different from conventional aircraft. In this paper, linear and non-linear flutter predictions are presented and applied to the aeroelastic performance of a slender HALE wing. For the second order non-linear structural model considered here, the effect of the static equilibrium configurations is taken into consideration when solving the perturbed aeroelastic system. The Galerkin approach is used to discretize the partial differential equations. Aerodynamic loads are derived according to the Wagner indicial function approach and are considered to be linear. The effect of tip deflection and elastic eccentricity is pointed out analysing a tipical low aspect ratio configuration and a tipical high aspect ratio configuration. The eccentricity parameter seems to play a central role in the design of low aspect ratio wings due to the important variation in the flutter speed. The tip deflection for the same case has a reduced effect. On the contrary the tip deflection is considered more important in the design of high aspect ratio wings while the eccentricity parameter introduces limited changes in the flutter boundary.

ACKNOWLEDGEMENTS

The authors would like to thank Prof. Pier Marzocca for his essential help during the derivation of system equations and discussion.

REFERENCES

[1] Romeo G., Design of High Altitude Very-Long Endurance Solar Powered Platform for Earth Observation and Telecommunication Applications. Aerotecnica Missili E Spazio, 1998, 77 (3-4), pp. 88-99.

[2] Romeo G., Frulla G., Cestino E., Corsino G. HELIPLAT: Design, Aerodynamic, Structural Analysis of Long-Endurance Solar-Powered Stratospheric Platform*.* *AIAA Journal of Aircraft,* Vol. 41, No. 6 , pp. 1505-1520. 2004.

[3] Romeo G., Frulla G., HELIPLAT: High Altitude Very-Long Endurance Solar Powered UAV for Telecommunication and Earth Observation Applications" T*he Aeronautical Journal*, Vol.108 (1084), pp. 277-293, 2004.

[4] Cestino E., Design of solar high altitude long endurance aircraft for multi payload and operations, *Journal of Aerospace Science and Technology* ,Vol. 10 Issue 6 , pp. 541-550, 2006.

[5] Frulla G. Aeroelastic Behavior of a Solar-Powered High-Altitude Long Endurance Unmanned Air Vehicle (HALE-UAV) Slender Wing *Journal of Aerospace Engineering*, Vol. 218, Part G, Special Issue, No. G3, June 2004, pp. 179-188.

[6] Romeo G., Frulla G., Cestino E., Marzocca P., Tuzcu I. Nonlinear Aeroelastic Modelling and Experiments of Flexible Wings, *Proc. of 47th AIAA/ASME/ ASCE/AHS/ASC Structures, Structural Dynamics, Materials Conference,* Newport RI, 1-4 May, 2006.

[7] Romeo G.,Frulla G., Cestino E., Marzocca P., Non-linear Aeroelastic Behavior of Highly Flexible HALE Wings, *Proc. 25th ICAS Congress* 3-8 September 2006, Hamburg Germany, 11 pages.

[8] Bisplinghoff R.J., Ashley H., Halfman R.L., Aeroelasticity. Addison-Wesley Publishing Company Inc. Reading, Massachusetts, 1957.

[9] Hodges D.H., Dowell E.H. Nonlinear Equations of Motion for the Elastic Bending and Torsion of Twisted Non Uniform Rotor Blades, *NASA TN D-7818*, 1974.

[10] Crespo Da Silva M.R.M., Glynn C.G., Nonlinear Flexural-Flexural-Torsional Dynamics of Inextensional Beams. Equations of Motion. *Journal of Structural Mechanics,* Vol. No. 6(4), pp. 437-448, 1978.

[11] Sedaghat A., Cooper J.E., Wright J.R., Prediction of Non-Linear Aeroelastic Instabilities, *Proc. ICAS 2000 Congress*, Harrogate, UK, 28 August-1 September.

[12] Patil M.J., Hodges D.H., On the Importance of Aerodynamic and Structural Geometrical Non-linearities in Aeroelastic Behavior of High-Aspect-Ratio Wings, *Journal of Fluids and Structures*, Vol. 19, pp. 905-915, 2004.

[13] Beddoes T.S., A Synthesis of Unsteady Aerodynamic Effects Including Stall Hysteresis, *Vertica* 1976; 1:113-23.

[14] Leishmann J.G., Beddoes T.S., A Semi-Empirical Model for Dynamic Stall, *Journal Am. Helicopter Soc.* Vol.34, 1989, pp 3-17.

[15] Kim D.-H., Lee I., Marzocca P., Librescu L., Schober S. Nonlinear Aeroelastic Analysis of an Airfoil Using CFD-Based Indicial Approach, *Journal of Aircraft*, Vol. 42, No.5, September–October 2005, pp. 1340-1344.

[16] Hodges D.H., Ormiston R.A. Non-linear Equations for Bending of Rotating Beams with Application to Linear Flap-Lag Stability of Hingeless Rotors. *NASA TM* X-2770, 1973.

[17] Meirovitch L., Fundamentals of Vibrations, McGraw Hill, New York, 2001.

[18] Nichkawde C., Strganac T.W., Nonlinear Aeroelastic Response of the Flexible Wing in Trim, *Proc. AIAA/ASME/ASCE/AHS/ASC Structures, Structural Dynamics, Materials Conference*, Newport RI, 1-4 May, 2006.

[19] Cestino E., Design of very long-endurance solar powered UAV, *PhD Dissertation* Politecnico di Torino, Aerospace Dept. , Torino, 2006.

[20] Marzocca P., Librescu L., Chiocchia G. Aeroelastic Response of a 2-D Lifting Surfaces to Gust and Arbitrary Explosive Loading Signatures, International

Journal of Impact Engineering, Vol. 25, No. 1, January 2001, pp. 41-65.

[21] Goland M., The Flutter of a Uniform Cantilever Wing, *Journal of Applied Mechanics*, Vol. 12, No. 4, 1945, pp. A-198–A-208.

[22] Goland M., and Luke Y. L., The Flutter of a Uniform Wing with Tip Weights, *Journal of Applied Mechanics*, Vol. 15, No. 1, 1948, pp. 13-20.

[23] Marzocca P., Librescu L., Silva W. A., Aeroelastic Response and Flutter of Swept Aircraft Wings, *AIAA Journal*, Vol. 40, No. 5, May 2002.

[24] Patil M.J., Hodges D.H., Nonlinear Aeroelasticity and Flight Dynamics of Aircraft in Subsonic Flow", *Proc. of the 21st Congress of International Council of the Aeronautical Sciences ICAS*, Melbourne, Australia, September 1998.

[25] Patil M.J., Hodges D.H., Limit-Cycle Oscillations in high-aspect-ratio wings, *Journal of Fluids and Structures*, Vol. 15, pp. 107-132, 2001.

[26] Tang D., Dowell E.H., Experimental and Theoretical Study on Aeroelastic Response of High-Aspect-Ratio Wings, *AIAA Journal*, Vol. 39, No. 8, pp. 419-429, 2001.

ISSN 1590-8844
International Journal of Mechanics and Control, Vol. 08, No. 01, 2007

DEVELOPMENT OF A CONTROL STRATEGY FOR A VARIABLE CAMBER SUSPENSION

I. Kuwayama*, F. Baldoni**, F. Cheli*

*Politecnico di Milano, Department of Mechanical Engineering
**Bridgestone Technical Center Europe S.p.A.

ABSTRACT

Prior research into the application of controlled suspension systems concerning ride comfort and driving stability performance is widely accepted. In fact, active suspension systems have been introduced to production vehicles. However, when it comes to handling performance while a vehicle is turning, drivers are still missing the tire's potential due to the presence of wheel alignment changes imposed by suspension K&C. A study of the camber's influence on tire response has been carried out by Bridgestone Corp. based on measurements performed by Flat-Trac III. The results reveal that the cornering force is strongly dependent on the camber angle, especially when the tire is working on a large slip angle regime. From a tire dynamics point of view, a positive camber, largely caused by a vehicle roll motion, decreases the adhesion level, which eventually limits handling performance, such as maximum lateral acceleration. The concept of a variable camber suspension comes from the idea of making the most of tire performance with optimized camber angles depending on vehicle behavior. In order to evaluate the potential of the variable camber suspension, optimizations of the camber angles of each one of wheels in particular maneuvers have been carried out.
Although this topic is fascinating, it has turned out to be challenging because a few reports related to the active camber control technology have been presented [1,2]. This also explains why a small number of references appear at the end of this paper [1,2,3]. An 18 dofs numerical vehicle model equipped with the variable camber suspension has been developed to investigate the efficiency of the active system in comparison to a passive model for which the optimal camber angle functions are introduced and optimized as an electronic controller. The characteristics of the passive model are derived from ADAMS full vehicle model and are validated with an actual vehicle on the track. The details of the numerical vehicle models are going to be published [3]. The simulation results in this paper demonstrate improved handling performance in terms of steady-state, limit, and transient maneuvers. It has been concluded that the variable camber system has a strong impact on handling performance. Therefore, further investigations are going to be carried out.

Keywords: Active Control, Optimization, Variable Camber, Vehicle Model, Vehicle Dynamics.

1 INTRODUCTION

The requirements of vehicle behavior relating to tire performance have become so diversified and complicated. One of the reasons why tire manufactures must develop exclusive tires for each new vehicle stems from the characteristics of suspensions, namely the behavior of camber angle, toe angle, etc. In fact, these characteristics vary according to the design concept of each car manufacturer, and a different vehicle obviously has a different characteristic. These suspension characteristics have constraints on the tire alignments. Normally, this condition leads to the tire's loss of potential. Fig.1 shows typical examples of cornering force curves in terms of a camber influence, which has been carried out on a Flat-Trac III at Bridgestone Technical Center Europe: the

Contact author: Isao Kuwayama

Via La Masa 34, 20158 Milano, Italy

drawing of tire sections shows a relationship between a camber angle, γ, lateral force, F_y, and steering direction indicated by the red dashed line in order to visualize general and unrealistic conditions underlined in Fig.1.

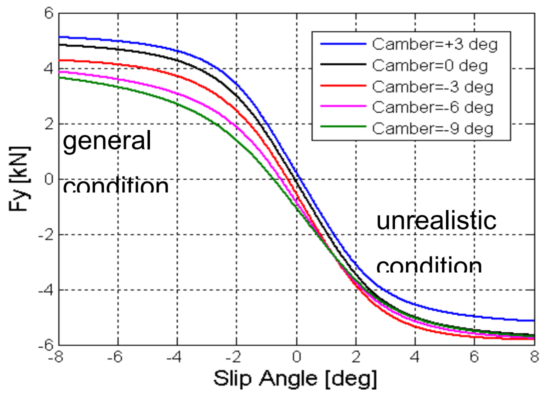

Figure 1 Cornering force curves with different camber angles at Fz=4500 N and I.P.=2.2 bar.

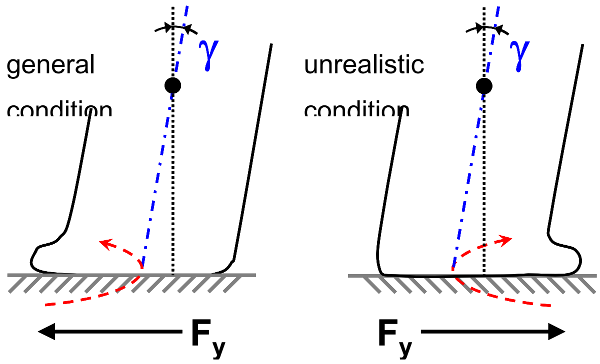

Figure 2 General and unrealistic conditions indicate positive and negative camber situations respectively.

According to the figure above, it can be seen that the unrealistic condition can provide higher and more consistent cornering forces in comparison to the general condition. Usually, as a lateral acceleration increases along with a roll angle while a vehicle is turning, tires tend to lean toward an external direction, which eventually limits tire performance due to an increase of the positive camber angle. If the camber angle can be directly controlled in order to realize and utilize the unrealistic tire alignments in general, vehicle handling performance would be improved; however, it should be noted that optimum handling performance can not be achieved by simply applying higher tire forces. In order to realize maximum handling performance depending on vehicle conditions as much as possible, an adequate control strategy must be developed based on an extensive knowledge of vehicle dynamics. The investigations presented in this paper have been focusing on the development of the control strategy that maximizes the handling performance in following three different basic maneuvers which enable us to evaluate steady-state, limit, and transient performance:

- Ramp-steer maneuver for steady-state performance,
- Step-steer maneuver for limit performance,
- Swept-steer maneuver for transient performance.

The optimum combination of non-linear camber angle functions for each one of the wheels in different vehicle conditions has been examined through optimization analyses; on-board sensor signals coupled with constant and variable coefficients build up the camber angle functions for each one of wheels independently.

2 SIMULATION MODEL

The 18 dofs numerical vehicle model has been developed by the author to investigate the potential of the variable camber suspension in detail while a sportive front-engine rear-drive vehicle has been chosen as a passive vehicle to be improved. The details of the description of the simulation model can be found in the paper [3] which is going to be published: the nomenclature of the system is presented in Appendix A.

2.1 VEHICLE MODEL

Both passive and active numerical vehicle models have been developed and these models describe the vehicle dynamics through the following dofs:

- 6 d.o.f. for the rigid chassis,
- 4 d.o.f. for the vertical displacements between unsprung mass and chassis,
- 4 d.o.f. for the wheel rotations,
- 4 d.o.f. for the variable camber rotations of the active suspension.

The passive model [3] has been constructed by the first 14 dofs of the above list. The dofs can be collected into $\underline{q}_p$ as a generalized vector which can be written in the following form:

$$\left\{\underline{q}_P\right\} = \left\{\begin{matrix}\underline{q}_{Ps}\\ \underline{q}_{Pu}\end{matrix}\right\} = \left\{\begin{matrix}\begin{bmatrix}X & Y & Z & \psi & \theta & \rho\end{bmatrix}^t \\ \begin{bmatrix}z_{u,1} & z_{u,2} & z_{u,3} & z_{u,4} & \theta_{u,1} & \theta_{u,2} & \theta_{u,3} & \theta_{u,4}\end{bmatrix}^t\end{matrix}\right\} \quad (1)$$

(See Fig.4 and Appendix A for further explanation)

The state space equation of the vehicle model can be expressed as:

$$[M]\{\dot{\underline{x}}\} = [A]\cdot\{\underline{x}\} + [B]\cdot\{\underline{f}_{TS}\} + [F]\cdot\{\underline{f}_{EX}\}$$

where $$\{\underline{x}\} = \left\{\begin{matrix}\underline{q}_P\\ \dot{\underline{q}}_P\end{matrix}\right\} \quad (2)$$

The force vector, f_{TS}, represents tire and suspension forces while the other force vector, f_{EX}, represents external forces.

The matrices, [A] and [B], are time-varying matrices while the matrix, [F], and the mass matrix, [M], are constant. The vehicle model has been equipped with a driveline model consisted of engine and differential [5], a tire model by Magic Formula 5.2 [4], and a suspension model with multi-dimensional maps derived through ADAMS Bench Rig Simulations. The simulation model for the passive vehicle is shown in Fig.3 and 4. An initial velocity, V_0, and a time history of a steering wheel angle, δ_H, are the input variables to launch open-loop handling simulations.

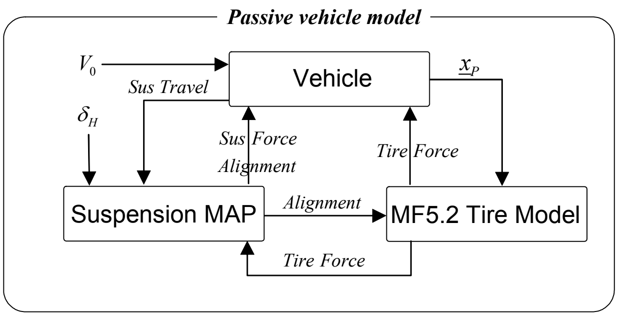

Figure 3 The passive vehicle system.

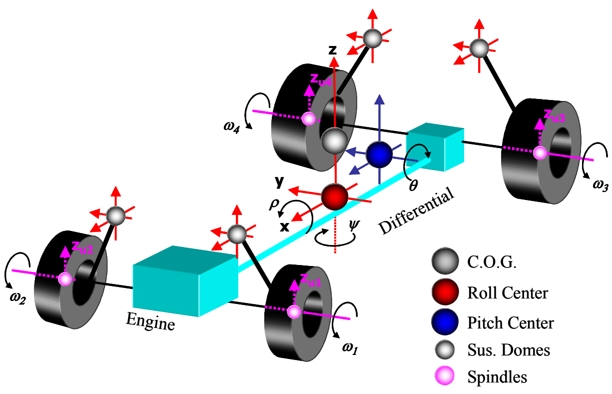

Figure 4 Degrees of freedom for the passive vehicle.

The passive vehicle model is extensively validated in terms of the entire chassis, tires, and vehicle components; therefore, reliable vehicle behavior can be observed with properly identified parameters. The simulations can be driven by a simple driver model which handles a throttle level.

In the case of the active model, it has been built up by all the dofs listed above. A generalized vector, q_A, for the active vehicle can be written as:

$$\{q_A\} = \begin{Bmatrix} q_{As} \\ q_{Au} \end{Bmatrix} = \begin{Bmatrix} \begin{bmatrix} X & Y & Z & \psi & \theta & \rho \end{bmatrix}' \\ \begin{bmatrix} z_{u,1} & z_{u,2} & z_{u,3} & z_{u,4} & \theta_{u,1} & \theta_{u,2} \\ \theta_{u,3} & \theta_{u,4} & \gamma_{a,1} & \gamma_{a,2} & \gamma_{a,3} & \gamma_{a,4} \end{bmatrix}' \end{Bmatrix} \tag{3}$$

where the terms, $\gamma_{a,i}$, indicate additional degrees of freedom in terms of active camber angles (see Fig.6 and Appendix A for further explanation). The details are presented in a subsequent section. As for a state space equation for the active vehicle model, Eq.(2) can be utilized with proper parameter constants and variables in particular matrices and vectors as well. In order to obtain a realistic interaction between the active suspension and chassis in this numerical simulation model, a physical variable camber suspension model has been developed to derive its characteristics through ADAMS bench rig simulations as it has done for the passive one [3]. A camber angle controller, for which a control strategy and an optimization procedure are presented in this paper, is implemented on the active vehicle. Activations of actuators built in the active suspensions can be handled by PID controllers; the differences of the camber angle signals between the optimum values given by the camber angle controller and the current values of the vehicle system are minimized by the PID controllers as seen in Fig.5.

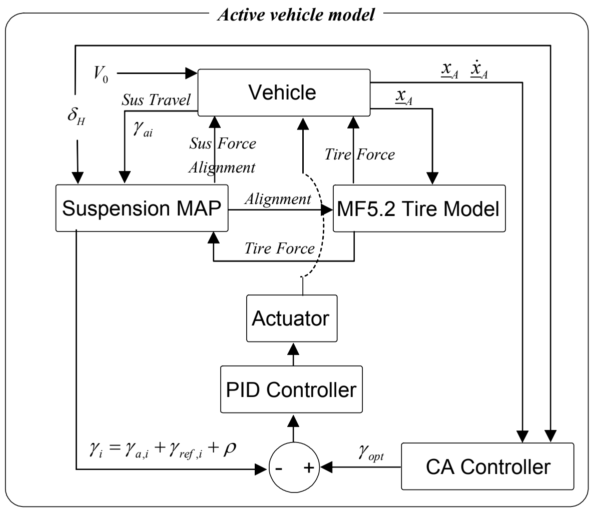

Figure 5 The active vehicle system.

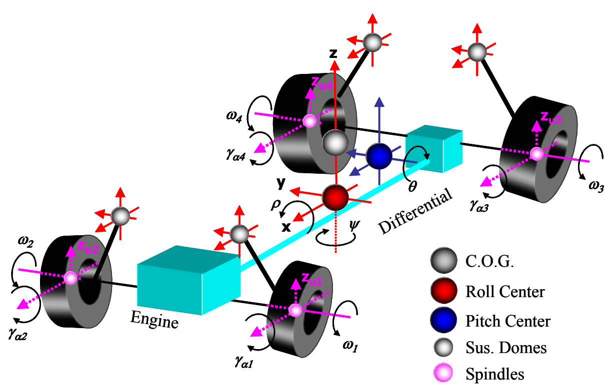

Figure 6 Degrees of freedom for the active vehicle.

2.2 SUSPENSION MODEL

The suspension maps implemented in the models are capable of reproducing tire alignments, jacking forces, and damper alignments and positions. The active suspension model with a movable upright and an actuator has been developed to create the active suspension maps that can reproduce the dynamic interaction of the active system. Fig.7 and 8 show both the passive and active multi-body suspension models; an equation of motion in terms of the camber rotation is derived based on the assumption that the rotation would take place in a 2-D vertical plane. In addition to the input signals for passive maps such as suspension travels, those of opposite side, steering wheel angle, and tire component forces, one of the state variables, $\gamma_{a,i}$, is added as the additional input signal for the active maps. Further details about the modelization techniques applied for the vehicle and suspension models are fully presented in the paper [3].

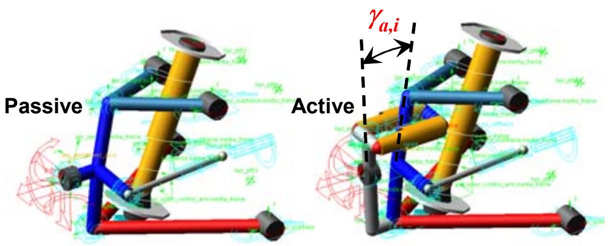

Figure 7 The multi-body suspension models.

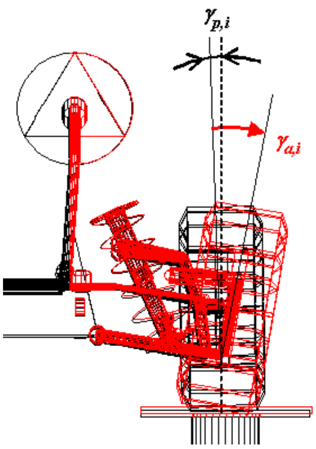

Figure 8 The active suspension model superimposed on the passive one.

2.3 TIRE MODEL

MF5.2 Tire Transient Model [4] is implemented on the vehicle model. Relaxation lengths of a longitudinal force and a lateral force, σ_κ and σ_α, can be expressed as:

$$\sigma_\kappa = Fz\cdot\left(Ptx1 + Ptx2\cdot dfz\right)\cdot\exp\left(-Ptx3\cdot dfz\right)\cdot\left(R_0/Fz_0\right) \tag{4}$$

$$\sigma_\alpha = Pty1\cdot\sin\left(2\arctan\left\{\frac{F_z}{\left(Pty2\cdot F_{z_0}\right)}\right\}\right)\cdot\left(1-Pky3\cdot|\gamma|\right)\cdot R_0 \tag{5}$$

where γ is a camber angle with respect to the ground. MF coefficients, *Ptx*, *Pty*, and *Pky*, are depending on tire models (see Appendix A). Furthermore, first-order lag of tire longitudinal and lateral deformation, u and v, is introduced through relaxation lengths above as:

$$\sigma_\kappa\frac{du}{dt} + |V_x|u = -\sigma_\kappa V_{sx} \tag{6}$$

$$\sigma_\alpha\frac{dv}{dt} + |V_x|v = \sigma_\alpha V_{sy} \tag{7}$$

Finally, the practical tire deformation slip quantities, κ' and α', are defined instead of the longitudinal and lateral wheel slip quantities κ and α as:

$$\kappa' = \frac{u}{\sigma_\kappa}\cdot\operatorname{sgn}\left(V_x\right) \tag{8}$$

$$\alpha' = \arctan\left(\frac{v}{\sigma_\alpha}\right) \tag{9}$$

The tire models presented in this paper are provided and validated on Flat Trac III by Bridgestone T.C.E. Not to mention that the same tire models for front and rear respectively used by the referring ADAMS full vehicle model are utilized by the passive and active numerical vehicle models as well.

3 CONTROL STRATEGY

Generally, handling performance of a real vehicle can be evaluated in two different ways, namely subjective and objective evaluations. In the former case, it requires a skilful driver who has considerable experiences to detect both advantages and disadvantages of the coupled performance of vehicle and tire; on the other hand, in the latter case, it requires not only accurate but also high resolution capable sensors, a data acquisition system, and a large space to perform objective handling maneuvers to measure specific values and curves, which characterize fundamental but significantly important vehicle features represented by understeer/sideslip gradients, vehicle frequency response to handle input, etc. Both methods can be virtually performed by simulations with proper simulation models; furthermore, numerical simulations have great advantages in terms of repeatability, which is one of the major issues of the objective handling tests. Therefore, the improvements achieved by an active control system can be clearly identified in particular expressions through objective handling campaigns, for which the control strategy has been developed.

Table I - List of Objective Performance and Target

Maneuver	Objective Performance	Target	
Ramp-steer	Steady-state behavior	Reduction of Understeer Gradient at linear regime and 0.8G	-15%
			-60% (0.8g)
		Reduction of Sideslip Gradient at linear regime and 0.8G	-10%
			-30% (0.8g)
		Increase of Maximum Lateral Acceleration	+15%
Step-steer	Limit behavior	Reduction of Yaw Rate Peak to Peak Value	-30%
		Reduction of Yaw Rate Damping Time	-20%
		Reduction of Peak of Side Slip Angle	-30%
Swept-steer	Transient behavior	Reduction of Max/Static Yaw Rate Gain Ratio	-40%

As it is underlined in the prior section, three types of handling tests are chosen to evaluate handling performance in terms of steady-state, limit, and transient behavior. Table I shows performance targets to be achieved by the active vehicle. In order to satisfy each target, optimization analyses have been carried out with a trust region method which solves the nonlinear curvefitting problem in the least squares sense.

3.1 OPTIMIZATION PROCEDURE

In general, a set of on-board sensor signals goes into an electronic controller to give appropriate orders for their actuator modules in order to improve designated vehicle performance. In this case, a couple of realistic sensor signals, such as lateral acceleration A_y, yaw velocity $\dot{\psi}$, and acceleration $\ddot{\psi}$, and steering wheel angle δ_H, has been chosen to construct camber angle functions for each one of the wheels. The camber angle function can be written as:

$$\gamma_{opt,i} = f_{Ay,i} \cdot A_y + f_{\dot{\psi},i} \cdot \dot{\psi} + f_{\delta_H,i} \cdot \delta_H + f_{\ddot{\psi},i} \cdot \ddot{\psi} \qquad (10)$$

where i indicates acronyms of internal/external and front/rear as: if, ef, ir, er. The coefficients, $f_{x,i}$, are assumed to be constant for each one of the wheels apiece for the convenient of the optimization analysis. These coefficients play an important role in the optimization as parameter variables which totally make 16 parameters. These parameters, which can be classified into four groups (Internal Front, External Front, Internal Rear, and External Rear), have been optimized to achieve the targets through the optimization analysis. After the optimization, dependencies of these optimized constant coefficients in terms of vehicle velocity, lateral acceleration, etc. have been examined to guarantee the advanced performance in different conditions: the details are presented in a subsequent section. Since the performance targets are explicitly indicated above, it is possible to specify objective functions for each maneuver to be minimized in order for the active vehicle to achieve particular target curves or values.

As for a ramp-steer maneuver, Fig.9 shows handling and sideslip diagrams with a target curve on the figures for the passive vehicle. The residuals between the curves can be considered as the objective functions, $f_{obj1}(A_y)$ and $f_{obj2}(A_y)$, to be minimized.

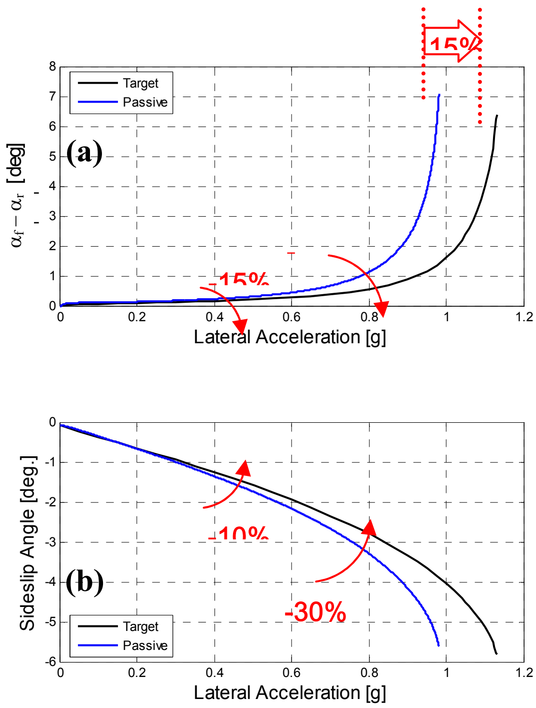

Figure 9 Ramp-steer maneuver at 100km/h: (a) Handling and (b) Sideslip diagram of the passive vehicle with the target curve.

Concerning a step-steer maneuver, Fig.10 shows a response of yaw rate and sideslip angle by the maneuver. In this case, the objective targets can be specified by constant values; the objective functions, the peak to peak yaw rate value $\dot{\psi}_{PP}$, the yaw rate damping time $\dot{\psi}_{damp}$, and the peak value of sideslip angle β_{peak}, are shown in Fig.10.

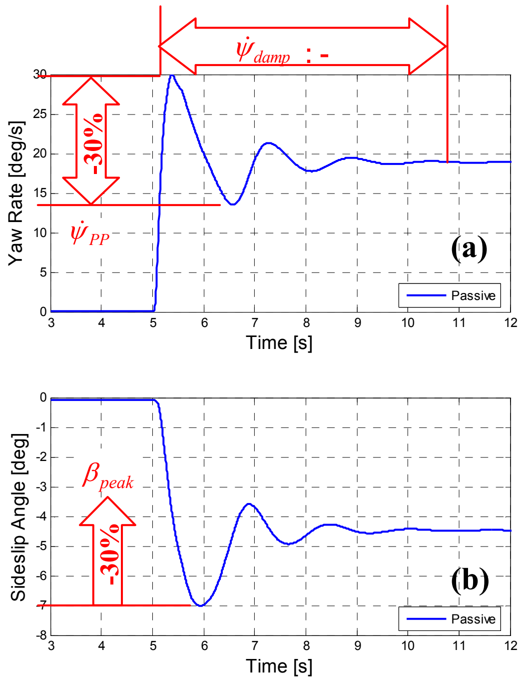

Figure 10 Step-steer maneuver at 100km/h: (a)Yaw Rate and (b) Sideslip Response of Passive Vehicle.

Last but not least, the target in terms of a frequency response of yaw rate must be taken into account. However, the operating range in terms of on-board sensor signals is basically included in the ramp-steer maneuver; therefore, the different control logic would cause some conflict between them. Accordingly the optimized parameters for a ramp-steer have been to applied to swept-steer maneuvers although different optimization analyses could have been performed to minimize the Max/Min Yaw Rate Gain Ratio independently. Fig.11 shows a flow of the optimization process which is capable of taking multiple objective functions into account. By introducing a loop routine, the optimization can find local peaks within a design field under constraints to obtain better results, which eventually leads to the true optimum solution as shown in the figure below. In addition, each one of the parameter variables has a constraint to share a controllable camber angle tolerance between the members of Eq.(10).

3.2 RAMP-STEER MANEUVER

Measurements of steady-state behavior by a ramp-steer maneuver can widely duplicate real driving situations from a linear behavior until limit of a vehicle within very short time, which would make thermal effects on the tires less sensitive and decrease excessive wears during the test campaign repetitions. In order to achieve the steady-state performance target by means of the variable camber suspension, optimization analyses of the camber angle distributions for the each wheel depending on the vehicle behavior have been carried out under the simulation parameters listed on Table II.

Table II - Ramp-steer simulation parameters

Total Time	Time step	Velocity	Gear	Steering Ramp	Start Time
[s]	[s]	[km/h]	[-]	[deg./s]	[s]
15	0.005	100	4	15	5

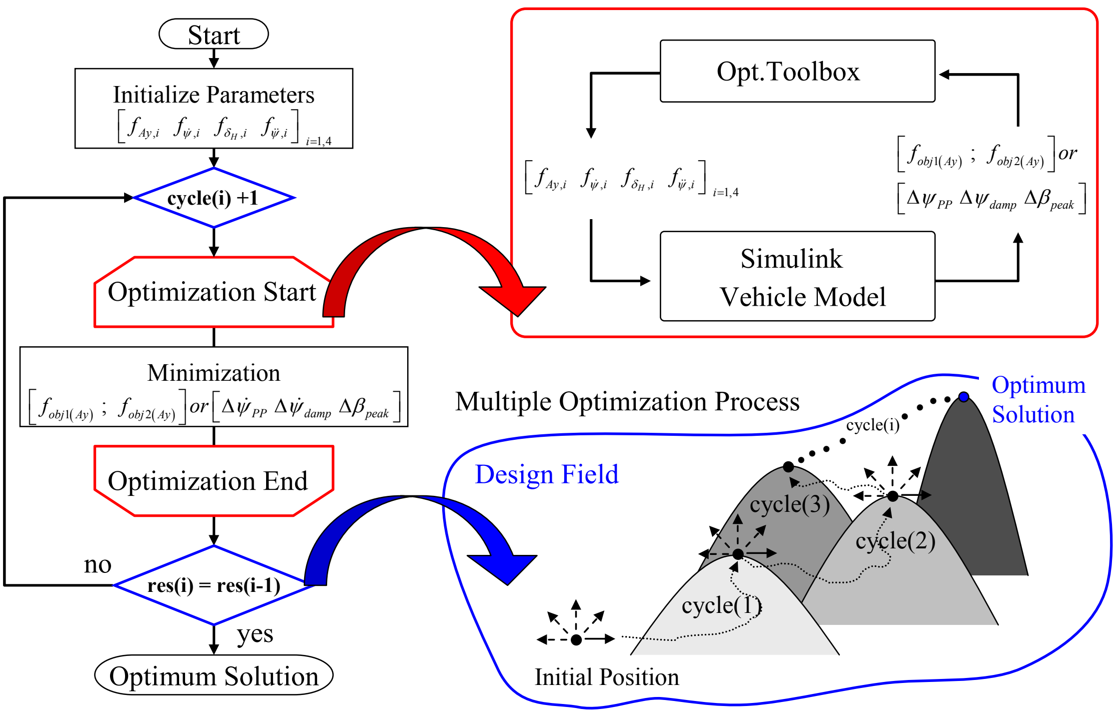

Figure 11 Multiple optimization flow for nonlinear multi-objective functions

ISSN 1590-8844
International Journal of Mechanics and Control, Vol. 08, No. 01, 2007

Fig.12 shows a result of the optimization. As seen in these figures, the objective functions represented by the residuals are appreciably minimized.

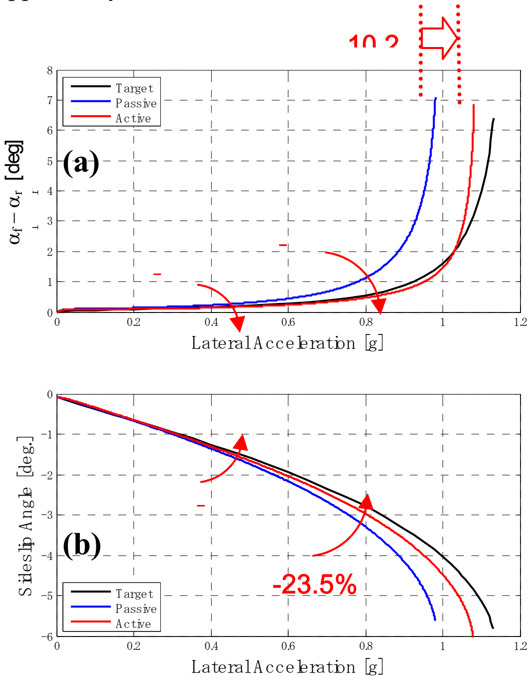

Figure 12 Ramp-steer maneuver at 100km/h:
(a) Handling and (b) Sideslip diagram of the passive and active vehicle with the target curve.

Fig.13 (a) and (b) show time histories of the camber angles with respect to the ground; a sign of the curves indicate positive/negative direction of the wheels as shown in Fig.2. Fig.14 shows actuator forces for one of the cylinders (see Fig.7) assigned by PID controllers. As seen in Fig.5, the PID controllers minimize the differences between optimum camber angles, $\gamma_{opt,i}$, and current camber angles, γ_i. Since the variable camber project is in a design phase, the ideal actuators are considered in order to evaluate the best control strategy.

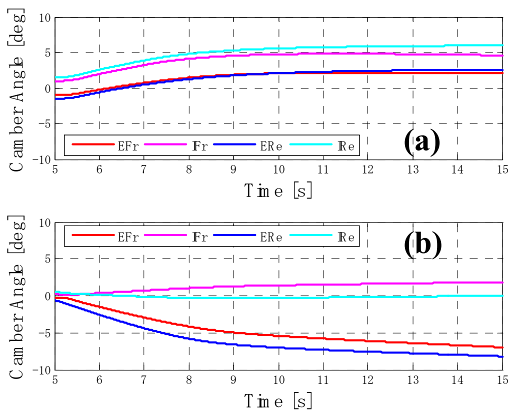

Figure 13 Ramp-steer maneuver at 100km/h:
Camber angles of the (a) passive and (b) active vehicle.

The real actuator, which meets the requirements specified through a series of investigations, is going to be looked for as a next step.

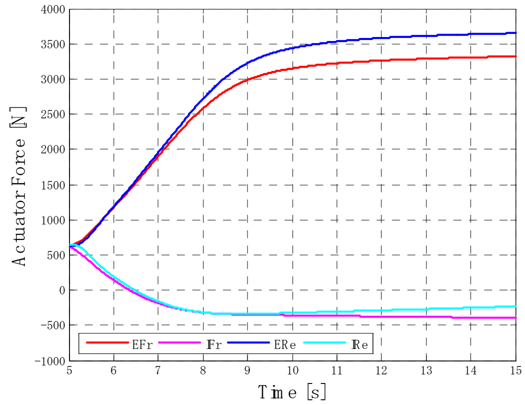

Figure 14 Ramp-steer maneuver at 100km/h:
Actuator forces

Fig.15 shows a comparison of four terms of Eq.(10) of the each wheel respectively. The sum of these members gives optimum camber angles with respect to the ground.

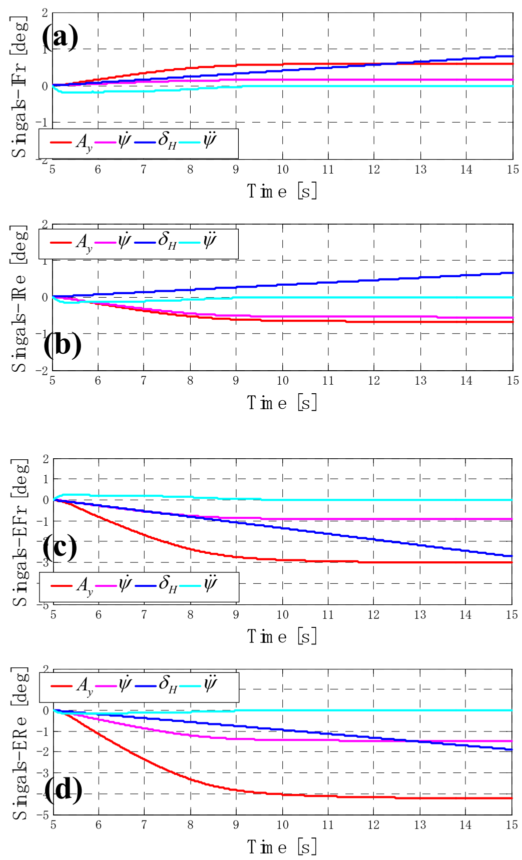

Figure 15 Ramp-steer maneuver at 100km/h:
Camber angle signals for the (a) internal front, (b) internal rear, (c) external front, and (d) external rear tire.

ISSN 1590-8844
International Journal of Mechanics and Control, Vol. 08, No. 01, 2007

The optimized parameters for Eq.(10) could work properly as long as the vehicle has been driven around a 100km/h; however, the input on-board signals notably vary with respect to a vehicle speed. Therefore, the speed dependencies have been taken into account. Essentially, steady state parameters can characterize passive vehicles behavior; moreover, the characteristic curves are not going to be varied according to the driving speeds. Fig.16 shows the handling and sideslip diagrams of the passive vehicle in different vehicle speed conditions. These figures clearly show the consistent steady-state characteristics of the passive vehicle as it should be and demonstrate the reliability of the presented numerical vehicle model.

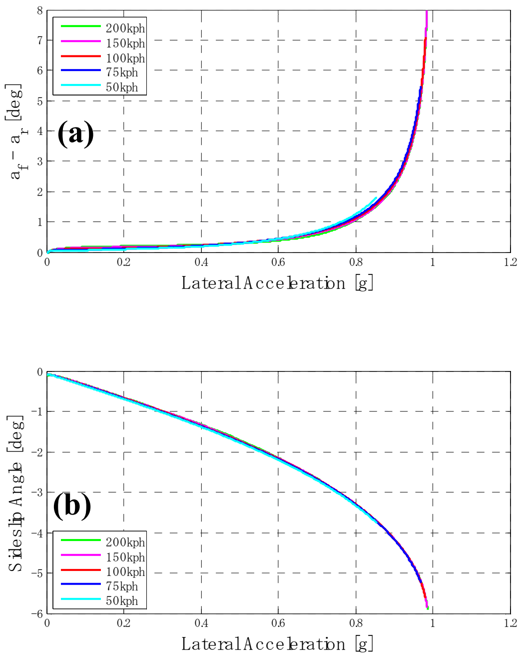

Figure 16 Ramp-steer maneuver at 50, 75, 100, 150 and 200km/h: (a) Handling and (b) Sideslip diagram of the passive vehicle.

As it is underlined above, the coefficients for input signals, such as yaw rate $\dot{\psi}$, yaw acceleration $\ddot{\psi}$, and steering wheel angle δ_H, are varied by the change of vehicle speed. Therefore, the coefficients of these signals must be variable functions. In this application, it has been derived as a map to ensure optimized performance in different conditions. The maps must have several axes with respect to a number of countermeasures; moreover, the number of the axes would increase when new counter measure is revealed as the investigation goes deeply. At the moment, in addition to the vehicle velocity, lateral acceleration is chosen as one of the axes of the multi-dimensional maps.

As discussed above, the vehicle velocity and lateral acceleration dependencies of each on-board sensor signals in steady-state condition have been examined. The ramp-steer maneuvers in different speeds have been performed in a similar condition as it has been done for the optimization but simply changed gear number in accordance with the vehicle speed. Firstly, the speed dependency of the steering wheel signal has been studied. Fig.17 shows a third term, $f_{\delta_H,i} \cdot \delta_H$, of Eq.(10) with the optimized constant coefficients, $f_{\delta_H,i}$, for the vehicle running at 100km/h.

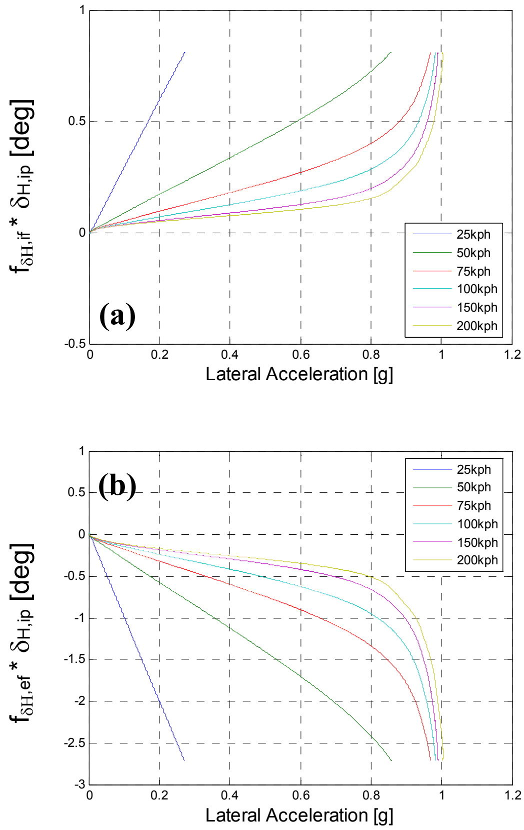

Figure 17 Ramp-steer maneuver at 25, 50, 75, 100, 150 and 200 km/h: responses of the third term of the camber angle function, $f_{\delta_H,i} \cdot \delta_H$, of the (a) internal front and (b) external front tire.

For the convenient of the following explanation, let the curve of 100km/h in Fig.17 be defined as a reference curve. As long as each one of the signals at a different vehicle speed follows the reference curve as the lateral acceleration increases, drivers can consistently expect improved handling performance by acquiring the optimized camber angle distribution for each wheel; however, in reality, they are largely diversified as shown in Fig.17. This is the reason why the variable coefficient maps for each referring on-board sensor signal must be introduced. Therefore, by creating and applying the variable coefficients, $f_{\delta_H,i}(v_H)$, as a function of the vehicle velocity instead of the constant one, all the modified curves of the handle input in the different vehicle speed can pursue the reference curve as shown in Fig.18.

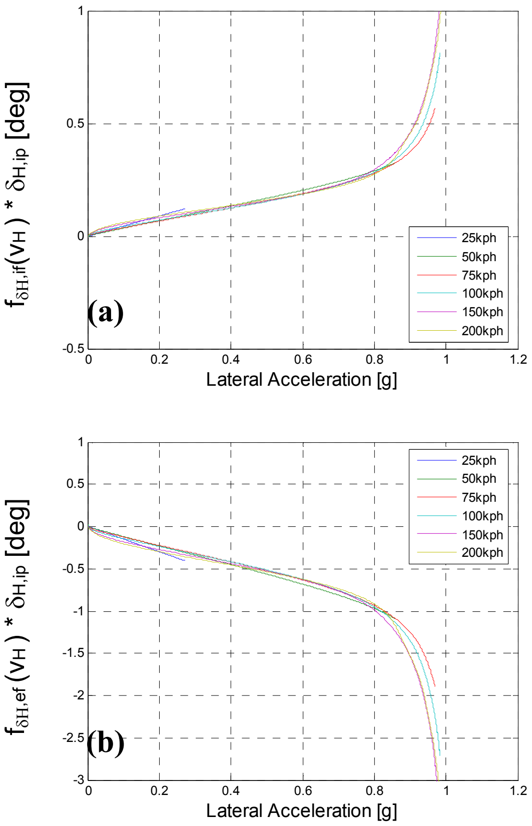

Figure 18 Ramp-steer maneuver at 25, 50, 75, 100, 150 and 200km/h: responses of the third term of the modified camber angle function, $f_{\delta_H,i}(v_H)\cdot\delta_H$, of the (a) internal front and (b) external front tire.

Another important aspect on the signal of the steering wheel angle must be taken into account to introduce an proper variable coefficient. Unlike other signals, the steering wheel never saturates to a certain value, which means it would continuously increase or decrease the camber angle in such an event that the vehicle is turning a tight corner at low speed; furthermore, even more critical situation may be found in a parking maneuver. This is the reason why it is necessary to introduce a kind of filter which allows the signal to saturate. In reality, concerning the range of the steering wheel angle to be used while a vehicle is maintaining a steady-state condition, the range from -180 [deg] up until 180 [deg] would be enough for the vehicle presented in this paper. Therefore, the filter has been designed to allow the signal to converge asymptotically toward the values, -180 and 180 [deg], after passing through -150 or 150 [deg]. Fig.19 (a) shows a filtering map as a function of an input signal, δ_H, and a vehicle velocity, v_H; the filtered signal, $\delta_{H,ft}$, can saturate on certain values depending on a vehicle velocity. By considering both the velocity dependency and the saturation filter, the steering input map has been derived as shown in Fig.19 (b).

The map gives a variable coefficient, $C_{\delta_H}(\delta_H, v_H)$, which can be applied to each one of the wheels with the particular optimized constant coefficients respectively. Likewise, the velocity dependency of the yaw rate $\dot{\psi}$ has been examined.

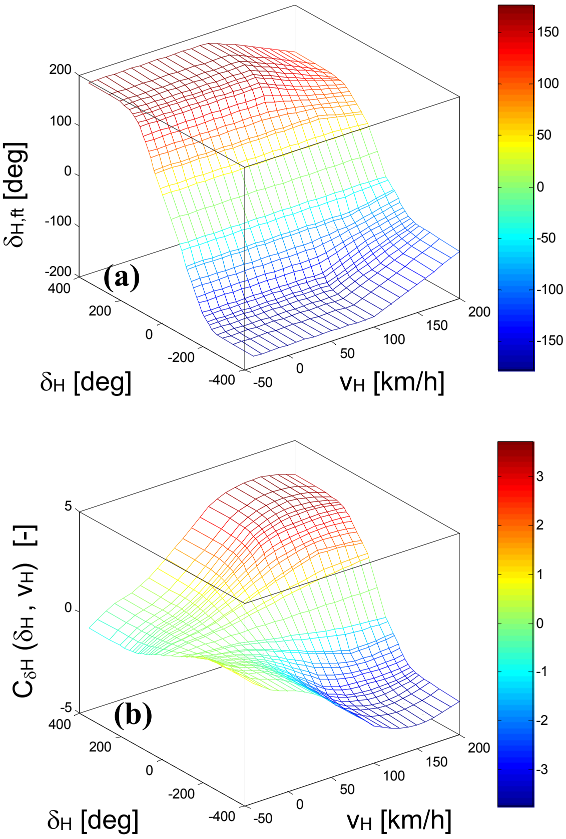

Figure 19 Steering wheel angle map: the (a) saturation and (b) variable coefficient map.

Fig.20 (a) shows a control signal with the optimized constant coefficients. As seen in Fig.20 (b), the signals at each velocities show appreciably similar curves with respect to the reference curve at 100km/h by considering velocity dependencies although nonlinearities are still observed in high lateral acceleration region.

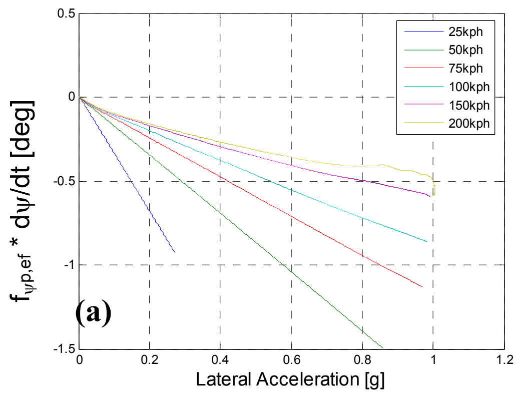

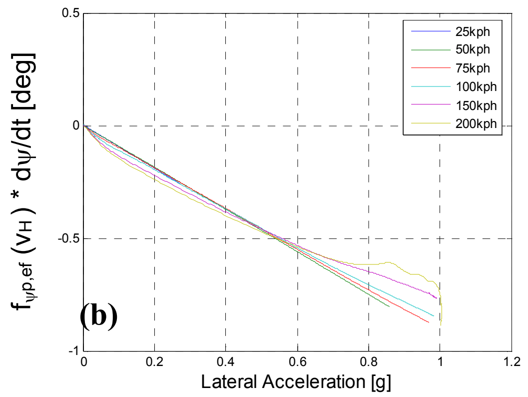

Figure 20 Ramp-steer maneuver at 25, 50, 75, 100, 150 and 200km/h: responses of the second term of the camber angle function (a) $f_{\dot\psi,i}\cdot\dot\psi$ and (b) $f_{\dot\psi,i}(v_H)\cdot\dot\psi$ of the external front tire.

The yaw acceleration, $\ddot\psi$, has been examined as well. Fig.21 (a) and (b) show raw data and modified curves of the yaw acceleration signals at different speed.

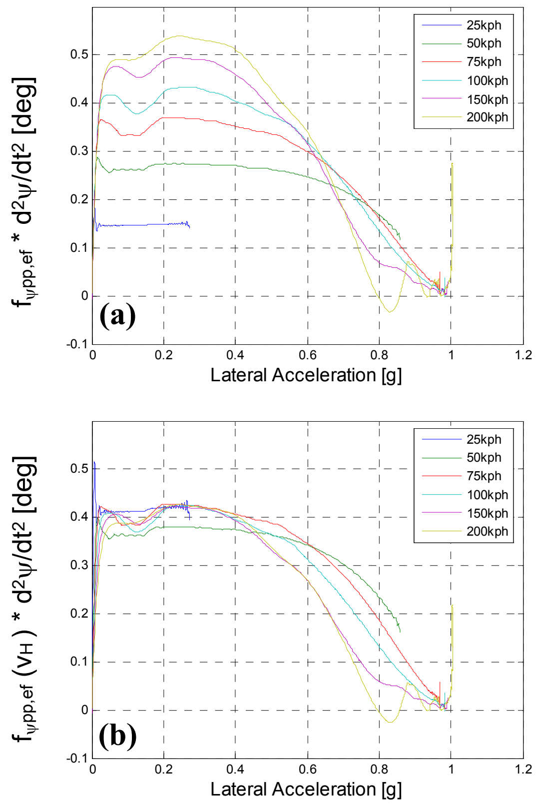

Figure 21 Ramp-steer maneuver at 25, 50, 75, 100, 150 and 200km/h: response of the fourth term of the camber angle function (a) $f_{\ddot\psi,i}\cdot\ddot\psi$ and (b) $f_{\ddot\psi,i}(v_H)\cdot\ddot\psi$ of the external front tire.

It is the noisiest signal of all; however, it is still worth observing because the change of it can be the second fastest signal next to the steering wheel signal, which can quickly tell the change of a vehicle motion to a controller: a yaw rate is the first response of a vehicle with respect to a driver input in terms of a steering wheel.
As a next step, in addition to the vehicle velocity, the lateral acceleration has been taken into account and introduced as one of the axes for variable coefficient maps as shown in Fig.22.

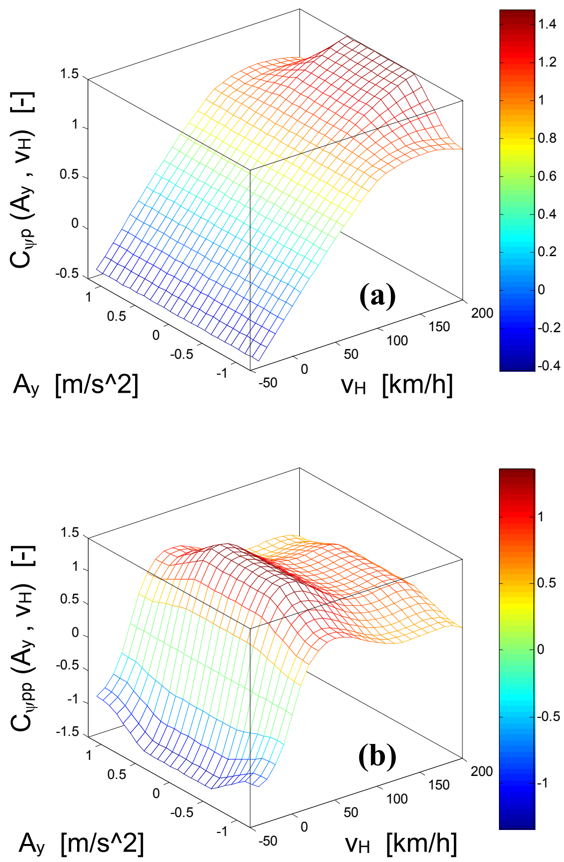

Figure 22 The variable coefficient map for the (a) yaw rate and (b) yaw acceleration

By now, vehicle velocity and lateral acceleration dependencies have been derived to achieve improved steady-state performance in different vehicle conditions and Eq.(10) has been modified as:

$$\gamma_{opt,i} = f_{Ay,i}\cdot A_y + f_{\dot\psi,i}\cdot C_{\dot\psi}\left(A_y, v_H\right)\cdot\dot\psi + f_{\delta_H,i}\cdot C_{\delta_H}\left(\delta_H, v_H\right) + f_{\ddot\psi,i}\cdot C_{\ddot\psi}\left(A_y, v_H\right)\cdot\ddot\psi \qquad (11)$$

where i indicates the same acronyms as Eq.(10). All the maps are implemented on the control logic and appreciably improved performance have been obtained; the details of the simulation results are presented in a following section.

3.3 STEP-STEER MANEUVER

In a step-steer maneuver, vehicle behavior around a limit can be easily reproduced by putting a higher step input of a steering wheel; in addition, both transient and steady state vehicle responses can be evaluated simultaneously. Concerning the vehicle transient motion, which is generated by a step steering input and eventually damped to a steady-state condition, yaw rate and sideslip angle responses are main objects of interest to be improved. The parameter variables of Eq.(10) have been optimized again with different objective functions in a similar procedure under the simulation parameters listed on Table III.

Table III - Step-steer simulation parameters

Total Time	Time step	Velocity	Gear	Step-steer Value	Duration	Start Time
[s]	[s]	[km/h]	[-]	[deg]	[s]	[s]
15	0.005	100	4	85	0.1	5

Fig.23 (a) and (b) show optimization results of yaw rate and sideslip responses in comparison with the passive vehicle.

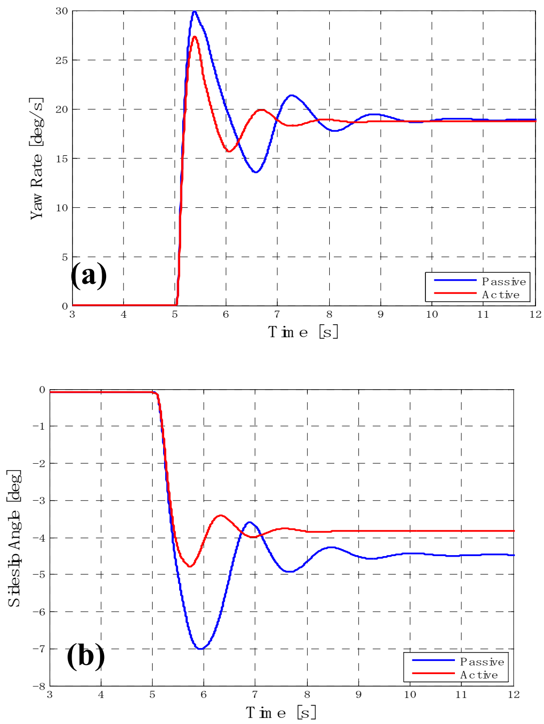

Figure 23 Step-steer maneuver at 100km/h: comparison of the (a) yaw rate and (b) sideslip response of the passive and active vehicle.

The optimization appreciably reduced the objective functions and almost achieved the targets. Fig.24 (a) and (b) show the camber angles with respect to the ground and actuator forces for one of the cylinders assigned by PID controller.

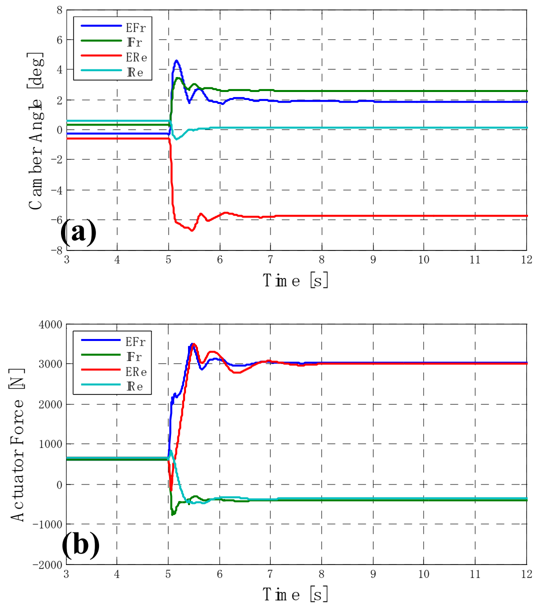

Figure 24 Step-steer maneuver at 50, 75, 100, 150 and 200km/h: the (a) camber angles and (b) actuator forces.

As a result of the optimization, the yaw acceleration signal appeared to be important compared with statedy-state case as seen in Fig.25.

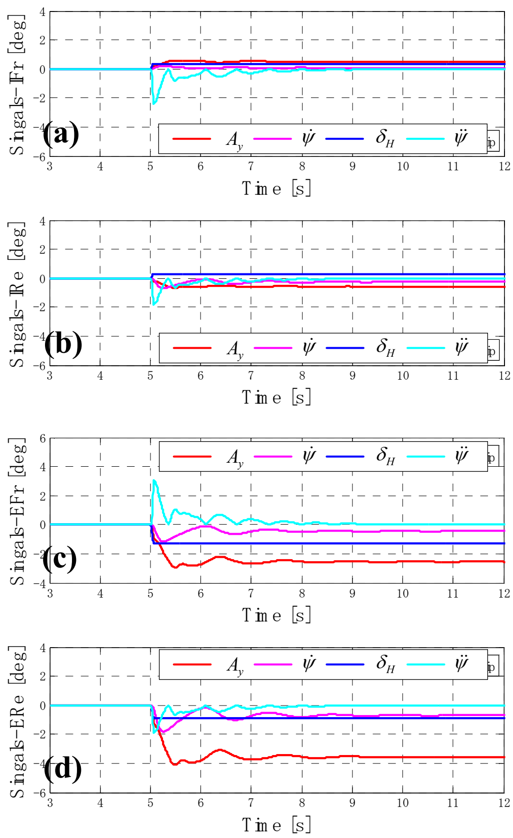

Figure 25 Step-steer maneuver at 100km/h: time history of four terms of camber angle function for the (a) internal front, (b) internal rear, (c) external front, and (d) external rear wheel.

Through the step-steer optimization analysis, new constant coefficients, $g_{x,i}$, instead of $f_{x,i}$ for Eq.(10) have been derived. As it has done for the ramp-steer optimization, velocity dependencies of the new coefficients have been examined in order to obtain the optimized performance in different vehicle speed conditions. In this case, the steering angle input must be varied according to the vehicle speed, because the amount of a step-steer value is defined as 150% of a steering wheel angle value with which the vehicle reaches 85% of a maximum lateral acceleration during a ramp-steer maneuver. Fig.26 indicates the steering wheel angles at 85% of the maximum lateral acceleration in different vehicle speed conditions. Therefore, the steering input values at 150% of the indicated points in Fig.26 are the steering input values for the step-steer maneuvers.

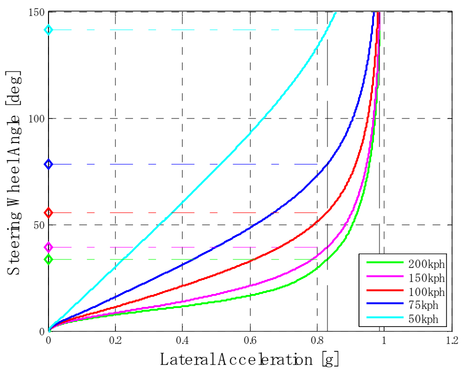

Figure 26 Ramp-steer maneuver at 50, 75, 100, 150 and 200km/h: handling diagram of the passive vehicle.

The details are neglected here; however, the velocity dependency maps, D_x, for the limit handling performance are derived in a similar way as it has done for steady-state case. As an example, $D_{\delta H}$ in Fig.27 shows a similar surface with $C_{\delta H}$.

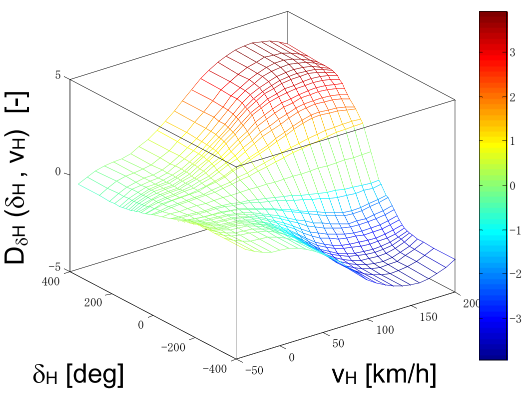

Figure 27 Variable steering wheel angle coefficient map.

The camber angle function can be rewritten as:

$$\gamma_{opt,i} = g_{Ay,i} \cdot A_y + g_{\dot{\psi},i} \cdot D_{\dot{\psi}}\left(A_y, v_H\right) \cdot \dot{\psi} + g_{\delta_H,i} \cdot D_{\delta_H}\left(\delta_H, v_H\right) + g_{\ddot{\psi},i} \cdot D_{\ddot{\psi}}\left(A_y, v_H\right) \cdot \ddot{\psi} \quad (12)$$

where i indicates the same acronyms as Eq.(10). In the current control logic, the transition between Eq.(11) and (12) takes place through a wheel angle rate $\dot{\delta}$ by putting a threshold $\dot{\delta}_{th}$; however, it is appreciable only for the specific maneuvers presented in this paper. In order to identify vehicle conditions in terms of steady-state and transient behavior with respect to vehicle conditions in general, state observers have been under investigation. The identification of the vehicle conditions by the state observers would make it possible to integrate these control logics effectively.

4 SIMULATION RESULTS

Through the optimization analyses, the camber angle controller has been developed and the improved performance in terms of the target maneuvers has been verified.

4.1 RAMP-STEER MANEUVER

Fig.28 shows comparison between the active and passive vehicles. As it can be seen, the vehicle performance optimized at 100km/h is able to be reproduced in different conditions by introducing variable coefficient maps.

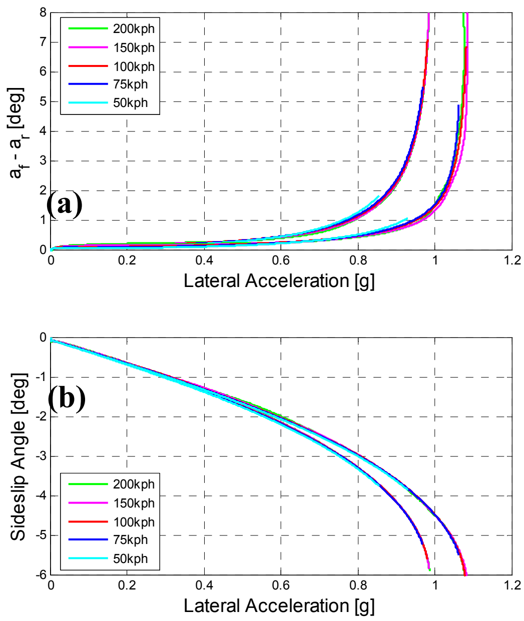

Figure 28 Ramp-steer maneuver at 50, 75, 100, 150 and 200km/h: (a) Handling and (b) Sideslip diagram.

The objective targets achieved by the variable camber suspension are listed in Table IV.

Table IV - Average values of the improvements for steady-state performance.

Ay	US Gradient		SS Gradient	
Max	Linear (0-0.5g)	0.8g	Linear (0-0.5g)	0.8g
+10%	-50%	-73%	-7%	-23%

ISSN 1590-8844
International Journal of Mechanics and Control, Vol. 08, No. 01, 2007

4.2 STEP-STEER MANEUVER

Yaw rate responses in different vehicle speed conditions are shown in Fig.23. Due to the severe definition of a steering input, the passive vehicle can not even maintain the vehicle over 150 km/h and eventually resulted in spinning off; on the other hand, the active vehicle is capable of stabilizing the vehicle in such conditions.

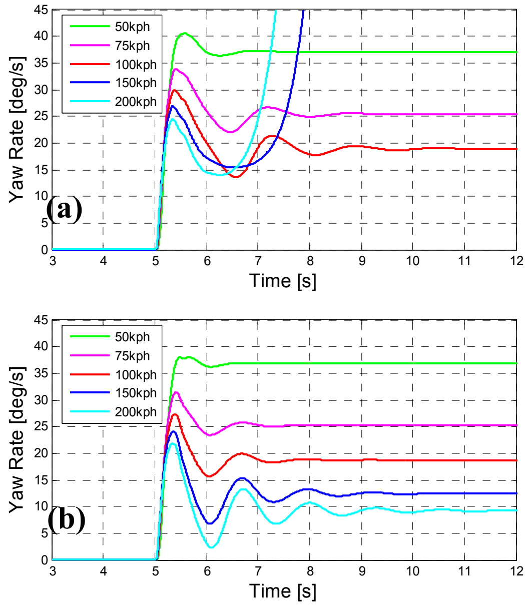

Figure 29 Step-steer maneuver at 50, 75, 100, 150 and 200km/h: the yaw rate responses of the (a) passive and (b) active vehicle.

Fig.30 shows the yaw rate responses normalized by a steady-state yaw rate value, which can be obtained after transient motion is damped, for each one of them.

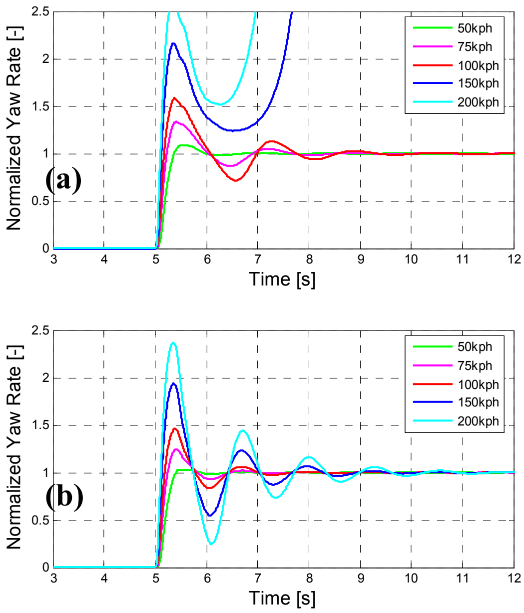

Figure 30 Step-steer maneuver at 50, 75, 100, 150 and 200km/h: the normalized yaw rate responses of the (a) passive and (b) active vehicle.

Fig.30 shows how effectively the active suspension damps the vehicle yaw motion compared with the passive case. Fig.31 shows vehicle sideslip angle responses in different speed conditions; the considerable reduction of the sideslip angle peak can be clearly seen.

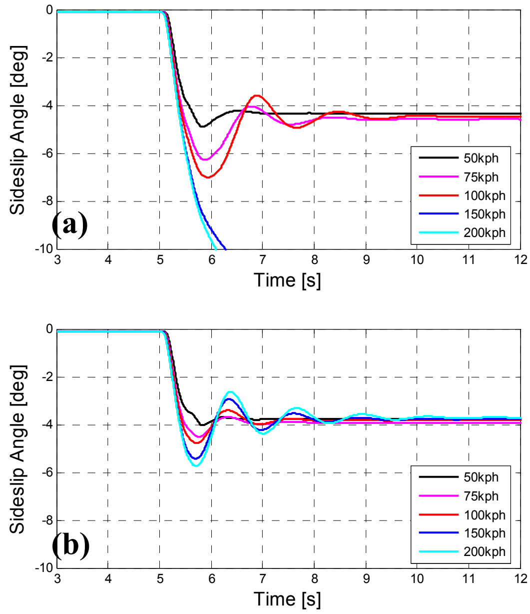

Figure 31 Step-steer maneuver at 50, 75, 100, 150 and 200km/h: the sideslip angle responses of the (a) passive and (b) active vehicle.

The vehicle trajectory paths shown in Fig.32 certify the fact that the vehicles are on a quite close path with different vehicle motions. Table V shows the objective targets achieved by the variable camber suspension.

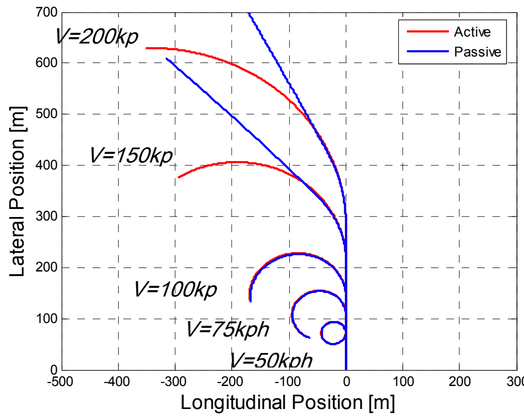

Figure 32 Step-steer maneuver at 50, 75, 100, 150 and 200km/h: comparison of the vehicle trajectory paths between the passive and active vehicle.

Table V - Average values of objective targets for limit performance

$\dot{\psi}$ P-P Value	$\dot{\psi}$ Damping	β Peak Value
-39%	-35%	-26%

Lastly, the closed up figure of the trajectory path at 150km/h is shown in Fig.33. The figure shows that the active vehicle can maintain stable condition while the passive one spins off with the same steering input.

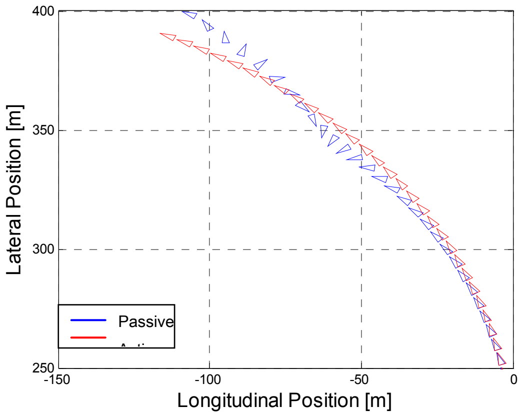

Figure 33 Step-steer maneuver at 150km/h: comparison of the vehicle trajectory path between the passive and active vehicle.

4.3 SWEPT-STEER MANEUVER

In order to evaluate transient performance of the active vehicle, frequency response analyses by a swept-steer maneuver have been performed with a maximum steering angle of 20°, varying the frequency input from 0.2 to 4 Hz with a rate of 0.2 Hz/s in different speed conditions as listed in Table VI. In this maneuver, the tire/vehicle system acts as a transfer function and is used to pass from a time domain to a frequency domain in order to evaluate frequency responses.

Table VI - Swept-steer simulation parameters.

Total Time	Time step	Velocity	Swept-steer Value	Frequency Rate	Start Time
[s]	[s]	[km/h]	[deg]	[Hz]	[s]
26	0.005	50,75,100,150	-20/20	0.2	5

The camber angle function Eq.(11) has applied to this maneuver; Fig.34 shows frequency responses of yaw rate and lateral acceleration. The higher the vehicle speed is, the higher static gain the active vehicle acquires; both vehicles show similar behavior in a low speed condition but an average 40% reduction of a peak gain ratio with respect to a static gain has been achieved at the vehicle speed over 75km/h conditions.

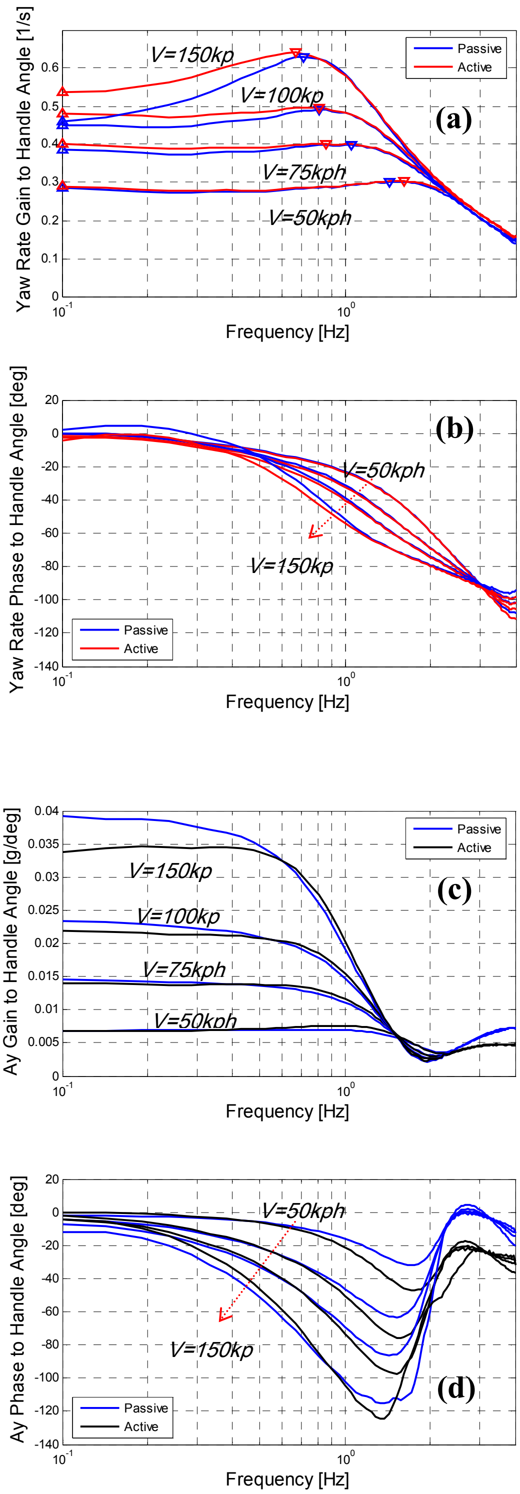

Figure 34 Swept-steer maneuver at 50, 75, 100 and 150km/h: frequency responses of the (a) yaw rate gain, (b) yaw rate phase, (c) lateral acceleration gain, and (d) lateral acceleration phase to the handle angle.

CONCLUSIONS

Through the optimization analyses, the camber angle controller has been developed to make the most of tire performance by means of the variable camber suspension. The results presented here show appreciable improvements in terms of steady-state, limit, and transient performance. Since the objective targets are clearly given to specific open loop maneuvers in order to investigate the basic behavior of the active and passive vehicle, the control strategies developed in this paper are dedicated to these maneuvers; therefore, closed loop campaigns represented by a lane change maneuver etc, are going to be examined to make these camber angle functions work toward more general driving conditions. At this point, state observers have been under investigation in order to identify steady-state and transient conditions so that the presented control strategies would be effectively integrated and applied in general driving conditions. In addition, the actuator forces necessary to realize the variable camber have been investigated as well. Therefore, a real actuator which meets the demands must be looked for and found in order to take a realistic actuator dynamics into account as a next step.

NOMENCLATURE

X-Y-Z	Global Coordinate System fixed to a Ground
ψ	Vehicle Yaw Angle
θ	Vehicle Pitch Angle
ρ	Vehicle Roll Angle
z_{ui}	i-th Displacement of Unsprung Mass
θ_{ui}	i-th Rotational Angle of Wheel
γ_{pi}	i-th Tire Passive Camber Angle
γ_{ai}	i-th Tire Active Camber Angle
σ_{κ}	Longitudinal Relaxation Length
σ_{α}	Lateral Relaxation Length
κ	Longitudinal Slip
α	Lateral Slip
α_f	Front Tire Slip Angle
α_r	Rear Tire Slip Angle
δ_H	Steering Wheel Angle
$\gamma_{opt,i}$	i-th Optimum Inclination Angle
$f_{Ay,i}$	i-th Constant Coefficient for A_y signal
$f_{\psi p,i}$	i-th Constant Coefficient for ψ_p signal
$f_{\delta H,i}$	i-th Constant Coefficient for δ_H signal
$f_{\psi pp,i}$	i-th Constant Coefficient for ψ_{pp} signal
$C_{\psi p}$	Variable Coefficient for ψ_p signal
$C_{\delta H}$	Variable Coefficient for δ_H signal
$C_{\psi pp}$	Variable Coefficient for ψ_{pp} signal
$D_{\psi p}$	Variable Coefficient for ψ_p signal
$D_{\delta H}$	Variable Coefficient for δ_H signal
$D_{\psi pp}$	Variable Coefficient for ψ_{pp} signal
γ	Tire Camber Angle with respect to Ground
F_z	Normal Wheel Load
F_{z0}	Tire Nominal Load
R_0	Unloaded Tire Radius
Pt…	MF Coefficients for Transient Response
Pk…	MF Coefficients for Pure Slip Coefficients

REFERENCES

[1] Ammon D., *Vehicle Dynamics Analysis Tasks and Related Tire Simulation Challenges*, International Journal of Style Guides, VOL.24, N.4, Month 2004, pp. 2346-2498.

[2] Schiehlen W., Multibody system dynamics: Roots and perspectives. *Multibody System Dynamics*, 1, pp. 149-188, 1997.

[3] Kuwayama I., Baldoni F. and Cheli F., *A Full Vehicle Model for the Development of a Variable Camber Suspension*, to be published.

[4] Pacejka H.B., 2002, Tyre and Vehcle Dynamics, Butterworth and Heinemann Editions.

[5] Cheli F., Pedrinelli M. and Zorzutti A., 2005, *Modellazione Integrata della Dinamica dell'Autoveicolo e della Powertrain*, Proceedings of XVII AMETA Congress, 11-15 September, Firenze, Italy.

[6] Kiencke U. and Nielsen L., 2000, *Automotive Control Systems: For Engine, Driveline, and Vehicle*, Springer.

[7] Rajamani R., 2006, *Vehicle Dynamics and Control*, Springer.

[8] Milliken W.F. and Milliken D.L., 1995, Race Car Vehicle Dynamics, Society of Automotive Engineers, Inc.

[9] Gillespie T.D., 1992, Fundamentals of vehicle dynamics, Society of Automotive Engineers, Inc.

ISSN 1590-8844
International Journal of Mechanics and Control, Vol. 08, No. 01, 2007

VISION SYSTEM FOR INDUSTRIAL ROBOTS PATH PLANNING

V. Niola, C. Rossi, S. Savino

Department of Mechanical Engineering for Energetics
University of Naples "Federico II"

ABSTRACT

In this paper the early results on the possibility to use a video system for the robot's trajectories planning is presented. By means of this application it is possible to plan the trajectories by a PC monitor, just clicking with the mouse on the monitor.
In order to obtain a three dimensional vision a couple of cameras has been used.
A software was developed that by means of each couple of frames make possible to select a desired point in the work space, obtaining three cartesian coordinates. These last are given to the control system and recorded by this last. Finally the control system will move the robot in a work cycle that is described by means of the points selected and recorded as described above.
Tests have been carried on with a robot prototype that was designed and built at our Laboratory and showed a very good behaviour of the system.

Keywords: Vision System, Path Planning, Industrial Robots

1 INTRODUCTION

Industrial robots are a part of a production system and are used for a large number of application. Industrial application are referred to technological fields (assembly or dismounting, cut or stock removal; electrochemical processes; abrasive trials; cold or warm moulding; design with CAD techniques; metrology), or about several processes (control of the row material; workmanship of the component; assemblage; packing or storages; controls of quality; maintenance).
The main advantages of this technique are:
1) elimination of the human errors, particularly in the case of repetitive or monotonous operations;
2) possibility to vary the production acting on the power of the automatic system (the automatic machines can operate to high rhythms day and night every day of the year);
3) greater informative control through the acquisition of historical data; these data can be used for successive elaborations, for the analysis of the failures and to have statistics in real time;
4) quality control founded on objective parameters in order to avoid dispute, and loss of image.

Contact author: Cesare Rossi
University of Naples "Federico II"
Department of Mechanical Engineering for Energetics
Via Claudio, 21 – 80125 Napoli – Italy
E-mail cesare.rossi@unina.it

In any case a work cycle of a robot will be made by a number of points and sub-trajectories that can be planned in several ways.
The "Artificial Vision" permits industrial automation and system vision able to act in the production activities without humane presence and can be usefully connected with robotic systems; in fact the vision for a robot system can significantly increase the robot capability to interact with the environment and also can evaluate, analyze and manage the robot's movements.
In this paper the early results on the possibility to use a video system for the robot's trajectories planning is presented. By means of this application it is possible to plan the trajectories by a PC monitor, just clicking with the mouse on the monitor.

2 THE PATH PLANNING

A path planning algorithm, using as inputs: path definition and constraints due to the path and due to the robot's structure, will compute the trajectories in the joint space as arrays of positions and, also, velocities and accelerations of the joint themselves.
At the Robot Mechanics Laboratory of the Department of Mechanical Engineering for Energetics, has been developed a complete procedure that permits to give to a robot arm all the parameters to describe an assigned path; this by means of a vision system. The procedure gives to the operator the possibility to fix start and end points of a working cycle, the

intermediate points and the obstacles, by means of a couple of images on the monitor of a PC.
This procedure starts from a software, developed at the same Laboratory, that permits to recognize a point of a three dimensional work space, starting from its two dimensional frame (image plane). This needs, obviously, at least a couple of images, taken from two different points of view (stereoscopic vision).

2.1 THE VISION SYSTEM
A vision system essentially consists in a frame grabber, a (television) camera and an host computer. Each point of the observed scene has a corresponding point on the image; the linkage between the "scene points" and the "image points" is a merely geometric transform, as schematically shown in figure 1

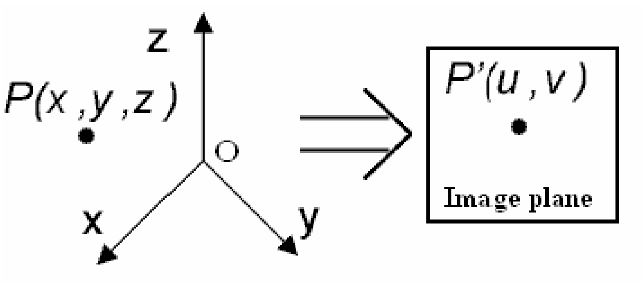

Figure 1 Geometric transform.

A (tele)camera model is necessary; this means to find the geometrical relations that describe the transform mentioned above, tacking onto account all the involved parameters. These last are intrinsic parameters (optics and camera sensors) and extrinsic parameters that essentially depend on the position of the camera reference frame respect to an external frame.
The simplest (tele)camera mathematical model is the pin-hole that is schematically reported in figure 2.

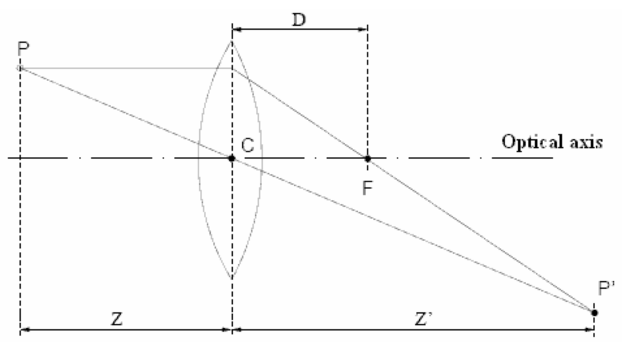

Figure 2 Pin hole model-

If f (focal length), is the distance of the hole (or center of projection) O from the image plane, then by means of the triangles similarity, it is possible to obtain:

$$X' = -f \cdot \frac{X}{Z} \qquad Y' = -f \cdot \frac{Y}{Z} \qquad Z' = -f \qquad (1\text{-}3)$$

If the coordinates of a point P(X,Y,Z) in the scene and the focal length are known, it is possible to asses the coordinates of a point P'(X',Y',Z') that is the "image" of P on the image plane.
Obviously the opposite is not possible: from a point on the image plane it isn't possible to obtain its corresponding coordinates in the space. This last aspect becomes possible only if a couple of images of the same scene are available; in this case, in fact, it is possible to obtain a stereoscopic vision. This last can reconstruct a three-dimensional object by a number n ($n \geq 2$) of different images. In our case a couple of tele-cameras was used.

2.2 THE PERSPECTIVE TRANSFORMATION
If $\{O,x,y,z\}$ and $\{\Omega,\xi,\eta,\zeta\}$ are 2 arbitrarily disposed reference systems, and P is a point whose Cartesian coordinates in reference system $\{O,x,y,z\}$are expressed by means vector $\{w\}$, then is possible to write Cartesian coordinates in reference system $\{\Omega,\xi,\eta,\zeta\}$ by means following vector:

$$\{w_c\} = [R] \cdot \{w\} + \{t\} \qquad (4)$$

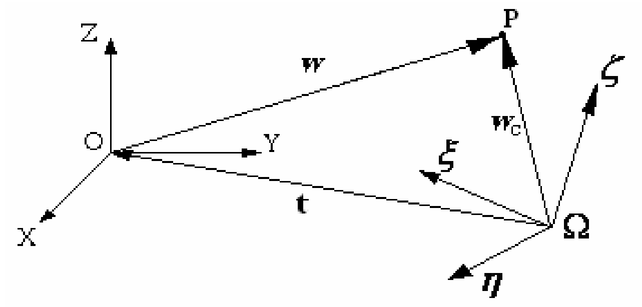

Figure 3 Frames.

where
$\{w\}$ is expressed in the reference $\{O,x,y,z\}$;
$\{w_c\}$ is expressed in the reference $\{\Omega,\xi,\eta,\zeta\}$;
$\{t\}$ is the vector from the point Ω to the point O, and is expressed in the reference $\{\Omega,\xi,\eta,\zeta\}$;
$[R]$ is the rotation matrix between two reference systems .

The columns of the matrix $[R]$ represent the members of versors $\hat{x}, \hat{y}, \hat{z}$ in the reference $\{\Omega,\xi,\eta,\zeta\}$; mutual, the lines of such matrix they are the members of versors $\hat{\xi}, \hat{\eta}, \hat{\varsigma}$ in the reference $\{O,x,y,z\}$.

$$[R] = \begin{bmatrix} \xi_x & \xi_y & \xi_z \\ \eta_x & \eta_y & \eta_z \\ \zeta_x & \zeta_y & \zeta_z \end{bmatrix} \qquad (5)$$

It is possible to write (4) in homogenous coordinates:

$$\{\widetilde{w}_c\}=\begin{Bmatrix} w_\xi \\ w_\eta \\ w_\zeta \\ 1 \end{Bmatrix}=[T]\cdot\{\widetilde{w}\}=\begin{bmatrix} \xi_x & \xi_y & \xi_z & t_\xi \\ \eta_x & \eta_y & \eta_z & t_\eta \\ \zeta_x & \zeta_y & \zeta_z & t_\zeta \\ 0 & 0 & 0 & 1 \end{bmatrix}\cdot\begin{Bmatrix} w_x \\ w_y \\ w_z \\ 1 \end{Bmatrix} \tag{6}$$

The matrix [T] is a homogenous transformation matrix.
The first three elements of the fourth row, constitute the matrix of perspective transformation, that it concurs to project points, geometric places, on a plan, considering their guideline and their distance from this plane.
$\hat{n}$ is a perpendicular versor to the plan R in the image reference: it coincides with one of versors of reference system, like it is shown in figure 4.

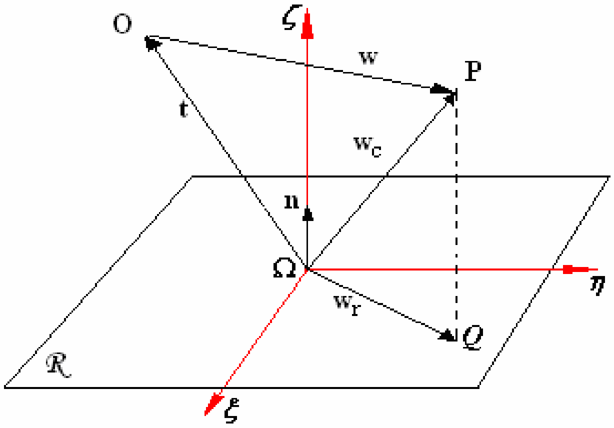

Figure 4

It is easy to see that the distance of the P point from the plane R is characterized from the segment PQ, whose value can be obtained like scalar product between $\hat{n}$ and w_c:

$$\begin{aligned} d &= \{\hat{n}\}^T\cdot\{w_c\}=\{\hat{n}\}^T\cdot([R]\cdot\{w\}+\{t\})= \\ &=([R]^{-1}\cdot\{\hat{n}\})^T\cdot\{w\}+\{\hat{n}\}^T\cdot\{t\} \end{aligned} \tag{7}$$

introducing homogenous coordinates the (7) can be written:

$$d=\begin{Bmatrix} [R]^{-1}\cdot\{\hat{n}\} \\ \{\hat{n}\}^T\cdot\{t\} \end{Bmatrix}^T\{\widetilde{w}\}=\{\widetilde{N}\}^T\cdot\{\widetilde{w}\} \tag{8}$$

where the product $[R]^{-1}\cdot\{\hat{n}\}$, characterizes the first three members of the vector $\{\widetilde{N}\}$, and $\{\hat{n}\}^T\cdot\{t\}$ represents the fourth component:

$$\{\widetilde{N}\}=\begin{Bmatrix} N_x \\ N_y \\ N_z \\ t_n \end{Bmatrix}=\begin{Bmatrix} \xi_x\cdot n_\xi+\eta_x\cdot n_\eta+\zeta_x\cdot n_\zeta \\ \xi_y\cdot n_\xi+\eta_y\cdot n_\eta+\zeta_y\cdot n_\zeta \\ \xi_z\cdot n_\xi+\eta_z\cdot n_\eta+\zeta_z\cdot n_\zeta \\ t_\xi\cdot n_\xi+t_\eta\cdot n_\eta+t_\zeta\cdot n_\zeta \end{Bmatrix} \tag{9}$$

The first three elements of N correspond to the members of orthogonal versor to the projection plan, written in starting reference system, while the fourth element represents the distance between two reference origin, measured along the orthogonal direction.
Starting from vector $\{w_c\}$, that characterizes the coordinates of the point P in the camera reference, it is possible to determine the vector $\{w_r\}$. It characterizes the coordinates of the point Q in the reference system $\{\Omega,\xi,\eta,\zeta\}$, and, therefore, it is always a vector of image plan R. It is possible to express such vector like product of an opportune matrix [S] and the vector $\{w_c\}$:

$$\{\widetilde{w}_r\}=\begin{Bmatrix} w_\xi \\ w_\eta \\ w_\zeta \\ 1 \end{Bmatrix}=[S]\cdot\{\widetilde{w}_c\}=$$
$$=\begin{bmatrix} n_\eta+n_\zeta & 0 & 0 & 0 \\ 0 & n_\xi+n_\zeta & 0 & 0 \\ 0 & 0 & n_\xi+n_\eta & 0 \\ 0 & 0 & 0 & 1 \end{bmatrix}\cdot\begin{Bmatrix} w_\xi \\ w_\eta \\ w_\zeta \\ 1 \end{Bmatrix} \tag{10}$$

Obviously, one of the members of the vector $\{w_r\}$ will be null, since it is planar vector : if versor $\hat{n}$ coincides with the axis ζ (figure 4), then $w_\zeta=0$. This means that the matrix S will have always one null line.
Replacing in (2.10) $\{w_c\}$ expression:

$$\{\widetilde{w}_r\}=[S]\cdot\{\widetilde{w}_c\}=[S]\cdot[T]\cdot\{\widetilde{w}\} \tag{11}$$

An object, when it is represented in perspective, appears more or less "large" according to its distance from the observation point.
It is possible to define a perspective projection vector $\{\widetilde{p}\}$, that it is obtained starting from the vector $\{w_r\}$, scaling it of the distance d from projection plan:

$$\{\widetilde{p}\}=\begin{Bmatrix} w_\xi \\ w_\eta \\ w_\zeta \\ d \end{Bmatrix}=\begin{Bmatrix} (n_\eta+n_\zeta)\cdot w_\xi \\ (n_\xi+n_\zeta)\cdot w_\eta \\ (n_\xi+n_\eta)\cdot w_\zeta \\ \{\widetilde{N}\}^T\cdot\{\widetilde{w}\} \end{Bmatrix}=[T_P]\cdot\{\widetilde{w}\} \tag{12}$$

The matrix $[T_p]$ is the perspective transformation matrix; by means of this matrix, it is possible to determine the coordinates in the image plan, of a {O,x,y,z} reference system point.
It is interesting to consider this last matrix as follows:

$$[T_P] = [S]\cdot[T_{OL}] = \begin{bmatrix} (n_\eta + n_\zeta) & 0 & 0 & 0 \\ 0 & (n_\xi + n_\zeta) & 0 & 0 \\ 0 & 0 & (n_\xi + n_\eta) & 0 \\ 0 & 0 & 0 & 1 \end{bmatrix} \cdot \begin{bmatrix} \xi_x & \xi_y & \xi_z & t_\xi \\ \eta_x & \eta_y & \eta_z & t_\eta \\ \zeta_x & \zeta_y & \zeta_z & t_\zeta \\ N_x & N_y & N_z & t_n \end{bmatrix} \tag{13}$$

Matrix $[T_{OL}]$ is a transformation matrix, that allows to realize a 3D scaling

If the versor $\hat{n}$, that is normal to the image plane, coincides with the ζ axis, matrix $[T_p]$ becomes:

$$[T_P] = \begin{bmatrix} \xi_x & \xi_y & \xi_z & t_\xi \\ \eta_x & \eta_y & \eta_z & t_\eta \\ 0 & 0 & 0 & 0 \\ N_x & N_y & N_z & t_n \end{bmatrix} \tag{14}$$

Thus the perspective projection vector $\{\tilde{p}\}$ will be given from:

$$\{\tilde{p}\} = \{w_\xi, w_\eta, 0, d\}^T$$

Evidently in this expression there is a loss of information that depends on which plane has been chosen as projection plane. In fact, if vector $\hat{n}$ coincides with one of the axes of the frame $\{\Omega,\xi,\eta,\zeta\}$, two of its components are zero. This means a reduction of the matrix [S] rank, so, indirectly, [Tp] will be non invertible and the computing of the point P Cartesian coordinates from those in the image plane will be impossible.

Matrix [S] represents the fact that in a perspective representation the third dimension is not valuable so that it is impossible to recognize an object from a two dimensional image [1,5,6].

2.3 THE CAMERA MODEL

A camera is a device that "captures" a portion of space in a plane image.

A mathematical model of the camera must permit to compute the coordinates of a point in the image plane from those spatial of the same point.

The simplest camera model is the pin-hole.

Consider a point $P \equiv \{w_\xi, w_\eta, w_\zeta\}^T$ and it's projection P' $\equiv \{u,v\}^T$ on R through the plane F (see fig.5)

As already described, it is possible to write simple perspective projection equations:

$$\begin{cases} u = f\cdot\dfrac{w_\xi}{w_\zeta} \\ v = f\cdot\dfrac{w_\eta}{w_\zeta} \end{cases} \tag{15}$$

If we consider the point P position vector in a frame having a plane parallel to the image plane, the previous equations describe the transform of this vector through a thin lens.

The transform consists in a d/f factor scaling, where d is the distance between the point p and the camera plane and, in the simple case of $\hat{n} \equiv \zeta$, is $d = w_\zeta$.

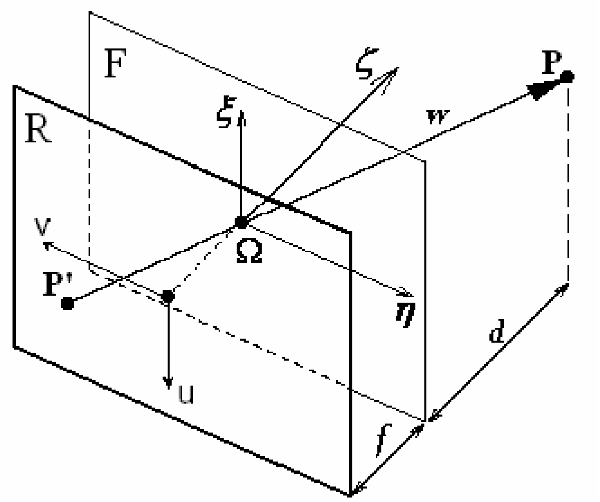

Figure 5

If, for the sake of simplicity, that versor $\hat{n}$ coincides with ζ axis, we obtain:

$$\{\tilde{p}\} = \begin{Bmatrix} w_\xi \\ w_\eta \\ 0 \\ d \end{Bmatrix} = [T_P]\cdot\{\tilde{w}\} = \begin{bmatrix} \xi_x & \xi_y & \xi_z & t_\xi \\ \eta_x & \eta_y & \eta_z & t_\eta \\ 0 & 0 & 0 & 0 \\ N_x & N_y & N_z & t_n \end{bmatrix} \cdot \begin{Bmatrix} w_x \\ w_y \\ w_z \\ 1 \end{Bmatrix} \tag{16}$$

To take onto account the transform operated from the thin lens, it is possible to define a new matrix that will be indicated as focal matrix [F]:

$$\begin{Bmatrix} u \\ v \\ 0 \\ d/f \end{Bmatrix} = [F]\cdot\{\tilde{p}\} = \tag{17}$$
$$= \begin{bmatrix} 1 & 0 & 0 & 0 \\ 0 & 1 & 0 & 0 \\ 0 & 0 & 1 & 0 \\ 0 & 0 & 0 & 1/f \end{bmatrix} \cdot \begin{bmatrix} \xi_x & \xi_y & \xi_z & t_\xi \\ \eta_x & \eta_y & \eta_z & t_\eta \\ 0 & 0 & 0 & 0 \\ N_x & N_y & N_z & t_n \end{bmatrix} \cdot \begin{Bmatrix} w_x \\ w_y \\ w_z \\ 1 \end{Bmatrix}$$

The (17) permits to compute the coordinates (u, v) of a image point P' starting from those of a space point P.
It has to be considered that:
1. The camera optical centre doesn't coincide with the CCD physical centre, having, instead, coordinates (u_0 , v_0).
2. The coordinates of a point in the camera reference frame are measured in pixel, so, a scale factor must be considered.
3. The pixel is not a square, so, two different scale factors must be considered: one along u (δ_u) and another along v (δ_v).
4. Because of dephasings in the screen line scanning the axes of the image frame are not orthogonal but the angle beween them is $\vartheta \neq \pi/2$.
The first three points are taken onto account by introducing in the 15 the optical centre translation and the re-scaling of the axes u and v independently one from the other:

$$\begin{cases} u = \dfrac{1}{\delta_u}\cdot f \cdot \dfrac{w_\xi}{w_\zeta} + u_0 \\ v = \dfrac{1}{\delta_v}\cdot f \cdot \dfrac{w_\eta}{w_\zeta} + v_0 \end{cases} \tag{18}$$

where:

(u_0 ,v_0) are the coordinates of the main point;
(δ_u δ_v) are the real pixel dimensions along the directions u e v; the physical dimensions of δ are in pixel $\cdot m^{-1}$.

The proposed model, if versor $\hat{n}$ coincides with ζ axes, becomes:

$$\begin{Bmatrix} u \\ v \\ 0 \\ 1 \end{Bmatrix} = \frac{1}{d}\cdot \begin{bmatrix} f/\delta_u & 0 & 0 & u_0 \\ 0 & f/\delta_v & 0 & v_0 \\ 0 & 0 & 1 & 0 \\ 0 & 0 & 0 & 1 \end{bmatrix} \cdot \begin{Bmatrix} w_\xi \\ w_\eta \\ 0 \\ d \end{Bmatrix} = \tag{19}$$
$$= [K]\cdot\{\tilde{p}\}$$

Matrix [K] can be defined as intrinsic camera parameters matrix, because its elements depends only on the focal distance and on the camera sensor characteristics.
A more general model must consider that the axes of the image frame are not orthogonal but the angle between them is $\vartheta \neq \pi/2$. Thus, matrix K, in a general form is:

$$[K] = \begin{bmatrix} f/\delta_u & (f/\delta_u)\cdot\cot\vartheta & 0 & u_0 \\ 0 & f/(\delta_v \cdot \sin\vartheta) & 0 & v_0 \\ 0 & 0 & 1 & 0 \\ 0 & 0 & 0 & 1 \end{bmatrix} \tag{20}$$

Hence, the "pin-hole" camera model can be described, in general, by the following equation:

$$\begin{Bmatrix} u \\ v \\ w \\ 1 \end{Bmatrix} = \frac{1}{d}\cdot[K]\cdot[S]\cdot[T_{OL}]\cdot\{\tilde{w}\} \tag{21}$$

written for a generic projection plane.
If the versor $\hat{n}$ coincides with ζ axis, the model becomes:

$$\begin{Bmatrix} u \\ v \\ 0 \\ 1 \end{Bmatrix} = \frac{1}{d}\cdot \begin{bmatrix} f/\delta_u & 0 & 0 & u_0 \\ 0 & f/\delta_v & 0 & v_0 \\ 0 & 0 & 1 & 0 \\ 0 & 0 & 0 & 1 \end{bmatrix} \cdot \begin{bmatrix} 1 & 0 & 0 & 0 \\ 0 & 1 & 0 & 0 \\ 0 & 0 & 0 & 0 \\ 0 & 0 & 0 & 1 \end{bmatrix} \cdot$$
$$\cdot \begin{bmatrix} \xi_x & \xi_y & \xi_z & t_\xi \\ \eta_x & \eta_y & \eta_z & t_\eta \\ \zeta_x & \zeta_y & \zeta_z & t_\zeta \\ N_x & N_y & N_z & t_n \end{bmatrix} \cdot \begin{Bmatrix} w_x \\ w_y \\ w_z \\ 1 \end{Bmatrix} \tag{22}$$

By a further simplifying we have:

$$\begin{Bmatrix} u \\ v \\ 0 \\ 1 \end{Bmatrix} = \frac{1}{d}\cdot \begin{bmatrix} f/\delta_u & 0 & 0 & u_0 \\ 0 & f/\delta_v & 0 & v_0 \\ 0 & 0 & 1 & 0 \\ 0 & 0 & 0 & 1 \end{bmatrix} \cdot \begin{bmatrix} \xi_x & \xi_y & \xi_z & t_\xi \\ \eta_x & \eta_y & \eta_z & t_\eta \\ 0 & 0 & 0 & 0 \\ N_x & N_y & N_z & t_n \end{bmatrix} \cdot \begin{Bmatrix} w_x \\ w_y \\ w_z \\ 1 \end{Bmatrix} =$$
$$= \frac{1}{d}\cdot[K]\cdot[T_P]\cdot\{\tilde{w}\} \tag{23}$$

This last equation can be also written as follows:

$$\begin{Bmatrix} u \\ v \\ 0 \\ 1 \end{Bmatrix} = [M]\cdot\{\tilde{w}\} \Leftrightarrow \{\tilde{\phi}\} = [M]\cdot\{\tilde{w}\} \tag{24}$$

Where $\{\tilde{\phi}\}$ is the vector $\{u,v,0,1\}^T$, and [M] is the following matrix:

$$[M] = \frac{1}{d}\cdot[K]\cdot[T_P] = \frac{1}{d}\cdot[K]\cdot[S]\cdot[T_{OL}]$$

ISSN 1590-8844
International Journal of Mechanics and Control, Vol. 08, No. 01, 2007

The terms of this last equation are:
$[K]$ is the intrinsic camera parameters matrix and contains information on optics and on the sensors of the camera

$$[K]=\begin{bmatrix} f/\delta_u & 0 & 0 & u_0 \\ 0 & f/\delta_v & 0 & v_0 \\ 0 & 0 & 1 & 0 \\ 0 & 0 & 0 & 1 \end{bmatrix}=\begin{bmatrix} f_u & 0 & 0 & u_0 \\ 0 & f_v & 0 & v_0 \\ 0 & 0 & 1 & 0 \\ 0 & 0 & 0 & 1 \end{bmatrix}$$

$[T_{OL}]$ is the extrinsic camera parameters matrix and contains information on its spatial position.
The elements of matrix $[S]$ are the components of the versor orthogonal to the retina plane; they are not considered as extrinsic parameters because their amount depend only on the adopted conventions.
The focal length can be expressed as a function of the pixel's dimensions and is represented by vector:

$$\{f\}=\{f_u \quad f_v\}^T=[\{f/\delta_u f/\delta_v\}]^T$$

In this way it is possible to use a lower number of parameters, by introducing just the two components of vector $\{f\}$, instead of the 3 parameters f, δ_u, δ_v.
Finally: equation (24) represents the correspondence between the coordinates of a point in the image plane and those of the same point in the work space.
The situation is more complex if it is necessary to recognise the position (w) of a point starting to its camera image (u, v). In this case the expression (24) becomes a system of 2 equation with 3 unknowns, so it is not absolutely solvable.
This obstacle can be exceeded by means of a vision system with at least two cameras.

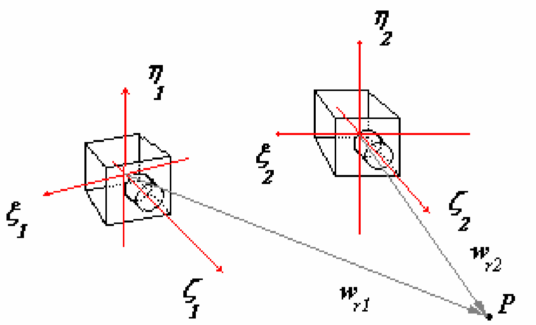

Figure 6

Equation (24) must be written for both the cameras:

$$\begin{aligned}&[M_1]\{\tilde{w}\}_o=\{\tilde{\phi}_1\}\\&[M_2]\{\tilde{w}\}_o=\{\tilde{\phi}_2\}\end{aligned}\qquad(25)$$

As martix [M] is given by the product of the factors: $\frac{1}{d}\cdot[K]\cdot[T_P]$, its third row is null; hence it is not invertible.
Our aim is to find the vector $\{\tilde{w}\}_0$, that is to say: to find the spatial coordinates of a point from the coordinates $\{\tilde{\phi}\}$ in the image plane. As equation 4.5 is non invertible, the problem has to be solved as follows: matrix [M] can be written in this way:

$$[M]=\begin{bmatrix} \{m_1\}^T & m_{14} \\ \{m_2\}^T & m_{24} \\ \{m_3\}^T & m_{34} \\ \{m_4\}^T & m_{44} \end{bmatrix}\qquad(26)$$

This last, if is $\{n\}_r=\{\zeta\}_r$ becomes:

$$[M]=\begin{bmatrix} \{m_1\}^T & m_{14} \\ \{m_2\}^T & m_{24} \\ \{0\}^T & 0 \\ \{\zeta\}_o^T & t_\zeta \end{bmatrix}\qquad(27)$$

$$\begin{cases} u_1=\dfrac{\{m_1^1\}^T\{w\}_o+m_{14}^1}{\{\zeta_1\}^T\{w\}_o+t_{\zeta 1}^1} \\ v_1=\dfrac{\{m_2^1\}^T\{w\}_o+m_{24}^1}{\{\zeta_1\}^T\{w\}_o+t_{\zeta 1}^1} \end{cases},\quad \begin{cases} u_2=\dfrac{\{m_1^2\}^T\{w\}_o+m_{14}^2}{\{\zeta_2\}^T\{w\}_o+t_{\zeta 2}^2} \\ v_2=\dfrac{\{m_2^2\}^T\{w\}_o+m_{24}^2}{\{\zeta_2\}^T\{w\}_o+t_{\zeta 2}^2} \end{cases}\qquad(28)$$

It has to be pointed out that in these last the apexes 1, 2 of the terms m represent the camera .
If we consider that vector $\{w\}_o$ is the same one for both the systems, we can write:

$$\begin{cases} (u_1\{\zeta_1\}-\{m_1^1\})^T\{w\}_o=m_{14}^1-u_1t_{\zeta 1}^1 \\ (v_1\{\zeta_1\}-\{m_2^1\})^T\{w\}_o=m_{24}^1-v_1t_{\zeta 1}^1 \\ (u_2\{\zeta_2\}-\{m_2^1\})^T\{w\}_o=m_{14}^2-u_2t_{\zeta 2}^2 \\ (v_2\{\zeta_2\}-\{m_2^2\})^T\{w\}_o=m_{24}^2-v_2t_{\zeta 2}^2 \end{cases}\qquad(29)$$

This last equation can be written more strictly:

$$[A]\{w\}_o=\{b\}\qquad(30)$$

ISSN 1590-8844
International Journal of Mechanics and Control, Vol. 08, No. 01, 2007

where:

$$[A] = \begin{bmatrix} \left(u_1\{\zeta_1\} - \{m_1^1\}\right)^T \\ \left(v_1\{\zeta_1\} - \{m_2^1\}\right)^T \\ \left(u_2\{\zeta_2\} - \{m_2^1\}\right)^T \\ \left(v_2\{\zeta_2\} - \{m_2^2\}\right)^T \end{bmatrix}$$

and

$$\{b\} = \begin{Bmatrix} m_{14}^1 - u_1 t_{\zeta 1}^1 \\ m_{24}^1 - v_1 t_{\zeta 1}^1 \\ m_{14}^2 - u_2 t_{\zeta 2}^2 \\ m_{24}^2 - v_2 t_{\zeta 2}^2 \end{Bmatrix}$$

It is evident that in eq. (30) both matrix [A] and vector {b} depend only from the camera parameters and from the coordinates (in pixel) of the point in the two image planes.
The matrix [M] in the equations (25) has always a null row, hence a null determinant; this makes impossible to compute $\{w\}_o$ from the coordinates in pixel; in equation (30), instead, it is possible to use the left pseudo-inverse of matrix [A], except for singularities. Consequently we have:

$$\{w\}_o = \left([A]^T [A]\right)^{-1} \cdot [A]^T \{b\} \tag{31}$$

Equation (31) represents the relation of the acknowledgment of a point by means of a stereoscopic vision system with calibrated cameras. It is possible to go back to the position of a point of the space, in the chosen reference system, if are known the coordinates of this point in two different images. This result is the principle of the visual acknowledgment used for path planning.

3 THE CAMERA CALIBRATION

Camera calibration in the context of three-dimensional machine vision is the process of determining the internal camera geometric and optical characteristics (intrinsic parameters) and/or the 3-D position and orientation of the camera frame relative to a certain world coordinate system (extrinsic parameters). In many cases, the overall performance of the machine vision system strongly depends on the accuracy of the camera calibration.
In order to calibrate the tele-cameras a toolbox, developed by Christopher Mei, INRIA Sophia-Antipolis [8], was used. By means of this toolbox it is possible to find the intrinsic and extrinsic parameters of two cameras that are necessary to solve the stereoscopic problem. In order to carry out the calibration of a camera, it is necessary to acquire any number of images of observed space in which a checkerboard pattern is placed with different positions and orientations [9, 10].
In each acquired image, after clicking on the four extreme corners of a checkerboard pattern rectangular area, a corner extraction engine includes an automatic mechanism for counting the number of squares in the grid. These points are used like calibration points. The dimensions dX, dY of each of squares on the checker board are always kept to their original values in millimeters, and represent the parameters that put in relation the pixel dimensions with observed space dimensions (mm).
After corner extraction, calibration is done in two steps: first initialization, and then nonlinear optimization.
The initialization step computes a closed-form solution for the calibration parameters based not including any lens distortion.
The non-linear optimization step minimizes the total reprojection error (in the least squares sense) over all the calibration parameters (9 DOF for intrinsic: focal (2), principal point (2), distortion coefficients (5), and 6*n DOF extrinsic, with n = images number).

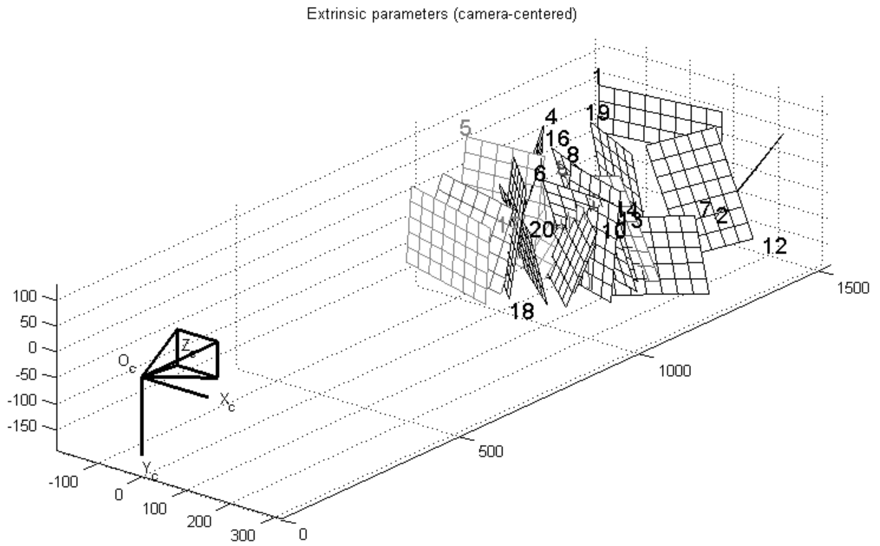

Figure 7 Position of the grids for the calibration procedure.

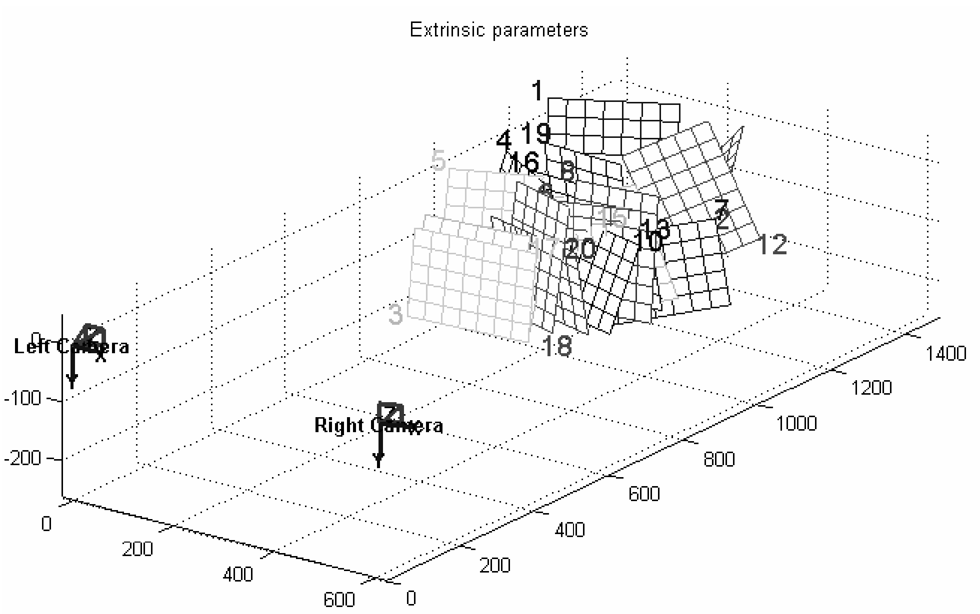

Figure 8 Calibration planes.

The calibration procedure allows to find the 3-D position of the grids with respect to the camera, like shown in fig. 7.
With two camera calibration, it is possible to carry out a stereo optimization, by means of a toolbox option, that allows to do a stereo calibration for stereoscopic problem.
The global stereo optimization is performed over a minimal set of unknown parameters, in particular, only one pose unknown (6 DOF) is considered for the location of the calibration grid for each stereo pair. This insures global rigidity of the structure going from left view to right view.
In this way the uncertainties on the intrinsic parameters (especially that of the focal values) for both cameras it becomes smaller.
After this operation, the spatial configuration of the two cameras and the calibration planes may be displayed in a form of a 3D plot, like shown in fig. 8.In figure 9 is reported the vision test rig: the two telecameras, the checkerboards and the robot.

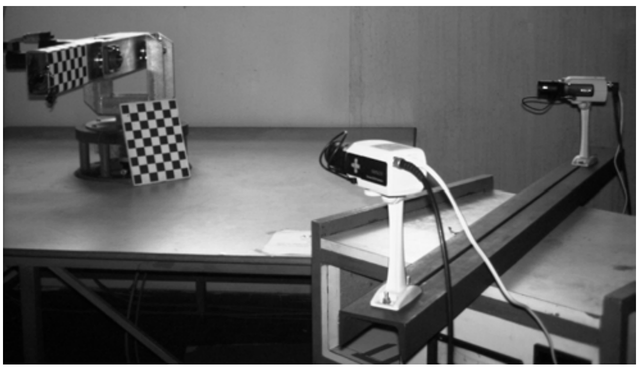
Figure 9 The stereoscopic vision system.

4 THE PATH PLANNING SOFTWARE

The procedure starts from a couple of images (taken from two different cameras); the operator selects (with the cursor) a point on the first image of the couple and this will fix a point in a plane. Subsequently, on the second image appears a green line, that represents the straight line that links the focus of the first camera to that point. Now the operator can fix the real position (in the work space) of that point by clicking on this green line.
In figure 10 the couple of images is reported; on the left is reported the first image and on the right the second one; on the second image is also reported a white solid thick line that is the line that links the focus of the first camera to the point selected on the image on the left.
This procedure gives the coordinates of the selected point in the frame of the working space (world frame). Once a point has been assigned in the work space, by means of inverse kinematics it is possible to compute the joint coordinates of the robot when the robot's end-effector is in that position.
Finally the procedure permits to assign a point either as belonging to the path, or as representing an obstacle; in this last case, the path will be computed in order to avoid that point.
In figure 11 the robot arm and the work space are shown; the numbers 1, 2 and 3 represent three points of the path and the cardinals I and II represent two obstacles that are supposed to be spherical.
In has to be pointed out that, as previously told, to fix a point a couple of images is needed; in figure 11, for the sake of simplicity, just two images are reposted: on the left is the first image of the couple used for the points, while on

the right is reported the second image of the couple for the obstacles.
The path is made up by straight segments that link the selected points (those belonging to the path). The point that represent an obstacle are recorded as a sphere, if the a straight segment intersects a sphere; the procedure records these intersections and joints each couple of them by means of an arc of a circle. So, the path will consist in a number of straight segments and arcs of circle.
In figure 12 is reported an example of a part of a path in perspective representation.
In figure 13 the robot arm and an example of path are shown. In the same figure the points and the obstacles are, also, clearly visible. The points are marked with the same meanings used in the previous figure.

6 CONCLUSIONS

A technique that uses a vision system in path planning, has been proposed and tested at the Laboratory of Robot Mechanics of the D.I.M.E. This technique permits to plan the robot end-effector path starting from two images of the work space, recorded with a vision system, that is previously calibrated. The customer must only choose, with the mouse on the monitor, the points that belong to the path or represent an obstacle; and the procedure computes the robot end-effector path.
The procedure is divided in two steps: the first step supplies to find the cartesian coordinates of the points that belongs to geometric path and of those points that represent an obstacle; the second step carries out cinematic inversion to calculate the points coordinates in the joint space.

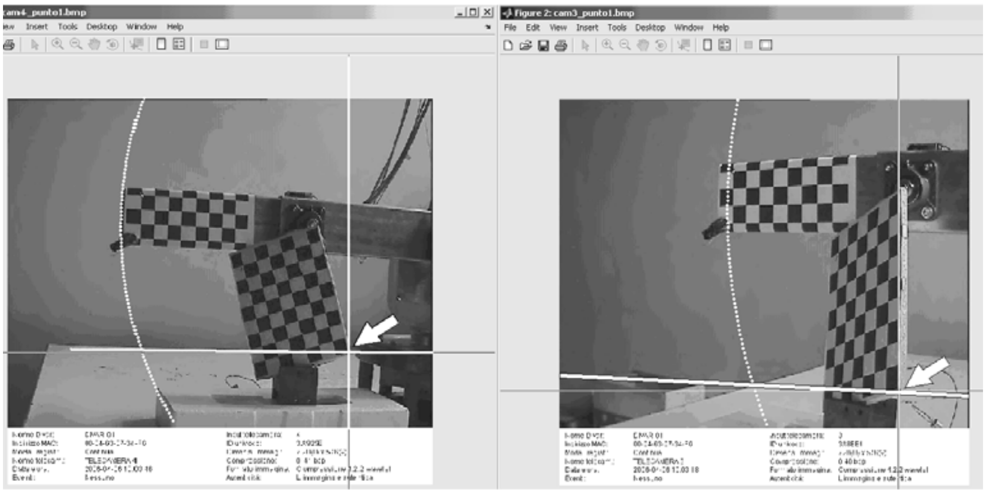

Figure 10 Point assigning by the couple of images.

Figure 11 Path assigning.

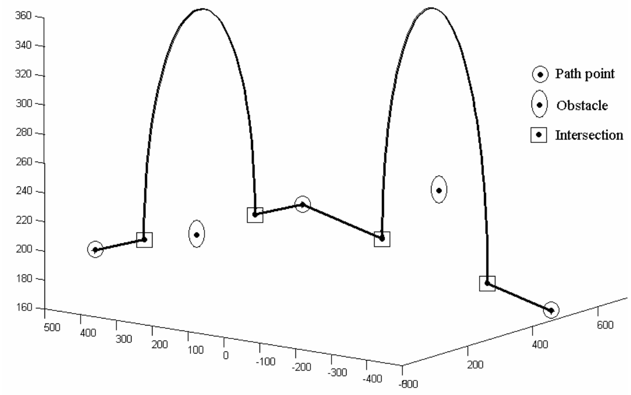

Figure 12 Example of path in perspective view.

Once time information are fixed, it will be also possible to calculate velocities and accelerations that each joint must have in order to describe the planned trajectory.
Future developments of studied vision-planning system, are acknowledgment of the objects in the work space, acknowledgment of surfaces and volumes, and its equations. This last aspect demands the contemporary use of more cameras, mainly in the cases of objects that have cavity. Ulterior developments will concur the improvement of obstacles acknowledgment modalities, and more "fluid" trajectory planning by means of a real-time control with vision system.

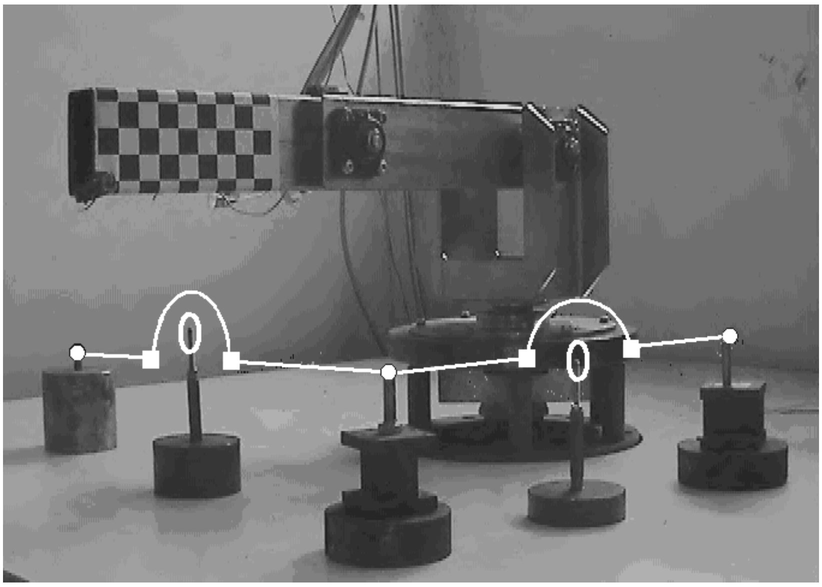

Figure 13 Example of path in the work space.

REFERENCES

[1] V. Niola, C.Rossi: A method for the trajectories recording of a robot arm: early results - *Proc. 9th WSEAS International Conference on Computers*, Athens 11 - 16 July 2005.
[2] V.Niola, C. Rossi: Video acquisition of a robot arm trajectories in the work space - *WSEAS Transactions on Computers*, Iusse 7, Vol. 4, july 2005, pp. 830 – 836.
[3] V. Niola, C. Rossi, S. Savino: Modelling and Calibration of a Camera for Trajectories Recording - *Proc. 5th WSEAS Int. Conf. on Signal Processing, Robotics and Automation* – Madrid, February 15-17, 2006.
[4] A. Fusiello: Visione Computazionale: appunti delle lezioni – Informatic Department, University of Verona, 3 March 2005.
[5] R. Sharma, S, Hutchinson – "Motion perceptibility and its application to active vision-based servo control"- *Technical Report UIUC-BI AI RCV-94-05*, The Beckman Institute, Università dell'Illinois, 1994.
[6] R. Sharma – "Active vision for visual servoing: a review - *IEEE Workshop on Visual Servoing: Achivement"* - Application and Open Problems, Maggio 1994.
[7] R. Sharma, S, Hutchinson – "Optimizing hand/eye configuration for visual-servo system" - *IEEE International Confeence on Robotics and Automation* , pp. 172-177, 1995.
[8] [R4] C. Mei: Camera Calibration Toolbox for Matlab -http://www.vision.caltech.edu/bouguetj/calib_doc.
[9] [R5] V. Niola, C. Rossi, S. Savino – "Modelling and calibration of a camera for robot trajectories recording" - *Proc. 5th WSEAS Int. Conf. on "Signal Processing, Robotics and Automation"* – Madrid, February 15-17, 2006.

[10] V. Niola, C. Rossi, S. Savino – "Perspective Transform and Vision System for Robot Trajectories Recording" - *Proc. 5th WSEAS Int. Conf. on "Signal Processing, Robotics and Automation"* – Madrid, February 15-17, 2006.

[11] R. Sharma, S. Hutchinson, On the observability of robot motion under active camera control, *Proc. IEEE International Conference on Robotics and Automation,* May 1999, pp. 162-167.

[12] J. T. Feddema, C. S. George Lee, O. R. Mitchell, Weighted selection of image features for resolved rate visual feedback control, *IEEE Trans. Robot. Automat.,* Vol. 7, 1991, pp. 31-47.

[13] R. Brancati, C. Rossi, S. Savino, A Method for Trajectory Planning in the Joint Space, *Proc. of 14th International Workshop on Robotics in Alpe-Adria-Danube Region,* Bucharest, Romania, May 26-28, 2005, pp. 81-85.

ISSN 1590-8844
International Journal of Mechanics and Control, Vol. 08, No. 01, 2007

SUB-SYSTEMS EQUIPMENTS WEIGHT AND VOLUME FIRST ESTIMATION: A TOOL FOR AIRCRAFT CONCEPTUAL DESIGN

Sergio Chiesa, Nicole Viola

DIASp POLITECNICO di TORINO

ABSTRACT

Aim of the paper is to describe a methodological approach in order to perform a preliminary estimation of weight and volumes of equipments, that have to be integrated into new a concept of aircraft, during the early definition phase of the design. It is quite obvious that the weight of all aircraft components is relevant in order to define the total aircraft weight but even more important is the correct preliminary estimation of weight and volumes of each single equipment, in order to define their installation (i.e. their position inside the airplane) to check not only the total amount of weight but also the centre of gravity (C.o.G.) coordinates, the inertia moments and the airplane volumes, and in order to establish a suitable starting point for safety (influenced by installation) and maintainability (influenced by accessibility) preliminary studies.

Keywords: Aircraft System Design, Equipment installation, Equipment weight estimation, Volume estimation

1 INTRODUCTION

In Aerospace Engineering the conceptual design phase (i.e. the very early phase of the design process) is extremely important. A typical tool of aircraft conceptual design methodologies is the Weight Estimation, i.e. a set of Weight Estimation Relationships (WERs) for every parts of the aircraft [1], or better, for every “sub-systems” of the “system” of the aircraft. In more traditional applications the WERs have the main task of giving us addenda of the total Aircraft Weight, so accounting in this the influencies of characteristics even typical of single parts. More recently, the introduction of modern 3D-CAD parametric SW has induced a great improvement to computerized Conceptual Design methodologies, [2], in particular allowing to take into account the compatibility between the global system (the Aircraft) and its component parts, not only from the point of view of weight but also of volume.
Consequently, even if in a simplified way, the digital mock-up has become an important output of the conceptual design, as it makes it possible to better define the concept of the aircraft itself and as it represents a good beginning for installation studies (safety analyses for installation and accessibility analyses for maintenance). While in the traditional approach the Weight Estimation is generally performed only at subsystem level (i.e. wing, fuselage, tail, landing gear, propulsion, flight controls system, hydraulic system, fuel system, electrical system, avionics, etc.), nowadays, thanks to the introduction of 3D-CAD, the possibility of drawing up the estimation of weight and of volume at equipment level is real. Some ideas about how this task can be accomplished, taking as examples some kinds of equipments usually installed on aircraft, will be presented in the following paragraphs.

Contact author: Sergio Chiesa, Nicole Viola

DIASp Politecnico di Torino

Corso Duca degli Abruzzi 24 – 10129 Torino Italy

2 WEIGHT AND VOLUME ESTIMATION OF EQUIPMENTS

2.1 GENERAL

In weight estimation two main approaches are available: analytic and statistic. In traditional methodologies the analytical approach has been used [3] mainly for structural parts, like wing, body, etc., but, at the end, the statistical one was found more suitable, in particular for the on-board subsystems, and became the preferred approach [1].

ISSN 1590-8844
International Journal of Mechanics and Control, Vol. 08, No. 01, 2007

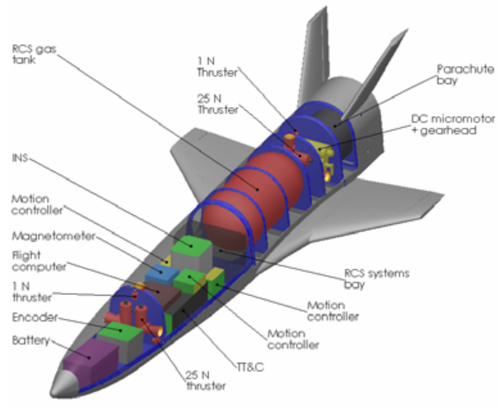

Figure 1 Example of preliminary Digital Mock-up [4]

The introduction of 3D-CAD opened a new way in order to overcome the statistical approach limits (limits in the statistical base, difficulties when facing innovative design cases) by drawing the hypothesized solution and calculating the weight via the estimation of the density of materials.
However, if the estimation of the density of materials is quite easy for structural parts, this is not so for not structural on-board sub-systems; consequently, the statistical approach remains the only suitable, at least for not-structural subsystems.
What is true for subsystems is even more valid for equipments, that are component parts of such subsystems; moreover equipments data are usually available for a number of elements for every kind, so giving us, generally, a good statistical basis

Table I - Simplified forms assumed for equipments

Equipments	**Examples (Photographs & artistic impressions)**				**Simplified assumed forms**
A.P.U.- (Axiliary Power Unit)		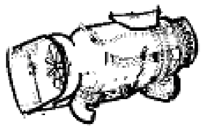			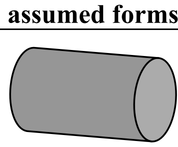
FAN		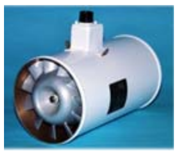			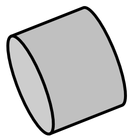
ELECTRICAL GENERATOR					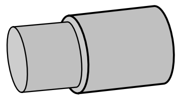
	IDG – Integrated Driven Generators				
					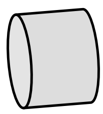
	Generators				
ELECTRICAL & AVIONICS		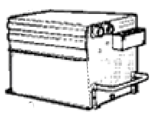		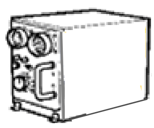	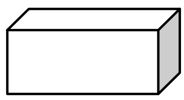
	TRU-Transformer Rectifier Unit		Inverter	Avionic equipment	
HYDRAULIC PUMPS (or MOTORS)					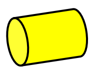

As far as the estimation of volumes is concerned, the problem is a little more complex because of the extremely widespread unevenness of forms, even if the same kind of equipment is considered. By the way, we can assume a simple and geometrically regular form for every kind of equipment: quite obviously the hypothesised form has to be as close as possible to the real shape.
As a matter of fact, the first "digital mock-up" is usually made with simplified forms for equipments, (if not yet fully defined, like it is in the case of "C.O.T.S. – Commercial Off The Shelf"), as shown in Figure 1, in which the preliminary digital mock-up of a "concept" of a re-entry vehicle is reported. To be clearer, next Table I shows how many kinds of equipments could be, quite well, represented by simplified forms, generally cylinders and boxes.
Please note that in Table I only few kinds of equipments, usually present on-board of aircraft, have been reported. Nevertheless, they are sufficiently different one from the other to establish and explain the methodological approach, that is the aim of the paper.
In the following paragraphs an heuristic approach to weight and volume estimation, is discussed, taking as examples APU and "axial flow Fan".

2.2 AUXILIARY POWER UNITS – APU

The APU is, in the context of all on-board subsystems, one of the most important equipment from the point of view of both volume and weight: Moreover, it is quite critical for the constraints related to its integration requirements, which are the need for air adduction and gas exhaust, the interface with other subsystems, safe location for passengers (in civil aircraft), noise reduction, accessibility issues, etc. In Figure 2 an example of an APU installation is shown.

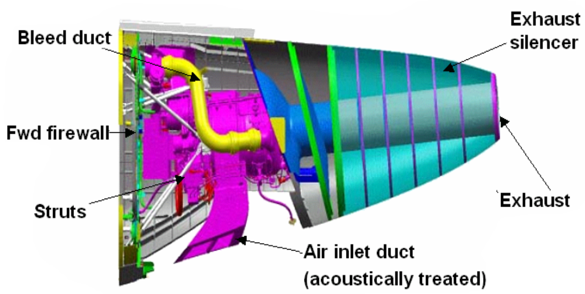

Figure 2 Example of APU installation in tail cone

In Table II are reported data of some APUs for small-medium size transport aircraft: in particular, the APU weights (W_{APU}) and the number of passengers (N° Pass) of the reference aircraft are shown respectively in column 3 and column 4. These two type of data have been taken into account together because it is plausible to search for correlation between such two parameters, as Figure 3, clearly shows. From Figure 3 the following WER can be established:

$$W_{APU} = 50 + 0.2\,(\text{N° Pass.}) \qquad (1)$$

Table II - Weight and Volume estimation of A.P.U.

A.P.U. [Reference Aircraft]		W_{APU} [kg]	N° Pass.	Drawing	L/Φ	Vol [dm^3]	ρ[kg/dm^3]
APS 3200 [Airbus Single-Aisle Aircraft Family]		140	199	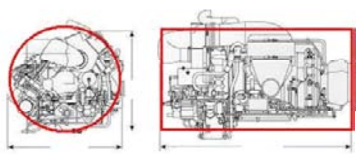	1.54	628.3	0.22
APS 2100 [Boeing 717]		186	120	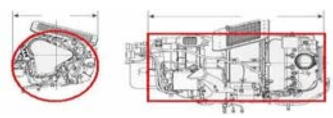	1.66	454.1	0.41
APS 2000 [Boeing 737]		128	140		2.40	348.3	0.37
APS 1000 [BaeSystem BAe 146 & AVRO RJ]		86	90	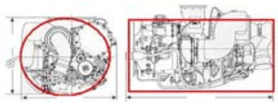	1.46	281.8	0.30
APS 1000 [Bombardier deHavilland Dash 8-400]		86	60	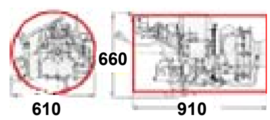	1.43	270.3	0.32

Table III - Fan's Weight and Volume estimation

FAN		**Volume Flow [m^3/min]**	**W_{FAN} [kg]**	**DRAWING**	**DIMENSIONS**		**L/Φ**	**Vol [dm^3]**	**ρ [kg//dm^3]**
					L	**D**			
FAN Axial Flow **6577-1**		80	3.18	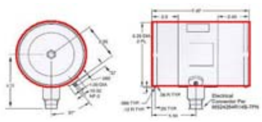	190	147	1.30	3.20	0.98
FAN Axial Flow **731376**		115	6.66	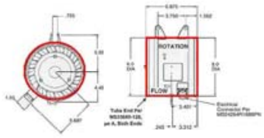	175	203	0.86	5.67	1.18
FAN Axial Flow **731378-1**		60	3.22	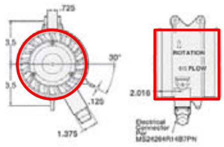	140	127	0.91	1.95	1.65
FAN Axial Flow **4100044**		140	11.33	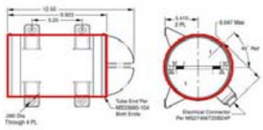	252	178	1.41	6.26	1.81
FAN Axial Flow **4100947**		25	1.54	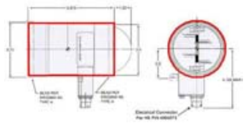	149	95	1.57	1.06	1.45
FAN Axial Flow **4101054**		82	3.17	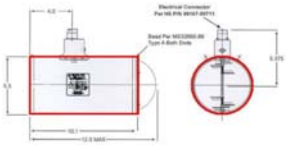	257	140	1.84	3.93	0.91
FAN Axial Flow **4101257**		150	3.31	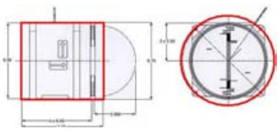	178	168	1.06	3.92	0.84
FAN Axial Flow **4101408**		232	6.21	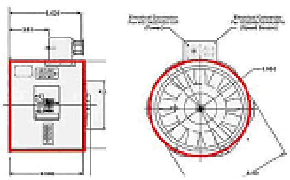	165	228	0.72	6.63	0.94
FAN Axial Flow **4101410**		56	2.94	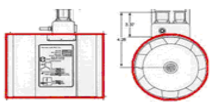	159	121	1.31	1.62	1.81

ISSN 1590-8844
International Journal of Mechanics and Control, Vol. 08, No. 01, 2007

As far as the volume is concerned, considering the variety and the complexity of APU forms (see second column of Table II), column 5 shows how such forms can be approximated by cylinders with length to diameter ratio (L/Φ) varying not so much.

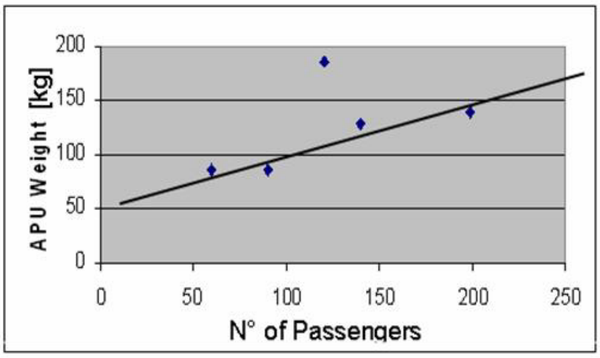

Figure 3 APU's Weight vs N° of Passengers

From column 6 of Table II we can infer that a good value for the length to diameter ratio (if more detailed data are not available) can range from about 1.5 to 2.4. Finally, in column 7 the volumes of these cylinders are calculated and in column 8 the APU weights divided by such volumes give an "assumed density", that is, for APU, equal to about 0.35 kg/dm^3. Figure 4 shows how good is the estimation of this assumed density (at least for APUs): this will be very useful for preliminary evaluations.

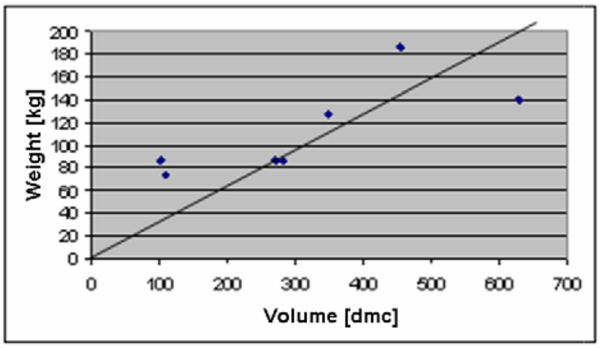

Figure 4 APU "assumed density" = Weight/Volume

2.3 AXIAL FLOW FAN

The second kind of component considered is the axial fan (with its embedded electrical motor), usually utilized for passengers cabin or avionic bays cooling. The choice of considering this kind of component is due to its extremely high variety in terms of weight, volume, temperatures, power levels (in comparison with above seen APU), besides the good availability of data, shown in Table III. Before analysing these data, in order to better understand them, more technical data of the first Fan presented in Table III are reported in Table IV, and, in Figure 5, where the balance of powers determines the maximum amount of Volumetric Flow.

In the case of Fan, at the contrary of APU, any correlation of Weight values with airplane characteristics is possible, because the action of fan is extremely localized, on a part or better on a bay of the airplane; in other words fan of small size could be present on a great size planes and vice-versa..

So correlation of weight values has been found with an equipment's functional parameter, in particular the Volumetric Flow.

This correlation Fan Weight vs. Volumetric Flow is shown in Figure 6 and can be expressed as:

$$W_{FAN} = 0.033\,(\text{Vol. Flow}) + 1 \qquad (2)$$

Like in the APU case, the form that better represents the Fan is the cylinder; the ratio L/□ can be assumed = 1.3. Matching Weight and Volume data from Table III, with good correlation as shown in Figure 6, the "assumed density" value for Fans will be considered about 1.3.

Table IV - Example of FAN characteristics

<table>
<tr><td>FAN Axial Flow P/N 6577-1</td><td></td></tr>
<tr><td colspan="2"><u>Design Features</u>
Oversize Precision Bearings
Lightweight Cast Aluminium Construction</td></tr>
<tr><td colspan="2"><u>Applications</u>
Avionics Cooling: Boeing B737, B747</td></tr>
<tr><td colspan="2"><u>Technical Data</u>
Input Power
* 115 / 200 VAC
* 3 Phase / 400 HZ
Speed = 11,500 RPM
Weight = 7.0 Pounds = 3,18 kg</td></tr>
</table>

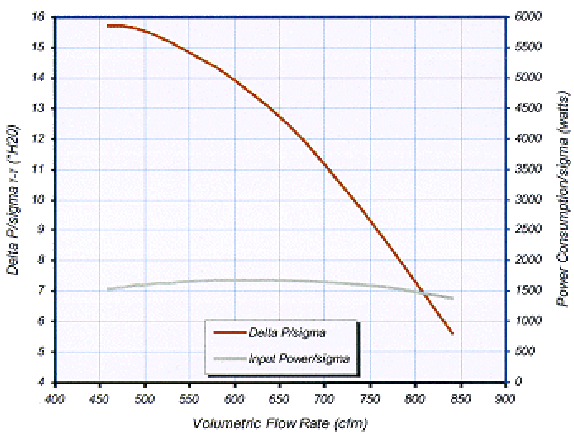

Figure 5 Volumetric Flow of Fan

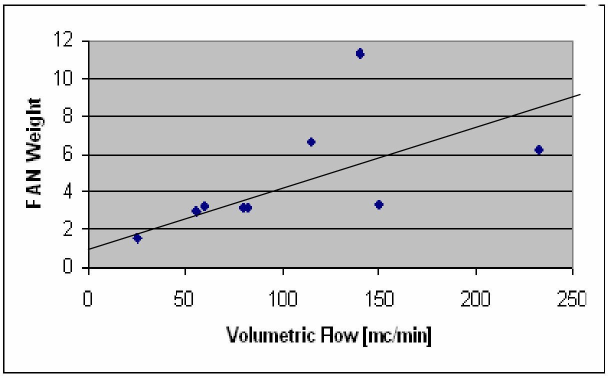

Figure 6 Fan Weight vs. Volumetric Flow

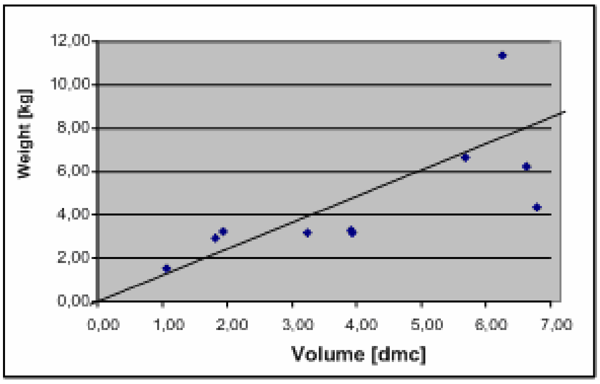

Figure 7 FAN “assumed density” = Weight

2.4 OTHER EQUIPMENTS

In the previous point the “idea” of “assumed density” that, if known, can offer an easy way to estimate equipment volume, following the more usual weight estimation, has been presented for two, very different kind of equipment.

To repeat so detailed discussion for every other main equipments would be too long: so, in the present point, an application of concept of “assumed density” almost for other kinds of equipments presented in Table I, will be now shortly presented and discussed, having as reference the Table V too.

2.4.1 IDG – Integrated Driven Generator

This equipment is an a.c. brushless generator with an integrated mechanical-hydraulic transmission able to give a constant rotating speed output to generator, even if the input varies according to different throttle values of the propulsion engine: so it is possible to obtain ac at constant frequency even if the generator is driven by a propulsion engine. In Table V, in a very synthetic way, a WER for IDG, derived from an already defined base [5], with indication of typical parameter values range, has been reported. A value of “assumed density”, derived on the basis of real IDG available data [7] is also proposed.

2.4.2 Starter/Generator

This equipment is the typical on board dc generator for small size aircraft in which it is traditionally preferred to ac generators because of possibility to be used, fed by battery, as starter of propulsion engine too.

In Table V a WER, already defined [6], with indication of typical parameter values range, has been reported. A value of “assumed density”, derived on the basis of real available data [7] is also proposed; the value for the starter/generator is quite high because of mechanical heavy criticality due to brushes and to wide spread of stress (mechanical and thermal), associated with the double running mode.

Table V - Equipments W.E.R.s and assumed density

EQUIPMENT	**Weight Estimation Relationship**	**Typical Parameter Values Range**	**Assumed Density [kg/dm^3]**
IDG (ac – 400 Hz)	W = 18+ 0.5 P P [kvA]	20[kvA]--- 120 [kvA]	1.39
Starter/ /generator (dc)	W =1.5+ 3.5 P P [kw]	3 [kw] -- -- 15 [kw]	3.10
Brushless dc generator	W = 8,6+ 0.55P P [kw]	3 [kw] -- -- 15 [kw]	1.40
A.c. generator (ac-wide frequency)	W = 5+ 0.5 P P [kvA]	20[kvA]--- 180 [kvA]	2.20
Electric Starter	W = 6+ 0.038 I I [A]	100 [A] - --500[A]	2.40
Transformer Rectifier Unit	W = 0.5+ 0.03 I I [A]	20 [A] -- - 300[A]	0,99
Inverter	W = 5+ 0.67 P P [kvA]	200[vA]-- --5 [kvA]	0.87
Avionic Equip. (Ex: UHF/VHF radio)	W = 2+ 0.12 P P [w]	5 [w] -- -- 40[w]	1.40
Hydraulic Pump	W = 0.052 Q Q [l/min]	12[l/min]-- 250 [l/min]	4.20

2.4.3 Brushless dc generator

This equipment is an ac generator with fully rectified current output; in this way the brushes, that are a heavy penalisation for the previous seen Starter/Generator, are avoided with advantages by the points of view of reliability and of Electro-Magnetic Compatibility, even if the function of starting engine is no more possible. The WER reported in Table V, in the Starter/Generator one, shows less weight at the same Power. In plus, assumed density for the Brushless dc generator is less then 50% lower then the starter/generator, and that because the relevant presence of electronic parts.

2.4.4 A.c. Generator

This is generator utilized when ac is requested without need of constant frequency (or if an electronic conversion is foreseen in a later time). The WER proposed in Table V, in comparison with the Starter/generator one shows, at the same Power, a lower weight that can be explained by higher voltage. The Power /Weight ratio is a little better than the one of Brushless dc Generator, because the absence of electronic part (to rectifier current), that also explain the higher assumed density value.

2.4.5 Electric Starter
The electric starter is normally utilized on small size airplane, as aforesaid with dc generation, if a starter/generator has not been chosen; so, in many cases, it is accompanying the brushless dc generator. The electric starter is a dc motor with brushes, like the starter/generator, but sized for very short time running only; this explain the assumed density, quite high but less than the one of starter/generator, sized for continuous running..

2.4.6 TRU – Transformer Rectifier Unit
The task of this equipment is to transform in dc a part of ac generated (medium-heavy size airplanes), for users that need this kind of current. Please note that, at the contrary of previous seen equipments, all with mechanical parts, TRU is completely made of electronic parts; this means an assumed density lower than the ones of motors and/or generators. In plus the completely static nature of the equipment allow it to be configured in box form (see Table I).

2.4.7 Inverter
The inverters generate ac (for users that need it) transforming part of dc generated on small size airplane. As seen for TRU they are static equipment, with low assumed density even if a little greater then TRU. For the same reason of TRU it has box form.

2.4.8 Avionic Equipment
First of all is to be considered that Avionics Equipment could be of several kinds, with great differences between them. As example, in Table V, a typical Radio UHF/VHF (Receiver / Transmitter) is presented. In the WER the parameter is the emitted Power in FM and the assumed density is lower then in motors and /or generators because all parts are electronic; this allow to assume box form, like for TRU and Inverters. By the way assumed density is higher then the TRU and Inverters, probably because low power do not requires large clearance between electronic modules in order to dissipate thermal energy.

2.4.9 Hydraulic Pump
The last equipment presented in Table V is the hydraulic pump, also to increase the generality of proposed methodological approach. The equipment is mainly characterized by value of assumed density, higher then in electrical motors, because of very reduced dimensions, as shown in Figure 8, with high power to weight ratio; that is easy to understand by considering WER (having as parameter the volumetric flow Q) reported in Table IV :

$$W_{PUMP} = 0.052\,Q \qquad (3)$$

The deduction of the WER is shown in Figure 9 and Table VI contain the statistical base utilized.

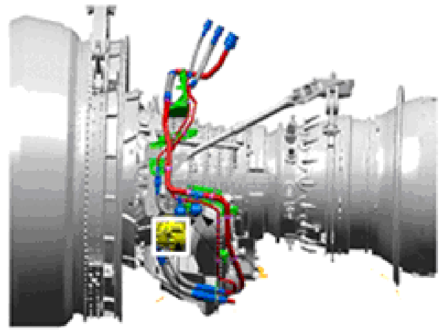

Figure 8 Reduced size typical of hydraulic pump

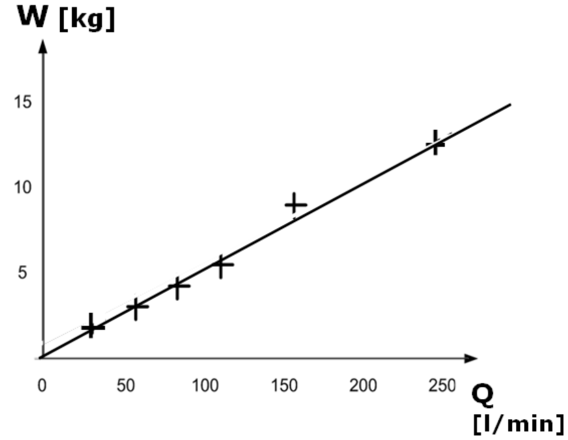

Figure 9 Hydraulic Pumps Weight

Table VI - Data about hydraulic pumps, from [8]

CILINDRATA MASSIMA (cm^3)	VELOCITA' DI ROTAZIONE (RPM) di progetto	massima	PESO (kg)
3,6	10.000	12.500	2
7,2	8.000	10.000	3
12,3	7.000	8.750	4
18,84	6.000	7.500	5,2
27,44	5.650	7.100	9
49,16	5.000	6.250	12,7

By expressing the volumetric flow Q as:

$$Q = C_{MAX} RPM_{MAX} \eta_{VOL} / 1000 \qquad (4)$$

it is easy to link W_{PUMP}, Q and Displacement, listed in the first column of Table VI; for example the greater pump considered, with Q = 250 [l/min] will have W about 12 kg with a displacement C_{MAX} = 49,16; this last is a very small value, that means very reduced size (see Figure 8 again), that also brings to high assumed density value, reported in Table V.

3 CONCLUSIONS

In the previous points the problem of Weight and Volumes estimation, at "equipment levels", has been discussed, pointing out their relevance in the field of Aerospace Vehicles conceptual design.
Two problems that has been presented are:
-Definition of a "simplified form assumed" for every kind of Equipments, with some example on quite different cases
- Introduction of so called "assumed density" ρ.
For two very different (size, function…) kind of equipments like APU and axial flow Fan the ρ has been statistically derived, as well as weights, offering to Designers the possibility of quick estimation of dimensions if weight is known or vice versa.
Finally, for some others components (electrical motors and/or generators, electrical / electronic static devices), the indicative values of weight and assumed density has been discussed.
The same discussion has been made for airborne hydraulic pump (or motor), underlining high value of ρ, that explains the very reduced size (for a given Power value) typical of this equipment.
All methodological approach discussed in the paper are to be considered as ideas to be tailored, in appropriate ways, to all (or, at less, to greater part) of kinds of equipments that constitute the present advanced aerospace systems.

ACKNOWLEDGEMENTS

The Authors give many thanks to Ing. Alessandro Rougier for valid support in data collection and analysis.

REFERENCES

[1] Chiesa S., *Sulla previsione del peso degli impianti di bordo nella fase preliminare del progetto dei velivoli*, Ingegneria, n°1-2, 1977.

[2] Chiesa S., DiSciuva M., Camatti D., Corpino S., Pasquino M, *Utilizzo di CAD 3D parametrico per Studi di configurazione e Digital Mock-up nel progetto concettuale*, AIDAA Congress, Turin, Nov. 1999.

[3] Gabrielli G., *Peso teorico e peso reale delle ali a sbalzo*, L'Aerotecnica 1, 1953

[4] Chiesa S., Corpino S., Viola N., *Feasibility study of a technological demonstrator of reduced size for sub-orbital flight*, 24th ICAS Congress, Yokohama, Japan, August-September 2004.

[5] Chiesa S., Tonso A., *Tendenze e sviluppi attualinei sistemi di generazione della potenza elettrica in c.a. a frequenza fissa a bordo degli aeromobili,* Aerotecnica Missili e Spazio, Vol.59, n°2/80.

[6] Chiesa S., *Sulla razionalizzazione della generazione elettrica sui velivoli da trasporto regionale di nuova generazione*, L'Aerotecnica Missili e Spazio, Vol.66, n°2, 1987

[7] Chiesa S., *Impianti di bordo per aeromobili: impianto elettrico*, CLUT Torino

[8] Chiesa S., *Impianti di bordo per aeromobili: impianto idraulico*, CLUT Torino

TEMPLATE FOR PREPARING PAPERS FOR PUBLISHING IN INTERNATIONAL JOURNAL OF MECHANICS AND CONTROL

Author1* Author2**

* affiliation Author1

** affiliation Author2

ABSTRACT

This is a brief guide to prepare papers in a better style for publishing in International Journal of Mechanics and Control (JoMaC). It gives details of the preferred style in a template format to ease paper presentation. The abstract must be able to indicate the principal authors' contribution to the argument containing the chosen method and the obtained results. (max 200 words)

Keywords: keywords list (max 5 words)

1 TITLE OF SECTION (E.G. INTRODUCTION)

This sample article is to show you how to prepare papers in a standard style for publishing in International Journal of Mechanics and Control.
It offers you a template for paper layout, and describes points you should notice before you submit your papers.

2 PREPARATION OF PAPERS

2.1 SUBMISSION OF PAPERS

The papers should be submitted in the form of an electronic document, either in Microsoft Word format (Word'97 version or earlier).
In addition to the electronic version a hardcopy of the complete paper including diagrams with annotations must be supplied. The final format of the papers will be A4 page size with a two column layout. The text will be Times New Roman font size 10.

Contact author: author1[1], author2[2]

[1]Address of author1.

[2]Address of author2 if different from author1's address.

2.2 DETAILS OF PAPER LAYOUT

2.2.1 Style of Writing

The language is English and with UK/European spelling. The papers should be written in the third person. Related work conducted elsewhere may be criticised but not the individuals conducting the work. The paper should be comprehensible both to specialists in the appropriate field and to those with a general understanding of the subject.
Company names or advertising, direct or indirect, is not permitted and product names will only be included at the discretion of the editor. Abbreviations should be spelt out in full the first time they appear and their abbreviated form included in brackets immediately after. Words used in a special context should appear in inverted single quotation mark the first time they appear. Papers are accepted also on the basis that they may be edited for style and language.

2.2.2 Paper length

Paper length is free, but should normally not exceed 10000 words and twenty illustrations.

2.2.3 Diagrams and figures

Figures and Tables will either be entered in one column or two columns and should be 80 mm or 160 mm wide respectively. A minimum line width of 1 point is required at actual size. Captions and annotations should be in 10 point with the first letter only capitalised *at actual size* (see Figure 1 and Table VII).

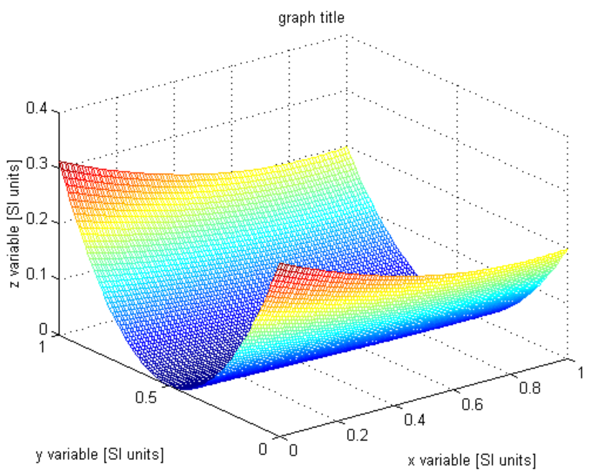

Figure 1 Simple chart.

Table VII - Experimental values

Robot Arm Velocity (rad/s)	Motor Torque (Nm)
0.123	10.123
1.456	20.234
2.789	30.345
3.012	40.456

2.2.4 Photographs and illustrations

Authors could wish to publish in full colour photographs and illustrations. Photographs and illustrations should be included in the electronic document and a copy of their original sent. Illustrations in full colour …

2.2.5 Equations

Each equation should occur on a new line with uniform spacing from adjacent text as indicated in this template. The equations, where they are referred to in the text, should be numbered sequentially and their identifier enclosed in parenthesis, right justified. The symbols, where referred to in the text, should be italicised.

- point 1
    - point 2
        - point 3

1. numbered point 1
    2. numbered point 2
        3. numbered point 3

$$W(d) = G(A_0, \sigma, d) = \frac{1}{T}\int_0^{+\infty} A_0 \cdot e^{-\frac{d^2}{2\sigma^2}} dt \tag{1}$$

3 COPYRIGHT

Authors will be asked to sign a copyright transfer form prior to JoMaC publishing of their paper. Reproduction of any part of the publication is not allowed elsewhere without permission from JoMaC whose prior publication must be cited. The understanding is that they have been neither previously published nor submitted concurrently to any other publisher.

4 PEER REVIEW

Papers for publication in JoMaC will first undergo review by anonymous, impartial specialists in the appropriate field. Based on the comments of the referees the Editor will decide on acceptance, revision or rejection. The authors will be provided with copies of the reviewers' remarks to aid in revision and improvement where appropriate.

5 REFERENCES (DESCRIPTION)

The papers in the reference list must be cited in the text. In the text the citation should appear in square brackets [ ], as in, for example, "the red fox has been shown to jump the black cat [3] but not when...". In the Reference list the font should be Times New Roman with 10 point size. Author's first names should be terminated by a 'full stop'. The reference number should be enclosed in brackets.
The book titles should be in *italics*, followed by a 'full stop'. Proceedings or journal titles should be in *italics.* For instance:

REFERENCES (EXAMPLE)

[1] Smith J., Jones A.B. and Brown J., *The title of the book*. 1st edition, Publisher, 2001.

[2] Smith J., Jones A.B. and Brown J., The title of the paper. *Proc. of* Conference *Name*, where it took place, Vol. 1, paper number, pp. 1-11, 2001.

[3] Smith J., Jones A.B. and Brown J., The title of the paper. *Journal Name*, Vol. 1, No. 1, pp. 1-11, 2001.

[4] Smith J., Jones A.B. and Brown J., *Patent title*, U.S. Patent number, 2001.

International Journal of Mechanics and Control – JoMaC
Published by Levrotto&Bella
TRANSFER OF COPYRIGHT AGREEMENT

NOTE: Authors/copyright holders are asked to complete this form signing section A, B or C and mail it to the editor office with the manuscript or as soon afterwards as possible.	*Editor's office address:* Andrea Manuello Bertetto Elvio Bonisoli *Dept. of Mechanics* *Technical University – Politecnico di Torino* *C.so Duca degli Abruzzi, 24 – 10129 Torino – Italy* *e_mail: jomac@polito.it* *fax n.: +39.011.564.6999*

The article title:

By:____

To be Published in ***International Journal of Mechanics and Control JoMaC***
Official legal Turin court registration Number 5320 (5 May 2000) - reg. Tribunale di Torino N. 5390 del 5 maggio 2000

A Copyright to the above article is hereby transferred to the JoMaC, effective upon acceptance for publication. However the following rights are reserved by the author(s)/copyright holder(s):
1. All proprietary rights other than copyright, such as patent rights;
2. The right to use, free or charge, all or part of this article in future works of their own, such as books and lectures;
3. The right to reproduce the article for their own purposes provided the copies are not offered for sale.

To be signed below by all authors or, if signed by only one author on behalf of all co-authors, the statement A2 below must be signed.

A1. All authors:

SIGNATURE_______________________________DATE___________ SIGNATURE_______________________________DATE___________

PRINTED NAME_______________________________________ PRINTED NAME_______________________________________

SIGNATURE_______________________________DATE___________ SIGNATURE_______________________________DATE___________

PRINTED NAME_______________________________________ PRINTED NAME_______________________________________

A2. One author on behalf of all co-authors:
"I represent and warrant that I am authorised to execute this transfer of copyright on behalf of all the authors of the article referred to above"

PRINTED NAME_______________________________________

SIGNATURE_______________________________ TITLE_______________________________ DATE_______________

B. The above article was written as part of duties as an employee or otherwise as a work made for hire. As an authorised representative of the employer or other proprietor. I hereby transfer copyright to the above article to Editel-Pozzo Gros Monti effective upon publication. However, the following rights are reserved:
1. All proprietary rights other than copyright, such as patent rights;
2. The right to use, free or charge, all or part of this article in future works of their own, such as books and lectures;
3. The right to reproduce the article for their own purposes provided the copies are not offered for sale.

PRINTED NAME_______________________________________

SIGNATURE_______________________________ TITLE_______________________________ DATE_______________

C. I certify that the above article has been written in the course of employment by the United States Government so that no copyright exists, or by the United Kingdom Government (Crown Copyright), thus there is no transfer of copyright.

PRINTED NAME_______________________________________

SIGNATURE_______________________________ TITLE_______________________________ DATE_______________

CONTENTS

next number scheduled titles:

Optimization of Relative Orbit Transfer with Low Thrust Propulsion
M. Massari

Nonlinear Elastic Characteristic of Magnetic Suspensions through Hilbert Transform
E. Bonisoli

Proposal of Innovative Fluid Dynamic Nonlinear Servovalve Models
L. Borello, M. D. L. Dalla Vedova

A Stress Evaluation Strategy for Designing Squat Structures
C. Rosso

Dynamic Root Stress Analysis in a Spur Gear under Impact Moving Load
T. Jingwei, X. Buqing, W. Shibin, B. Picasso